UNIVERSIDADE DE SÃO PAULO
INSTITUTO DE FÍSICA DE SÃO CARLOS

Marcia Frometa Fernandez

Coherent light-matter interaction in dense atomic clouds

São Carlos

2024

Marcia Frometa Fernandez

Coherent light-matter interaction in dense atomic clouds

Thesis presented to the Graduate Program in Physics at the Institute of Physics of São Carlos - University of São Paulo, to obtain the degree of Doctor of Science.

Concentration area: Theoretical and Experimental Physics

Advisor: Prof. Dr. Philippe Wilhelm Courteille

Coadvisor: Prof. Dr. Raul Celistrino Teixeira

Corrected version

(Original version available on the Program Unit)

São Carlos

2024

Fernandez, Marcia Frometa
Coherent light-matter interaction in dense atomic clouds / Marcia Frometa Fernandez; advisor Philippe Wilhelm Courteille; co-advisor Raul Celistrino Teixeira - corrected version -- São Carlos 2024.
124 p.

Thesis (Doctorate - Graduate Program in Theoretical and Experimental Physics) -- Instituto de Física de São Carlos, Universidade de São Paulo - Brasil , 2024.

1. Dense regime. 2. Optical dipole trap. 3. Coupled dipole model. I. Courteille, Philippe Wilhelm, advisor. II. Teixeira, Raul Celistrino, co-advisor. III. Title.

ACKNOWLEDGEMENTS

I would like to express my gratitude to many people, not only because their presence was relevant to the development of this work, but also because they were crucial in my life during these 4 (almost 5) years of pursuing my Ph.D.

My deep appreciation goes to my advisors, Raul and Philippe, for granting me the opportunity to conduct this research and for their continuous support. I also want to thank them for their understanding and patience during my Ph.D. journey and for motivate me to become a better scientist.

I extend this gratitude to Romain for the support he provided during the simulations of the Couple Dipole Model, and for the pizza evenings at his house with Dilleys.

Part of the content of this thesis is attributed to my dear laboratory colleagues: Pablo, Pedro, Ana, and Matheus, who assisted me significantly in the development of my research project. I want to express my gratitude to them and the other members of the strontium family (Claudio and Gustavo) for making the work more enjoyable and for brewing coffee for me every afternoon. Special thanks to Pablo, who is not only a great scientist but also a remarkable person that I'm proud to call a friend.

To my friends Dalila, Ana, Lucas, and Vinicius for being one of the greatest gifts São Carlos has given me. They have been like family to me during these years.

To Gessica for the emotional support (especially during the writing process of this document), for the love, patience and motivate me to be a better person.

To my sister Susana (without whom I probably wouldn't be here today) for always listening to me, advising me, simply for existing and being such an important person in my life that I love with all my heart.

Last but certainly not least, I want to express my deepest thanks to my parents, Sergio and Elena, for their unconditional love and support, for teaching me to be better every day, and for respecting my decisions.

This study was financed in part by the Coordenação de Aperfeiçoamento de Pessoal de Nível Superior - Brasil (CAPES) - Process number 88887.338558/2019-00.

ABSTRACT

FERNANDEZ, M. F. **Coherent light-matter interaction in dense atomic clouds**. 2023. 124p. Ph.D. Thesis (Doctor in science) - Instituto de Física de São Carlos, Universidade de São Paulo, São Carlos, 2024.

The main objective of this research is to study a particular case of light-matter interaction: the scattering of light in dense atomic samples. The regime of high atomic densities is represented by samples where the distance between neighboring atoms is on the order of the wavelength associated with the atomic transition. In this regime, short-range atomic interactions cannot be neglected, and in these systems, we expect to observe significant modifications in collective effects such as subradiance or superradiance. Overall, the propagation of light through this type of system is not well-known to the scientific community, and the existing models work to describe very specific situations.

To pave the way for achieving our overall goal, this work proposes an experimental setup to obtain a dense cloud of ^{88}Sr, which is the chemical species we work with in our laboratory. For this purpose, atoms previously trapped using a Magneto-Optical Trap are transferred to a Crossed Optical Dipole Trap. During the optimization and characterization of the optical trap, problems were encountered in producing an image with quantitative information of the atomic ensemble and in transferring a large number of atoms in a very small trapping volume. These problems were resolved with the implementation of a Phase Contrast Imaging system and the implementation of an Optical Molasses as an additional cooling step. Under these conditions, we obtained a cloud that can be suitable for conducting studies on collective effects, transitioning from the dilute to the dense regime.

The initial experiments, once our atomic ensemble was prepared, involve measuring the coherent transmission of a low-intensity beam through the cloud. For this purpose, incident light near the resonance of a dipolar transition of the type $J = 0 \leftrightarrow J = 1$ of ^{88}Sr is used, interacting with a homogeneous region of the sample. Simulations of this type of process can be performed using the Coupled Dipole Model, which describes the overall response of light scattering by the sample considering dipole-dipole interactions mediated by light. With this work, we aim to advance the understanding of density effects by comparing the coherent optical response of the dense cloud with the theory based on the Coupled Dipole Model.

Keywords: Dense regime. Optical dipole trap. Coupled dipole model.

RESUMO

FERNANDEZ, M. F. **Interação coerente luz-matéria em amostras atômicas densas**. 2023. 124p. Tese (Doutorado em Ciências) - Instituto de Física de São Carlos, Universidade de São Paulo, São Carlos, 2024.

O principal objetivo desta pesquisa é estudar um caso particular da interação luz-matéria: o espalhamento da luz em amostras atômicas densas. O regime de altas densidades atômicas está representado por amostras onde a distância entre átomos vizinhos é da ordem do comprimento de onda associado à transição atômica. Neste regime, as interações de curto alcance não podem ser negligenciadas, e esperamos observar modificações importantes em efeitos coletivos como a subradiância ou superradiância. No geral, a propagação da luz por esse tipo de sistema é um processo não muito conhecido pela comunidade científica, e os modelos existentes funcionam para descrever situações muito específicas.

Para abrir caminho ao cumprimento do nosso objetivo geral, neste trabalho é proposto um arranjo experimental para obter uma nuvem densa de ^{88}Sr, que é a espécie química com a qual trabalhamos em nosso laboratório. Para isso, os átomos previamente aprisionados usando uma Armadilha Magneto-Óptica são transferidos para uma Armadilha Óptica de Dipolo cruzada. Durante o processo de otimização e caracterização da armadilha óptica, foram enfrentados problemas para produzir uma imagem com informação quantitativa do ensemble atômico e para transferir um número grande de átomos num volume de aprisionamento muito pequeno. Esses problemas foram resolvidos com a implementação de um sistema de Imagem de Contraste de Fase e a implementação de um Melaço Óptico como etapa extra de esfriamento. Nessas condições, obtivemos uma nuvem que pode ser apropriada para realizar estudos de efeitos coletivos, podendo transicionar desde o regime diluído até o regime denso.

Os primeiros experimentos realizados, uma vez preparado nosso ensemble atômico, consistem em medir a transmissão coerente de um feixe de baixa intensidade pela nuvem. Para isso, é usada uma luz incidente próxima da ressonância de uma transição dipolar do tipo $J = 0 \leftrightarrow J = 1$ do ^{88}Sr, que interage com uma região homogênea da amostra. Simulações desse tipo de processo podem ser realizadas usando o Modelo de Dipolos Acoplados, o qual descreve a resposta total do espalhamento da luz pela amostra considerando as interações dipolo-dipolo mediadas pela luz. Com este trabalho, pretendemos avançar no entendimento dos efeitos de densidade, realizando uma comparação entre a resposta coerente óptica da nuvem densa e a teoria baseada no Modelo de Dipolos Acoplados.

Palavras-chave: Regime denso. Armadilha óptica de dipolo. Modelo de dipolos acoplados.

LIST OF FIGURES

CONTENTS

1 INTRODUCTION

Light-matter interaction is a very general phenomena that can be manifested in several ways, being constantly present in life and nature. The vivid colors of the sky seen during sunsets and sunrises, the emergence of rainbows, or even the biochemical reactions that lead to the formation of visual images in the eyes of humans and animals, are just a few examples of effects resulting from the propagation and scattering of light through different types of material media. Due to great diversity of phenomena, there is a difficulty in developing a theoretical description of light-matter interaction for the general case. Instead, there are several models to describe specific situations, but they present limitations, functioning under different regimes of density, intensity, spectral width, geometry or structure of the sample.

In atomic physics, the interaction of light with a single atom have been studied for more than four decades allowing the understanding of processes like emission, absorption, scattering (1) or others related to coherence and quantum interference (2). When transitioning to atomic ensembles, the exploration of light-matter interaction not only allows the continued study of aforementioned phenomena but also leads to the emergence of collective effects (3). Collective effects refer to phenomena that arise when a large number of individual atoms interact collectively with light. The emergence of these phenomena comes from the cooperative behavior of the particles, leading to effects that cannot be explained by considering each atom in isolation (4–6). In ensembles of atoms with sufficiently high density of scatterers, collective effects can lead to cooperative emission, which consist in an enhanced or suppressed emission rate compared to what would be expected if each atom were considered independently. These enhancement or suppression of the emission rate are nothing less that the phenomena known as superradiance and subradiance (7–9), which are one of the most studied collective effects, and can be monitored by measuring the time evolution of the excited collective state population (10). Another phenomenon related to the collective behavior of a group of atoms is the cooperative shift (11), which is a shift in the frequency of the emitted or absorbed light by the atoms.

Collective effects can be studied in various kinds of atomic ensembles, such as thermal atoms (12), Rydberg atoms (13, 14), or atoms inside an optical cavity (15). In particular, the advances in laser cooling and trapping techniques (16–19), have opened the possibility of studying light scattering by a more controlled atomic system that can present low temperatures, low collision rates and the chance of achieving samples with very high spatial densities.

According to the density regime of the atomic sample, which can be dilute or dense, collective effects studies can be divided in two different groups. The dilute regime

is defined by $\rho/k^3 \ll 1$, being ρ the spatial density and k the wave-number associated to the atomic transition, which is directly related to the wavelength of the transition through the expression $\lambda = 2\pi/k$. In 2018, Skipetrov and Sokolov established a criterion for the transition between the diffusive behavior of a point scatterers medium and the emergence of Anderson localization of light (20). This criterion consists in an adaptation of the traditional *Ioffe-Regel criterion* to the context of the scalar approximation of light polarization when describing Anderson localization of light waves in 3D disordered media (21), and represents the most used definition for the dense regime by the expression $\rho/k^3 \gtrsim 0.08$, which can also be expressed as $\rho\lambda^3 \gtrsim 20$. Defining the scattering mean free path ℓ_s as the average distance over which a moving particle travels before substantially changing its direction or energy, which in our specific context can be understood as the typical distance between two consecutive scattering events, the Ioffe-Regel criterion also leads to $k\ell_s < 1$ for the dense regime. The product $k\ell_s$ is a quantification of the number of oscillations of light between two scattering events (22–24). Therefore, $k\ell_s < 1$ indicates a condition where the light scattered by a scatterer point goes to the next scattering event before completing one oscillations, which violates the classical nature of wave transport. The phenomena of light diffusion by an atomic ensemble and Anderson localization will be tackled soon in this introduction.

The collective effects, in essence, need more than one atom interacting with the same light mode. In the past the majority of the experiments focuses on achieving this through the production of atomic samples with high optical depths. For this thesis, we would like to study this problem from the perspective of high spatial density samples. The investigation of the dense regime could have some practical applications and would allow for a better understanding of some processes. In biological science, the propagation of light in diffusive media can be applied for imaging biological tissues (25–27), being very relevant for medical diagnostic methods. Also, mechanisms as photosynthesis, which is responsible for the production of food and oxygen in ecosystems, can be understood as coherent effects of the interaction between light and matter in systems that capture light energy (28). In the context of quantum memories, it has been demonstrated that increasing the density of the storage medium (usually a cold atomic sample (29)) produces an improvement of the storage efficiency (30, 31), but also can brings about additional quantum noise that degrades the storage fidelity (32).

In general, collective effects of light scattering in the regime of high densities, are largely unknown. Different from the dilute regime, easier to achieve experimentally, the dense regime has been little studied and the existing models show qualitative discrepancies with the few available experimental observations (8, 33, 34). These discrepancies are mostly subject to complications due to the dense regime, where the short-range interactions between the scatterers within the atomic ensemble can lead to the observation of important modifications in collective effects. The main goal of this PhD research is to explore the

particular case of light-matter interaction in dense samples. Basically, we propose to advance the construction of a fundamental understanding of the processes underlying light scattering by dense samples through an experimental investigation that is as straight forward as possible, aiming to unequivocally isolate the effects of density.

In order to complement the motivation of this work, and specify the contribution of this work to the field, we will make a review of some concepts in the following sections.

1.1 Light diffusion in atomic samples

The propagation of light by a cold atomic cloud with a large number of scatterers, gives place to a multiple scattering process (35), in which a photon undergoes successive scattering events by multiple atoms within the ensemble. When light travels distances much larger than the mean free path, the incoming wave that polarize an atom can be re-emitted and polarize another atom. If this random process is repeated many times, the transport of the light wave through the sample becomes diffusive on average (36). In this situation, the resulting light scattered by the whole atomic system will be given by the interference of the electric fields scattered independently, and the propagation of light can be described by a classical equation of diffusion (37):

$$\frac{\partial \phi(\mathbf{r},t)}{\partial t} = D_B \ \Delta\phi(\mathbf{r},t) - \gamma \ \phi(\mathbf{r},t) + S(\mathbf{r},t) \ , \tag{1.1}$$

where $\phi(\mathbf{r},t)$ represents the local intensity of light within the sample, $S(\mathbf{r},t)$ is a term describing the incident light, D_B is the Boltzmann diffusion constant and γ is the absorption rate of light by the medium. The absorption rate is different than zero if the medium scatters part of the absorbed incident light in an inelastic way, producing a non conservation of energy in the local system. For cold atomic ensembles, absorption rate is usually zero ($\gamma = 0$).

The Boltzmann diffusion constant is particularly relevant in the study of transport phenomena in gases, where particles undergo random motion and collisions. This constant is related to the mean free path of light energy transport through the particles of the atomic gas and the average velocity of this transport, by the expression:

$$D_B = \frac{v\ell_t}{3} \ . \tag{1.2}$$

In general, the ℓ_t is not necessary equal to the scattering mean free path ℓ_s. Indeed, $\ell_t > \ell_s$ when the scattering process in not isotropic (38).

1.2 Anderson localization of light

As mentioned above, the Ioffe-Regel criterion represents the transition between light diffusion and Anderson localization, while increasing the density of point scatterers.

Anderson localization of light can be understood as a phenomenon where the propagation of light through a disordered medium becomes highly localized, which means that the scattered light will not spread over large distances. The name of this effect was after the physicist Philip W. Anderson proposed the idea in the context of electron transport in disordered systems (39). After the discovering, many works have been published reporting the observation of Anderson localization in different kind of systems (40).

For systems where $k\ell_s >> 1$, the equation 1.1 is valid to describe the transport of light. When the scattering mean free path is decreased until $k\ell_s < 1$, destructive interference between the many possible diffusion paths start to be important, giving place to a reduction of the diffusion constant, following the expression:

$$D \sim D_B \left(1 - \frac{1}{(k\ell_s)^2}\right) . \tag{1.3}$$

This reduction can eventually produce a total suppression of the light diffusion, presenting the Anderson localization phenomena when $D = 0$.

The emergence of Anderson localization of light by 1D and 2D atomic systems, have been theoretically predicted and experimentally verified (41). However, the attempts of experimental observations in 3D dense atomic samples, have been a failure showing non conclusive results. Theoretical simulations in these kind of systems predicts the absence of Anderson Localization (42). The reason seems to be related to the vectorial nature of light polarization, which induces additional terms in the interaction between one dipole and the near field produced by the neighbour scatterers, allowing to couple new polarization channels that open new paths for the escaping of light. Probing the effects of this vectorial nature of light scattering is part of this work.

1.3 Coherent transmission by dense samples

A way to detect density effects of an atomic ensemble can be done by measuring the coherent transmission spectrum by a near resonant low-intensity light. The coherent transmission represents the projection of the total electric field, which is the sum of the incident plus the emitted one, in the mode of the incident light beam. In other words, the coherent transmission will indicate how much of the spatial mode of the incident light passes through the atomic sample, preserving the original phase and polarization state.

In the dilute regime, the coherent transmission can be fully explained by the Coupled-Dipole Model, which describes the total response of the cloud by considering dipole-dipole interactions induced by the light (43–48). These dipole-dipole interactions occur when the electric dipole moment induced by the light in one atom influences the electric dipole moments of nearby atoms, leading to cooperative effects among the dipoles in the atomic ensemble. The Coupled-Dipole Model is a classical description since the

atomic dipoles have a linear response to the incident laser field and to the light scattered by all the other dipoles.

Coherent transmission of light by dense atomic samples was investigated using ^{87}Rb, observing that the Coupled-Dipole Model does not explain the behavior experimentally observed in the dense regime (34, 49). However, the levels structure of ^{87}Rb, with a degenerate ground state, makes it not ideal to execute this kind of study. It is thus fundamental to test this model with a simpler dipolar transition (a $J = 0 \leftrightarrow J = 1$ one) as considered in the theoretical calculations. In this ideal condition, we should observe a correspondence between experiments and theory, or identify the necessity of including other effects on the model, such as atomic motion or other effects not previously considered by the community.

1.4 Content of this thesis

In our lab, we cool and trap ^{88}Sr atoms. In this atomic species we can find, among lots of interesting properties that will be discussed over the text, the presence of $J = 0 \leftrightarrow J = 1$ dipolar transitions. This makes the ^{88}Sr perfect for studies of light scattering and compare the results with the predictions of the Coupled-Dipole Model.

In this thesis, we propose an experimental setup for obtaining a dense atomic cloud of ^{88}Sr, which is the most abundant isotope of Strontium. We first trap the atoms by using a Magneto Optical Trap and afterwards we want to transfer them to a tight Optical Dipole Trap, obtaining the density needed for observing collective effects in the dense regime. Once in the atomic dense regime, we are interested in studying, at first, the coherent transmission of low intensity light by this cloud and search for signatures of density effects in our system. Then, our plan is to continue studying the emergence of non-classical correlations by measuring the $g^{(2)}(\tau)$ correlation function (50) and searching for signatures of the absence of Anderson Localization of light in 3D systems.

This PhD work is focused on the first part of this dense regime studies: obtaining a dense atomic cloud, and then performing coherent transmission measurements. The objectives of this project can be summarized as:

- Implementation and characterization of a dense atomic cloud trapped in an Optical Dipole Trap.
- Perform simulations based on the Coupled-Dipole Model.
- Measure coherent transmission spectra.

This document will resume the progress for the implementation of an experimental setup that allows the realization of collective effects studies. Chapter 2 will introduce

some important concepts and the mathematical description of the Coupled-Dipole Model. Chapter 3 and 4 will present our experimental setup for cooling and trapping, describing the implemented system to obtain an ultracold cloud and achieving the regime of high density. Chapter 5 will show some simulations of coherent transmission spectra in the context of the Coupled-Dipole Model calculations, trying to model our real experimental conditions. The experimental implementation of coherent transmission measurements, will be presented at Chapter 6, where also will be shown our results about the presence of density effects in our atomic system. Chapter 7 will show the conclusions and future perspectives towards the achievement of the objectives of our research group.

2 LIGHT-MATTER INTERACTION

In this first chapter we will review the most important aspects of the coherent interaction between electromagnetic radiation and atomic systems. For this, we are going to introduce the mathematical formalism to theoretically describe our system. In the first part, we are considering the case of the light interacting with a single atom, but then we generalize to the many atoms systems situation. In that second part, we deduce the basic equations of the Coupled Dipole Model and discuss some of the approximations made to find them.

2.1 Single Atom

Let us consider a simple situation of one atom with center of mass at the position $\mathbf{R} = (x, y, z)$ interacting with a laser field. The radiation field is a monochromatic laser with frequency ω_l and the atom has its transition from the ground state to an excited level of natural frequency ω_0. If the atomic transition is closed and $|\omega_l - \omega_0| << \omega_l, \omega_0$, the excitation probability for another atomic level is very low; so basically, we are considering a two-level atom interacting with a laser field that can produce transitions from the ground state $|g\rangle$ to an excited level $|e\rangle$. An important statement in this first situation that we are considering is that light is going to be treated as a scalar wave, which means that only the intensity and phase are considered, but the polarization state of the light is not explicitly taken into account.

In these simplified conditions, putting the origin of energies in the energy of the ground state, we can write the Hamiltonian for the free atom as follows:

$$\hat{\mathcal{H}}_0 = \hbar\omega_0 |e\rangle\langle e| = \hbar\omega_0 \hat{\sigma}^+ \hat{\sigma}^- \ , \tag{2.1}$$

where $\hat{\sigma}^+ = |e\rangle\langle g|$ and $\hat{\sigma}^- = |g\rangle\langle e|$, are respectively the raising and lowering operators for the transition $|g\rangle \leftrightarrow |e\rangle$.

Assuming the wavelength of the incident field much greater than the atomic dimensions, the Hamiltonian of the interaction between the electromagnetic radiation and the atom in the first order is given by the *electric dipole approximation*, mediated by the electric dipole operator,

$$\hat{\mathcal{H}}_i = - \hat{\mathbf{d}} \cdot \mathbf{E}_l(\mathbf{R}) \ . \tag{2.2}$$

The electric dipolar approximation allows us to neglect higher-order terms for the coupling between the atom and the radiation, such as magnetic dipolar and electric quadrupolar, which are at least of order $a_0/\lambda \approx 10^{-4}$ (a_0 is the Bohr radius) with respect to the electric dipolar moment. In this case, for an electric-dipole-allowed atomic transition,

the electric dipole operator $\hat{\mathbf{d}}$ is given by

$$\hat{\mathbf{d}} = d\ |g\rangle\langle e|\boldsymbol{\epsilon} + h.c. = d\ \hat{\sigma}^{-}\boldsymbol{\epsilon} + d^{*}\ \hat{\sigma}^{+}\boldsymbol{\epsilon}^{*}\ , \tag{2.3}$$

where $\boldsymbol{\epsilon}$ is an unitary vector in the direction of the induced electric dipole and d is the scalar matrix element of the electric dipole moment between the ground and excited level. For the scalar model, the induced dipole is in the same direction as the incoming electric field, so $\boldsymbol{\epsilon} = \boldsymbol{\epsilon}_l$ where $\boldsymbol{\epsilon}_l$ is the unitary vector that represents the polarization of the incoming beam.

The electric field for the incoming laser, considered in equation (2.2), that we assume as being classical due to the high average number of photons of the laser beam, can be written as

$$\mathbf{E}_l(\mathbf{R}) = \mathrm{Re}\Big[E_l(\mathbf{R})e^{-i\omega_l t}\boldsymbol{\epsilon}_l\Big]\ , \tag{2.4}$$

where $E_l(\mathbf{R})$ is the scalar electric field amplitude.

Finally, the total Hamiltonian of the system can be expressed as follows:

$$\hat{\mathcal{H}} = \hat{\mathcal{H}}_0 + \hat{\mathcal{H}}_i = \hbar\omega_0\hat{\sigma}^{+}\hat{\sigma}^{-} - \frac{1}{2}\left(d\ \hat{\sigma}^{-}\boldsymbol{\epsilon} + d^{*}\ \hat{\sigma}^{+}\boldsymbol{\epsilon}^{*}\right)\left(E_l(\mathbf{R})e^{-i\omega_l t}\boldsymbol{\epsilon}_l + E_l^{*}(\mathbf{R})e^{i\omega_l t}\boldsymbol{\epsilon}_l^{*}\right)\ . \tag{2.5}$$

In this expression for the total Hamiltonian there are some anti-resonant terms that we can neglect with no physical consequences since they induce fast and small-amplitude oscillations that averages out in the typical timescales of observation of the physical system. The elimination of these terms is an approximation known as *rotating wave approximation* (RWA) (51). A way to find these non-resonant terms is to redefine new operators in a rotating reference frame:

$$\hat{\beta}^{-} = e^{i\omega_l t}\hat{\sigma}^{-}$$
$$\hat{\beta}^{+} = e^{-i\omega_l t}\hat{\sigma}^{+}\ .$$

These expressions replace the atomic coherences by new operators, in a reference frame that rotates with the phase of the incoming laser light; basically, we are considering that for quasi-resonant excitation, the coherences induced in the system oscillates with a frequency close to the frequency of the radiation field exciting the atomic transition. Separating the time-dependence of the atomic coherences, we can consider the new operators have a slow variation on time.

Replacing the atomic coherences in equation (2.5) by the new ones and considering a quasi-resonant excitation, we can perform the RWA neglecting the terms that oscillate with frequencies $2\omega_l$ since their temporal average is $\langle e^{i2\omega_l t}\rangle = 0$. In this way, we obtain a new expression for the total Hamiltonian given by

$$\hat{\mathcal{H}} = \ \hbar\omega_0\hat{\beta}^{+}\hat{\beta}^{-} - \frac{\hbar}{2}\left[\Omega(\mathbf{R})\ \hat{\beta}^{-} + \Omega^{*}(\mathbf{R})\ \hat{\beta}^{+}\right]\ . \tag{2.6}$$

Here $\Omega(\mathbf{R}) = \frac{d^* E_l(\mathbf{R})}{\hbar}$ is the Rabi frequency of the coupling between the incoming light and the atomic transition. Note that we used $\boldsymbol{\epsilon} \cdot \boldsymbol{\epsilon}_l = 1$, which is only true in the context of the scalar model of light.

We are now interested in calculating the time derivative of the operators $\hat{\beta}^-$ and $\hat{\beta}^+$ in the Heisenberg representation. For that we are going to apply the following equation for any operator $\hat{A}$

$$\frac{d\hat{A}}{dt} = \frac{i}{\hbar}\left[\hat{\mathcal{H}}, \hat{A}\right] + \frac{\partial \hat{A}}{\partial t} \ , \tag{2.7}$$

and, using the commutation relations:

$$\left[\hat{\beta}^-, \hat{\beta}^-\right] = \left[\hat{\beta}^+, \hat{\beta}^+\right] = 0$$
$$\left[\hat{\beta}^-, \hat{\beta}^+\right] = |g\rangle\langle g| - |e\rangle\langle e| \ ,$$

we obtain:

$$\frac{d\hat{\beta}^-}{dt} = i\Delta\hat{\beta}^- + \frac{i\Omega}{2} \tag{2.8}$$
$$\frac{d\hat{\beta}^+}{dt} = \left(\frac{d\hat{\beta}^-}{dt}\right)^\dagger \ , \tag{2.9}$$

where the parameter $\Delta = \omega_l - \omega_0$ represents the detuning of the laser with respect to the atomic resonance. Note that here we considered a new approximation: we put ourselves in the *linear regime limit*, i.e. supposing that the population of the excited state is much smaller than one, so we have $|g\rangle\langle g| - |e\rangle\langle e| \approx 1$. This means that we neglected saturation effects of the atomic transition, such as saturation broadening of the transition, or a non-linear dependence of the susceptibility of the atomic cloud on the electric field of the incoming light.

The restriction to describing only the atom and the laser field and not the light spontaneously emitted in arbitrary directions with arbitrary polarization results in a huge simplification. Also the spontaneous emission cannot be properly handled within the framework of the classical description for the electromagnetic field that was done until now. The true nature of the spontaneous emission process emerges from the Wigner-Weisskopf theory in which it is shown that an atom in the excited state decays exponentially as a result of the fluctuations of the quantized vacuum field. Details about this theory will be presented in the next section.

2.2 Many Atoms

2.2.1 Hamiltonian of the system

Let us consider now an ensemble of $\mathbf{N}$ identical atoms with frequency ω_0 and each atom j with center of mass at the position $\mathbf{R}_j = (x_j, y_j, z_j)$. As can be seen in figure 1, we

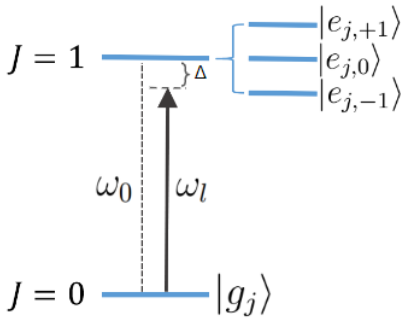

Figure 1 – Interaction between a light field and a simple dipolar transition $J = 0 \leftrightarrow J = 1$, with detuning $\Delta = \omega_l - \omega_0$.

Source: By the author.

have a similar situation as the one on the single atom case, but now we are not considering a two-level system. Instead, we have a laser field with frequency ω_l close to the resonance of a simple dipolar transition $J = 0 \leftrightarrow J = 1$, from a nondegenerate ground level $|g_j\rangle$ to the degenerate excited level, composed of three sublevels, with angular momentum in the $+z$ direction equal to -1, 0 and $+1$, given respectively by $|e_{j,-1}\rangle$, $|e_{j,0}\rangle$ and $|e_{j,+1}\rangle$. In this case, the transition amplitudes for the atoms depend on the light polarization: light with σ^+ polarization (with respect to z axis) will only excite the transition $|g_j\rangle \leftrightarrow |e_{j,+1}\rangle$, while light with σ^- polarization excites only the transition $|g_j\rangle \leftrightarrow |e_{j,-1}\rangle$. Light with linear polarization will excite a specific coherent superposition of the $|e_{j,\pm1}\rangle$ excited levels. The transition $|g_j\rangle \leftrightarrow |e_{j,0}\rangle$ could happen through emission and re-absorption of photons within the atomic cloud or excitation by light with a different propagation direction.

Note that in this new situation, we are not only considering many atoms, but also we are taking into account the full vector nature of the electromagnetic field. This is known as vectorial model of light, and it is more appropriate when the polarization state of the scattered light is important.

For convenience, we replace the basis $\{|e_{j,-1}\rangle, |e_{j,0}\rangle, |e_{j,+1}\rangle\}$ by $\{|e_{j,x}\rangle, |e_{j,y}\rangle, |e_{j,z}\rangle\}$ for the excited states. In this new basis, the description of the linear polarization is simplified: light polarized in the x direction will excite only the atomic transition $|g_j\rangle \leftrightarrow |e_{j,x}\rangle$ while light polarized in y excite the transition $|g_j\rangle \leftrightarrow |e_{j,y}\rangle$. This states are written as a function of the former ones as follows

$$|e_{j,x}\rangle = -\frac{|e_{j,+1}\rangle - |e_{j,-1}\rangle}{\sqrt{2}}$$
$$|e_{j,y}\rangle = i\frac{|e_{j,+1}\rangle + |e_{j,-1}\rangle}{\sqrt{2}}$$
$$|e_{j,z}\rangle = |e_{j,0}\rangle$$

In this situation, the raising and lowering operators for the atomic transition

$|g_j\rangle \leftrightarrow |e_{j,\alpha}\rangle$ (with $\alpha = x, y, z$), can be expressed respectively by $\hat{\sigma}^{+}_{j,\alpha} = |e_{j,\alpha}\rangle\langle g_j|$ and $\hat{\sigma}^{-}_{j,\alpha} = |g_j\rangle\langle e_{j,\alpha}|$. In the new basis defined above, we can write the Hamiltonian for the free atoms, as follows:

$$\hat{\mathcal{H}}_0 = \sum_{\substack{j=1...N \\ \alpha=x,y,z}} \hbar\omega_0 \; |e_{j,\alpha}\rangle\langle e_{j,\alpha}| = \sum_{\substack{j=1...N \\ \alpha=x,y,z}} \hbar\omega_0 \; \hat{\sigma}^{+}_{j,\alpha} \; \hat{\sigma}^{-}_{j,\alpha} \; , \tag{2.10}$$

Processes as spontaneous emission and re-absorption of photons by neighbours atoms are relevant for the study of atomic ensembles. Those are mediated by the free quantized vacuum modes of the electromagnetic field, where their free Hamiltonian is composed by the sum of the energy of all vacuum modes, as we can see below:

$$\hat{\mathcal{H}}_{EM} = \sum_{\mathbf{k},\boldsymbol{\epsilon}} \hbar\omega_k \; \hat{a}^{\dagger}_{\mathbf{k},\boldsymbol{\epsilon}} \; \hat{a}_{\mathbf{k},\boldsymbol{\epsilon}} \; . \tag{2.11}$$

Here $\hat{a}_{\mathbf{k},\boldsymbol{\epsilon}}$ and $\hat{a}^{\dagger}_{\mathbf{k},\boldsymbol{\epsilon}}$ are the annihilation and creation operators of a photon in the mode determined by the wavevector $\mathbf{k}$ and frequency $\omega_k = ck$; $\boldsymbol{\epsilon}$ is an unitary vector pointing at the polarization direction of the mode. In this Hamiltonian we eliminated the constant term $\sum_{\mathbf{k},\boldsymbol{\epsilon}} \frac{\hbar\omega_k}{2}$ with no physical consequence for our problem since effects related with the zero-point energy in vacuum (as the Casimir effect) are not relevant for the physical phenomena we are studying.

Using again the electric dipole approximation to obtain the Hamiltonian of the interaction between the electromagnetic radiation and the atoms, we have:

$$\hat{\mathcal{H}}_i = - \sum_{j=1...N} \hat{\mathbf{d}}_j \cdot \Big(\hat{\mathbf{E}}(\mathbf{R}_j) + \mathbf{E}_l(\mathbf{R}_j) \Big) \; , \tag{2.12}$$

and this time the electric dipole operator for each atom $\hat{\mathbf{d}}_j$ is given by:

$$\hat{\mathbf{d}}_j = \sum_{\alpha=x,y,z} \Big[d \; |g_j\rangle\langle e_{j,\alpha}| \boldsymbol{\epsilon}_\alpha + \text{h.c.} \Big] = \sum_{\alpha=x,y,z} \Big[d \; \hat{\sigma}^{-}_{j,\alpha} \boldsymbol{\epsilon}_\alpha + \text{h.c.} \Big] \; , \tag{2.13}$$

where $\boldsymbol{\epsilon}_\alpha$ is an unitary vector in the α direction. We see that the electric dipolar moment in the x (respectively y,z) direction couples only the ground state to the $|e_{j,x}\rangle$ (respectively $|e_{j,y}\rangle$, $|e_{j,z}\rangle$) excited state.

In the expression for $\hat{\mathcal{H}}_i$ we have separated the electric field of light in two components: $\hat{\mathbf{E}}(\mathbf{R}_j)$ the electric field operator of the quantized electromagnetic radiation at the position $\mathbf{R}_j$ and $\mathbf{E}_l(\mathbf{R}_j)$ the electric field for the incoming coherent monochromatic laser light. The first one can be written as

$$\hat{\mathbf{E}}(\mathbf{R}_j) = i \sum_{\mathbf{k},\boldsymbol{\epsilon}} \sqrt{\frac{\hbar\omega_k}{2\varepsilon_0 V}} \Big(\hat{a}_{\mathbf{k},\boldsymbol{\epsilon}} \; \boldsymbol{\epsilon} \; e^{i\mathbf{k}\cdot\mathbf{R_j}} + \hat{a}^{\dagger}_{\mathbf{k},\boldsymbol{\epsilon}} \; \boldsymbol{\epsilon}^{*} e^{-i\mathbf{k}\cdot\mathbf{R_j}} \Big) \; , \tag{2.14}$$

where ε_0 is the vacuum permittivity and V is a quantization volume; an artificial volume into which the quantized electromagnetic modes are obtained, that is made equal to infinity at the end of calculations if the system is in free space (52).

The electric field for the incoming laser, due to its approximation to a coherent state, it is exactly the same as the one considered in the single atom case (equation (2.4)):

$$\mathbf{E}_l(\mathbf{R}_j) = \frac{E_l(\mathbf{R}_j)e^{-i\omega_l t}\boldsymbol{\epsilon}_l + E_l^*(\mathbf{R}_j)e^{i\omega_l t}\boldsymbol{\epsilon}_l^*}{2} \ . \tag{2.15}$$

Note that here we can represent different configurations for the polarization of the incident light: a linear polarization in the x direction by $\boldsymbol{\epsilon}_l = \boldsymbol{\epsilon}_x$, or a right-hand circular polarization by $\boldsymbol{\epsilon}_l = -(\boldsymbol{\epsilon}_x + i\boldsymbol{\epsilon}_y)/\sqrt{2}$. For instance, if we consider the excitation laser light as a plane wave, the scalar electric field amplitude is simply given by a constant value: $E_l(\mathbf{R}) = E_0$. In the real experimental conditions we are interested in a Gaussian profile of the laser, but the details about it are going to be discussed in Chapters 5 and 6.

Finally, the total Hamiltonian of the system composed by $\mathbf{N}$ atoms interacting with an incoming laser and the quantized vacuum field, can be expressed as follows:

$$\begin{aligned}\hat{\mathcal{H}} = \hat{\mathcal{H}}_0 + \hat{\mathcal{H}}_{EM} + \hat{\mathcal{H}}_i = \sum_{\substack{j=1\ldots N\\ \alpha=x,y,z}} \Big[\hbar\omega_0 \hat{\sigma}^+_{j,\alpha}\hat{\sigma}^-_{j,\alpha} - \frac{1}{2}\left(d\ \hat{\sigma}^-_{j,\alpha}\boldsymbol{\epsilon}_\alpha + d^*\ \hat{\sigma}^+_{j,\alpha}\boldsymbol{\epsilon}^*_\alpha\right) \\ \left(E_l(\mathbf{R}_j)e^{-i\omega_l t}\boldsymbol{\epsilon}_l + E_l^*(\mathbf{R}_j)e^{i\omega_l t}\boldsymbol{\epsilon}_l^*\right)\Big] + \sum_{\mathbf{k},\boldsymbol{\epsilon}} \hbar\omega_k\ \hat{a}^\dagger_{\mathbf{k},\boldsymbol{\epsilon}}\ \hat{a}_{\mathbf{k},\boldsymbol{\epsilon}} \\ - i \sum_{\substack{j=1\ldots N\\ \alpha=x,y,z}} \sum_{\mathbf{k},\boldsymbol{\epsilon}} \sqrt{\frac{\hbar\omega_k}{2\varepsilon_0 V}} \Big[d\ e^{i\mathbf{k}\cdot\mathbf{R}_j}\ \hat{\sigma}^-_{j,\alpha}\ \hat{a}_{\mathbf{k},\boldsymbol{\epsilon}}\ \boldsymbol{\epsilon}_\alpha\cdot\boldsymbol{\epsilon} + d^* e^{i\mathbf{k}\cdot\mathbf{R}_j}\ \hat{\sigma}^+_{j,\alpha}\ \hat{a}_{\mathbf{k},\boldsymbol{\epsilon}}\ \boldsymbol{\epsilon}^*_\alpha\cdot\boldsymbol{\epsilon} \\ + d\ e^{-i\mathbf{k}\cdot\mathbf{R}_j}\ \hat{\sigma}^-_{j,\alpha}\ \hat{a}^\dagger_{\mathbf{k},\boldsymbol{\epsilon}}\ \boldsymbol{\epsilon}_\alpha\cdot\boldsymbol{\epsilon}^* + d^* e^{-i\mathbf{k}\cdot\mathbf{R}_j}\ \hat{\sigma}^+_{j,\alpha}\ \hat{a}^\dagger_{\mathbf{k},\boldsymbol{\epsilon}}\ \boldsymbol{\epsilon}^*_\alpha\cdot\boldsymbol{\epsilon}^*\Big] \ ,\end{aligned} \tag{2.16}$$

We can apply again the RWA, this time separating the time-dependence not only for the atomic coherences, but also for the radiation operators, so the new operators can be redefined as follows:

$$\begin{aligned}\hat{\beta}^-_{j,\alpha} &= e^{i\omega_l t}\hat{\sigma}^-_{j,\alpha} \\ \hat{\beta}^+_{j,\alpha} &= e^{-i\omega_l t}\hat{\sigma}^+_{j,\alpha} \\ \hat{b}_{\mathbf{k},\boldsymbol{\epsilon}} &= e^{i\omega_k t}\hat{a}_{\mathbf{k},\boldsymbol{\epsilon}} \\ \hat{b}^\dagger_{\mathbf{k},\boldsymbol{\epsilon}} &= e^{-i\omega_k t}\hat{a}^\dagger_{\mathbf{k},\boldsymbol{\epsilon}} \quad .\end{aligned}$$

Neglecting the terms that oscillate with frequencies $\omega_l + \omega_k$ and $2\omega_l$, the new Hamiltonian of the system is

$$\begin{aligned}\hat{\mathcal{H}}_N = \sum_{\substack{j=1\ldots N\\ \alpha=x,y,z}} \Big[\hbar\omega_0\hat{\beta}^+_{j,\alpha}\hat{\beta}^-_{j,\alpha} - \frac{\hbar}{2}\left(\Omega_{j,\alpha}\ \hat{\beta}^-_{j,\alpha} + \Omega^*_{j,\alpha}\ \hat{\beta}^+_{j,\alpha}\right)\Big] + \sum_{\mathbf{k},\boldsymbol{\epsilon}} \hbar\omega_k\ \hat{b}^\dagger_{\mathbf{k},\boldsymbol{\epsilon}}\ \hat{b}_{\mathbf{k},\boldsymbol{\epsilon}} \\ - i\hbar \sum_{\substack{j=1\ldots N\\ \alpha=x,y,z}} \sum_{\mathbf{k},\boldsymbol{\epsilon}} \Big[g^*_{\mathbf{k},\boldsymbol{\epsilon},\alpha}\ e^{i\mathbf{k}\cdot\mathbf{R}_j} e^{i(\omega_l-\omega_k)t}\hat{\beta}^+_{j,\alpha}\hat{b}_{\mathbf{k},\boldsymbol{\epsilon}} + g_{\mathbf{k},\boldsymbol{\epsilon},\alpha}\ e^{-i\mathbf{k}\cdot\mathbf{R}_j} e^{i(\omega_k-\omega_l)t}\hat{\beta}^-_{j,\alpha}\hat{b}^\dagger_{\mathbf{k},\boldsymbol{\epsilon}}\Big] \ ,\end{aligned} \tag{2.17}$$

with $\Omega_\alpha(\mathbf{R}_j) = \frac{d^* E_l(\mathbf{R}_j)}{\hbar}\boldsymbol{\epsilon}_\alpha^* \cdot \boldsymbol{\epsilon}_l$ the Rabi frequency of the coupling between the incoming light and the atomic transition for each atom, and $g_{\mathbf{k},\boldsymbol{\epsilon},\alpha} = d\sqrt{\frac{\omega_k}{2\hbar\varepsilon_0 V}}\boldsymbol{\epsilon}_\alpha \cdot \boldsymbol{\epsilon}^*$ is the Rabi frequency of the scalar coupling between the atomic transition and a vacuum electromagnetic mode.

An interesting thing to highlight about the RWA is that this approximation eliminated the terms proportional to $\hat{\sigma}_{j,\alpha}^+ \hat{a}_{\mathbf{k},\boldsymbol{\epsilon}}^\dagger$ and $\hat{\sigma}_{j,\alpha}^- \hat{a}_{\mathbf{k},\boldsymbol{\epsilon}}$. They describe the situations where the atom is excited and a photon is created in the mode $(\mathbf{k}, \boldsymbol{\epsilon})$, or the atom is de-excited and a photon is eliminated in the mode $(\mathbf{k}, \boldsymbol{\epsilon})$, which clearly violates the energy conservation.

2.2.2 Vectorial Coupled Dipole Model (CDM)

In order to continue the mathematical treatment to obtain the equations that couples all the electrical dipole moments induced in the atomic system, we will use the equation (2.7) to calculate the time derivative of the operators $\hat{\beta}_{j,\alpha}^-$, $\hat{\beta}_{j,\alpha}^+$, $\hat{b}_{\mathbf{k},\boldsymbol{\epsilon}}$ and $\hat{b}_{\mathbf{k},\boldsymbol{\epsilon}}^\dagger$ in the Heisenberg representation.

The atomic operators: $\hat{\beta}_{j,\alpha}^-$ and $\hat{\beta}_{j,\alpha}^+$, and the radiation operators: $\hat{b}_{\mathbf{k},\boldsymbol{\epsilon}}$ and $\hat{b}_{\mathbf{k},\boldsymbol{\epsilon}}^\dagger$ follow the commutation relations:

$$
\begin{aligned}
&\left[\hat{\beta}_{j,\alpha}^-, \hat{\beta}_{j',\alpha'}^-\right] = \left[\hat{\beta}_{j,\alpha}^+, \hat{\beta}_{j',\alpha'}^+\right] = 0 \\
&\left[\hat{\beta}_{j,\alpha}^-, \hat{\beta}_{j',\alpha'}^+\right] = \delta_{j,j'}\delta_{\alpha,\alpha'}\Big(|g_j\rangle\langle g_j| - |e_{j,\alpha}\rangle\langle e_{j,\alpha}|\Big) \\
&\left[\hat{b}_{\mathbf{k},\boldsymbol{\epsilon}}, \hat{b}_{\mathbf{k}',\boldsymbol{\epsilon}'}\right] = \left[\hat{b}_{\mathbf{k},\boldsymbol{\epsilon}}^\dagger, \hat{b}_{\mathbf{k}',\boldsymbol{\epsilon}'}^\dagger\right] = 0 \\
&\left[\hat{b}_{\mathbf{k},\boldsymbol{\epsilon}}, \hat{b}_{\mathbf{k}',\boldsymbol{\epsilon}'}\right] = \delta_{\mathbf{k},\mathbf{k}'}\delta_{\boldsymbol{\epsilon},\boldsymbol{\epsilon}'} \\
&\left[\hat{\beta}_{j,\alpha}^-, \hat{b}_{\mathbf{k},\boldsymbol{\epsilon}}\right] = \left[\hat{\beta}_{j,\alpha}^-, \hat{b}_{\mathbf{k},\boldsymbol{\epsilon}}^\dagger\right] = \left[\hat{\beta}_{j,\alpha}^+, \hat{b}_{\mathbf{k},\boldsymbol{\epsilon}}\right] = \left[\hat{\beta}_{j,\alpha}^+, \hat{b}_{\mathbf{k},\boldsymbol{\epsilon}}^\dagger\right] = 0 \ .
\end{aligned}
$$

Using these properties for the operators and considering the linear regime limit, we find the equations for the evolution of the operators in the Heisenberg picture:

$$
\frac{d\hat{\beta}_{j,\alpha}^-}{dt} = i\Delta\hat{\beta}_{j,\alpha}^- + \frac{i\Omega_{j,\alpha}}{2} - \sum_{\mathbf{k},\boldsymbol{\epsilon}} g_{\mathbf{k},\boldsymbol{\epsilon},\alpha}^*\ e^{i\mathbf{k}\cdot\mathbf{R}_j} e^{i(\omega_l-\omega_k)t}\hat{b}_{\mathbf{k},\boldsymbol{\epsilon}}\ , \tag{2.18}
$$

$$
\frac{d\hat{b}_{\mathbf{k},\boldsymbol{\epsilon}}}{dt} = \sum_{\substack{j=1\ldots N \\ \alpha=x,y,z}} g_{\mathbf{k},\boldsymbol{\epsilon},\alpha}\ e^{-i\mathbf{k}\cdot\mathbf{R}_j} e^{i(\omega_k-\omega_l)t}\,\hat{\beta}_{j,\alpha}^-\ , \tag{2.19}
$$

$$
\frac{d\hat{\beta}_{j,\alpha}^+}{dt} = \left(\frac{d\hat{\beta}_{j,\alpha}^-}{dt}\right)^\dagger , \tag{2.20}
$$

$$
\frac{d\hat{b}_{\mathbf{k},\boldsymbol{\epsilon}}^\dagger}{dt} = \left(\frac{d\hat{b}_{\mathbf{k},\boldsymbol{\epsilon}}}{dt}\right)^\dagger . \tag{2.21}
$$

Note that here, the equations for the time evolution of the atomic coherences are similar to the ones obtained for the single atom situation (equations (2.8) and (2.9)) if we neglect, in the many atoms case, the interaction between the atoms and the vacuum field modes.

We can now replace the two linear differential equations (2.18) and (2.19) by one differential-integral equation. For that we integrate equation (2.19) in order to find a formal solution for the operator $\hat{b}_{\mathbf{k},\boldsymbol{\epsilon}}$,

$$\hat{b}_{\mathbf{k},\boldsymbol{\epsilon}}(t) = \hat{b}_{\mathbf{k},\boldsymbol{\epsilon}}(0) + \sum_{\substack{j=1\ldots N \\ \alpha=x,y,z}} g_{\mathbf{k},\boldsymbol{\epsilon},\alpha} e^{-i\mathbf{k}\cdot\mathbf{R}_j} \int_0^t dt' e^{i(\omega_k-\omega_l)t'} \hat{\beta}^-_{j,\alpha}(t') \ , \tag{2.22}$$

and then, replacing this solution in equation (2.18), we obtain

$$\frac{d\hat{\beta}^-_{j,\alpha}}{dt} = i\Delta\hat{\beta}^-_{j,\alpha} + \frac{i\Omega_{j,\alpha}}{2} - \sum_{\mathbf{k},\boldsymbol{\epsilon}} \sum_{\substack{m=1\ldots N \\ \gamma=x,y,z}} g^*_{\mathbf{k},\boldsymbol{\epsilon},\alpha}\ g_{\mathbf{k},\boldsymbol{\epsilon},\gamma}\ e^{i\mathbf{k}\cdot(\mathbf{R}_j-\mathbf{R}_m)} \int_0^t dt' e^{i(\omega_l-\omega_k)(t-t')} \hat{\beta}^-_{m,\gamma}(t') \ . \tag{2.23}$$

The last term of the equation above represents an effective coupling between the operator $\hat{\beta}^-_{j,\alpha}$ and each one of the operators $\hat{\beta}^-_{m,\gamma}$. We can write this term as

$$\mathrm{B}_{j,\alpha,m,\gamma}(t) = \sum_{\mathbf{k},\boldsymbol{\epsilon}} g^*_{\mathbf{k},\boldsymbol{\epsilon},\alpha}\ g_{\mathbf{k},\boldsymbol{\epsilon},\gamma}\ e^{i\mathbf{k}\cdot(\mathbf{R}_j-\mathbf{R}_m)} \int_0^t dt' e^{i(\omega_l-\omega_k)(t-t')} \hat{\beta}^-_{m,\gamma}(t') \ , \tag{2.24}$$

such that equation (2.23) can be expressed as

$$\frac{d\hat{\beta}^-_{j,\alpha}}{dt} = i\Delta\hat{\beta}^-_{j,\alpha} + \frac{i\Omega_{j,\alpha}}{2} - \sum_{\substack{m=1\ldots N \\ \gamma=x,y,z}} \mathrm{B}_{j,\alpha,m,\gamma}(t) \ . \tag{2.25}$$

To calculate the equation (2.24) we apply the so-called *Weisskopf-Wigner treatment* of the coupling between atoms and the modes of the electromagnetic radiation (53). First, we replace the summation over $\mathbf{k}$ by an integral:

$$\sum_{\mathbf{k}} \to \frac{V}{(2\pi)^3} \int_0^\infty dk k^2 \int_0^\pi d\theta \sin\theta \int_0^{2\pi} d\phi \ ;$$

then, in order to solve this integrals, we consider $\omega_k \sim \omega_0$. This approximation relies on the fact that only values of ω_k close enough to ω_l (such the $|\omega_l - \omega_k| \lesssim \frac{1}{|t-t'|}$) will play a role for all t' in the time integration; for all other values, the term $e^{i(\omega_l-\omega_k)(t-t')}$ will quickly average to zero in the time integration.

Another approximation we also performed to solve the integrals mentioned above was the *rapid transit approximation* (also known as *Markov approximation* (54)). This consist in neglecting the retardation effects i.e. consider that the time needed for the light emitted by one atom to travel through the cloud and reach another atom is negligible with respect to all other time scales of the problem. This is only true for small atomic clouds.

The details of the application of the Weisskopf-Wigner treatment and the Markov approximation can be found on Appendix A, and with these calculations we find the following solution for $\mathrm{B}_{j,\alpha,m,\gamma}(t)$:

$$\mathrm{B}_{j,\alpha,m,\gamma}(t) = \frac{\Gamma}{2}\ V_{j,\alpha,m,\gamma}\ \hat{\beta}^-_{m,\gamma}(t) \ , \tag{2.26}$$

where the natural decay rate of the atomic level Γ is given by

$$\Gamma = \frac{d^2\omega_0^3}{3\pi\varepsilon_0\hbar c^3} \ , \tag{2.27}$$

and the adimensional matrix elements $V_{j,\alpha,m,\gamma}$

$$V_{j,\alpha,m,\gamma} = \frac{3}{2}\frac{e^{ik_0R_{jm}}}{ik_0R_{jm}^3}\Big[R_{jm}^2\boldsymbol{\epsilon}_\alpha^*\cdot\boldsymbol{\epsilon}_\gamma - (\mathbf{R}_{jm}\cdot\boldsymbol{\epsilon}_\alpha^*)(\mathbf{R}_{jm}\cdot\boldsymbol{\epsilon}_\gamma) + \left(\frac{i}{k_0R_{jm}} - \frac{1}{(k_0R_{jm})^2}\right)(R_{jm}^2\boldsymbol{\epsilon}_\alpha^*\cdot\boldsymbol{\epsilon}_\gamma - 3(\mathbf{R}_{jm}\cdot\boldsymbol{\epsilon}_\alpha^*)(\mathbf{R}_{jm}\cdot\boldsymbol{\epsilon}_\gamma))\Big] \ , \tag{2.28}$$

$$V_{j,\alpha,j,\gamma} = \delta_{\alpha,\gamma} \tag{2.29}$$

where $\mathbf{R}_{jm} = \mathbf{R}_j - \mathbf{R}_m$ is the vector that goes from atom j to atom m, and R_{jm} is the inter-atomic distance. Here we used the wavenumber associated to the atomic transition defined by $k_0 = \frac{\omega_0}{c}$.

Note that the effective coupling between two atoms (j and m) of the cloud is proportional to three terms: $(k_0R_{j,m})^{-1}$, $(k_0R_{j,m})^{-2}$ and $(k_0R_{j,m})^{-3}$. In the case of dilute atomic clouds (low spatial density), the last two terms, known as *short-range terms*, can be neglected since they are very small in comparison with the *long-range term* $(k_0R_{j,m})^{-1}$ for typical nearest-neighbour distances. However, we are considering all three terms since we are interested in the study of dense atomic clouds.

Replacing equation (2.26) in equation (2.25), we have

$$\frac{d\hat{\beta}_{j,\alpha}^-}{dt} = i\Delta\hat{\beta}_{j,\alpha}^- + \frac{i\Omega_{j,\alpha}}{2} - \frac{\Gamma}{2}\sum_{\substack{m=1\ldots N\\ \gamma=x,y,z}} V_{j,\alpha,m,\gamma}\ \hat{\beta}_{m,\gamma}^- \ , \tag{2.30}$$

which represent a set of effective time evolution equations for the atomic operators only. These equations are known as the **vectorial Coupled Dipole Model** (CDM), because the evolution of each component α of the vectorial dipole moment of atom j is effectively coupled to each component γ of the vectorial dipole moment of each other atom m through the matrix $\mathbf{V}$, of dimension $3N \times 3N$ and elements $V_{j,\alpha,m,\gamma}$.

Once again we can rewrite this set of differential equations in order to explicitly separate its homogeneous and inhomogeneous terms

$$\frac{d\hat{\beta}_{j,\alpha}^-}{dt} = \frac{i\Omega_{j,\alpha}}{2} + \sum_{\substack{m=1\ldots N\\ \gamma=x,y,z}} \mathrm{K}_{j,\alpha,m,\gamma}\ \hat{\beta}_{m,\gamma}^- \ , \tag{2.31}$$

and define here the so-called *kernel of the interaction*, given by

$$\mathrm{K}_{j,\alpha,m,\gamma} = -\frac{\Gamma}{2}\ V_{j,\alpha,m,\gamma} + i\ \Delta\ \delta_{j,m}\ \delta_{\alpha,\gamma} \ , \tag{2.32}$$

which is a $3N \times 3N$ matrix that determines the effective coupling between the atomic dipoles, mediated by the modes of the vacuum field.

2.2.3 The Eigenmodes of the CDM

If we consider, in the equations of the CDM, the absence of laser excitation ($\Omega_{j,\alpha} = 0$) and the absence of coupling between atoms ($\mathrm{K}_{j,\alpha,m,\gamma} = 0$ for $j \neq m$), we have

$$\frac{d\hat{\beta}^-_{j,\alpha}}{dt} = \left(i\Delta - \frac{\Gamma}{2}\right)\hat{\beta}^-_{j,\alpha} \ . \tag{2.33}$$

Here we used the equation (2.29) since the only terms different than zero are the ones for $j = m$ in the $\mathbf{V}$ matrix.

This set of equations has the same solution for each atom since, in absence of coupling between the atoms, each one of them behave as if it was alone in space. The solutions are given by:

$$\hat{\beta}^-_{j,\alpha}(t) = \hat{\beta}^-_{j,\alpha}(0)e^{\left(i\Delta - \frac{\Gamma}{2}\right)t} \ . \tag{2.34}$$

Having an identical behavior, we can understand that: for a single atom, the phase of its coherence turns with the relative frequency Δ in the light frequency rotating frame, and the coherence amplitude decays with a rate $\frac{\Gamma}{2}$. It is easy to demonstrate that the population of the excited states decay with rate Γ:

$$\begin{aligned}\frac{d(\hat{\beta}^+_{j,\alpha}\hat{\beta}^-_{j,\alpha})}{dt} &= \frac{d\hat{\beta}^+_{j,\alpha}}{dt}\hat{\beta}^-_{j,\alpha} + \frac{d\hat{\beta}^-_{j,\alpha}}{dt}\hat{\beta}^+_{j,\alpha} \\ &= \left(-i\Delta - \frac{\Gamma}{2}\right)\hat{\beta}^+_{j,\alpha}\hat{\beta}^-_{j,\alpha} + \left(i\Delta - \frac{\Gamma}{2}\right)\hat{\beta}^+_{j,\alpha}\hat{\beta}^-_{j,\alpha} = -\Gamma\hat{\beta}^+_{j,\alpha}\hat{\beta}^-_{j,\alpha} \ .\end{aligned} \tag{2.35}$$

Going back to including the effective coupling between the atomic dipoles in equation (2.33), so we have:

$$\frac{d\hat{\beta}^-_{j,\alpha}}{dt} = \sum_{\substack{m=1\ldots N \\ \gamma=x,y,z}} \mathrm{K}_{j,\alpha,m,\gamma}\ \hat{\beta}^-_{m,\gamma} \ , \tag{2.36}$$

the behavior of the dipoles will not anymore be independent of each other. To solve this set of 3N first-order differential equations we need to diagonalize the matrix K. This matrix is not Hermitian but it is symmetric, so we can still find a set of 3N numbers λ_n and vectors $\mathbf{v}_n$, for $n \in \{1, ..., 3N\}$, such that $\mathrm{K}\mathbf{v}_n = \lambda_n\mathbf{v}_n$. The vectors $\mathbf{v}_n$ are called the right-side eigenvectors of the matrix K, and the left-side eigenvectors are simply given by the transpose of the right-side eigenvectors $(\mathbf{v}_n)^t$.

By analogy with the independent-atom picture, we can write the eigenvalues of the matrix K as

$$\lambda_n = -\frac{\Gamma_n}{2} + i\Delta_n \quad \text{with} \quad n \in \{1, ..., 3N\} \ .$$

This eigenvalues are related to eigenmodes that will be linear combinations of the 3N operators $\sigma_{j,\alpha}$, and that we can call $\hat{v}_n$ for $n \in \{1, ..., 3N\}$. Each one of these eigenmodes

evolve on time in an independent way, since they are eigenmodes of the matrix $\mathbf{K}$, we have

$$\frac{d\hat{v}_n}{dt} = \left(i\Delta_n - \frac{\Gamma_n}{2}\right)\hat{v}_n \ , \tag{2.37}$$

which has a solution given by

$$\hat{v}_n(t) = \hat{v}_n(0)e^{\left(i\Delta_n - \frac{\Gamma_n}{2}\right)t} \ . \tag{2.38}$$

These eigenmodes are the so-called *collective modes*.

Let's imagine that we can excite one specific collective mode $\hat{v}_n$ by sending a laser beam with some spatial electric field distribution, in order to excite each atomic dipole with a definite amplitude and phase, that correspond exactly to the linear combination of atomic dipoles that configure this eigenmode. In this case, all the others eigenmodes will have an initial amplitude $\hat{v}_m = 0$ for $m \neq n$. This means that the amplitude of all atomic dipoles in the cloud will decay on time with the same rate $\frac{\Gamma_n}{2}$, different than the single-atom one ($\frac{\Gamma}{2}$). This modification of the decay rate is an intrinsic collective phenomenon. The modes that present $\Gamma_n > \Gamma$ are called *superradiant modes* while the ones with $\Gamma_n < \Gamma$ are called *subradiant modes*. At the same time, the imaginary part of the eigenvalue Δ_n represents a shift of the resonance that, in general, is different from the detuning Δ. This means that the laser will be in resonance with this specific eigenmode not anymore when $\Delta = 0$, but when $\Delta_n = 0$. The average of these shifts, considering a specific excitation, is called *collective Lamb shift*.

In general, a laser excitation of the atomic dipoles will produce different amplitudes for all eigenmodes of the atomic cloud. Then, the decay rate of the atomic excitation will not have a single rate, but several different rates Γ_n. In the same way, the atomic resonances are now inhomogeneously spread because of the different collective Lamb shifts Δ_n, which means that the collective atomic transition will present an inhomogeneous broadening, and an average shift, given by this collective Lamb shift.

2.2.4 Coherent Transmission

Going back to consider laser excitation in equation (2.31), once the laser is turned on, the atoms will begin to absorb and emit photons, and after some transient response of the cloud, the atomic dipoles will reach a steady state. In this situation, the average value of the operators do not change anymore and we can consider $\frac{d\langle\hat{\beta}^-_{j,\alpha}\rangle}{dt} = 0$. Then, we end up with a system of 3N linear equations:

$$\sum_{\substack{m=1\ldots N \\ \gamma=x,y,z}} \mathrm{K}_{j,\alpha,m,\gamma}\langle\hat{\beta}^-_{m,\gamma}\rangle = -\frac{i\Omega_{j,\alpha}}{2} \ , \tag{2.39}$$

which solution is given by

$$\langle\hat{\beta}^-_{m,\gamma}\rangle = -i \sum_{\substack{j=1\ldots N \\ \alpha=x,y,z}} \left(\mathrm{K}^{-1}\right)_{j,\alpha,m,\gamma} \frac{\Omega_{j,\alpha}}{2} \ . \tag{2.40}$$

Here $\left(\mathrm{K}^{-1}\right)_{j,\alpha,m,\gamma}$ is the matrix element of the inverse of the matrix $\mathbf{K}$.

Note that using the approximation $\hat{\beta}^{-}_{m,\gamma} \simeq \langle \hat{\beta}^{-}_{m,\gamma} \rangle$ is equivalent to treat the dipoles as classical. This rely on the assumption that in the linear regime, the quantum fluctuations of the operators can be neglected and the scattering process is classical in its essence.

We are interested in investigating the optical response of the cloud to a laser light nearly resonant with the specific transition $J = 0 \leftrightarrow J = 1$ considered in the Coupled Dipole Model. Specifically, we want to calculate the transmitted part of the total driving field, i.e. the projection of the total (incident + emitted) electric field in the mode of the incident light beam. For an point $\mathbf{r}$ in the forward direction of the laser excitation, we will have that the total field, in the linear and stationary regime, is given by (55):

$$\mathbf{E}_T(\mathbf{r}) = \mathbf{E}_l(\mathbf{r}) - i\frac{dk_0^3}{6\pi\epsilon_0} \sum_{\substack{m=1\ldots N \\ \gamma=x,y,z}} V_{j,\alpha,m,\gamma} \langle \hat{\beta}^{-}_{m,\gamma} \rangle \ . \tag{2.41}$$

Using this equation, we can access the field in the forward direction (which is dominated by its coherent part at low intensity (49)), but it is necessary to perform an integration over an area where the total field is projected into the mode of the incident laser field.

Another way to compute the coherent transmission, i.e. isolating the part of the field that preserves the polarization state and possesses a well-defined phase relationship with the incident field, is the following (56):

$$T(\Delta) = 1 + \frac{3i}{(\mathrm{w}_0 k_0)^2} \sum_{\substack{j=1\ldots N \\ \alpha=x,y,z}} \frac{E_l(\mathbf{R}_j)}{E_0} \, c_{j,\alpha}(\Delta) \ , \tag{2.42}$$

where $T(\Delta)$ is the coherent transmission coefficient, and it was calculated considering a Gaussian mode of the input laser with amplitude and waist given by E_0 and w_0 at the beams focus. Here, we have defined $c_{j,\alpha}(\Delta)$, which represents the re-scaled dipole amplitudes and, in the steady state regime, can be expressed by

$$c_{j,\alpha}(\Delta) = \frac{dk_0^3}{3\pi\varepsilon_0 E_0} \langle \hat{\beta}^{-}_{j,\alpha} \rangle \ . \tag{2.43}$$

The expression in equation (2.42) represents a useful definition of the transmission coefficient $T(\Delta)$, since avoids a numerically expensive point-by-point evaluation of the scattered field, as prescribed by the equation (2.41).

2.3 Collectiveness in an Atomic Ensemble

We saw in the previous sections that the collective modes, in the context of the CDM, are given by states in which the imaginary part gives information about the frequency shift of the resonance condition for each of these collective modes, while the real part represents the decay rate of the excited collective modes. Phenomena like subradiance and

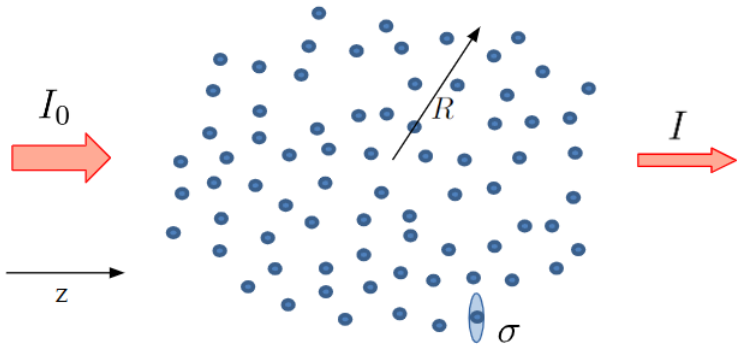

Figure 2 – Atomic ensemble of size R interacting with an incident light of intensity I_0 and having a transmitted light of intensity I, according to the absorption cross-section σ.

Source: By the author.

superradiance, or the collective Lamb shift, were experimentally verified for the dilute regime (where $\rho/k_0^3 \ll 1$).

In order to make an analysis of the collective effects in a system composed by N atoms (as the one shown in figure 2), it is convenient to introduce the parameter called *optical depth*. The optical depth b of an atomic cloud is defined by:

$$b = \sigma(\Delta) \int \rho(r) dz \ , \tag{2.44}$$

where $\sigma(\Delta)$ is the absorption cross-section

$$\sigma(\Delta) = \frac{\sigma_0}{1 + 4\frac{\Delta^2}{\Gamma^2}} \ , \tag{2.45}$$

that depends on the absorption cross-section at resonance $\sigma_0 = 3\lambda^2/2\pi$. At the end, the optical depth of the cloud at resonance will be proportional to the number of atoms, the size of the cloud and the wavenumber associated to the atomic transition as:

$$b_0 \propto \frac{N}{(k_0 R)^2} \ . \tag{2.46}$$

In the dilute regime, each atom of the cloud absorbs independently the incident light, and the total behavior is given by the Beer-Lambert law, which gives the transmitted intensity as a function of the b:

$$I = I_0 e^{-b} \ . \tag{2.47}$$

In the case of the dense regime (where $\rho/k_0^3 \gtrsim 0.1 - 1$), the effective interaction between neighbouring atoms can reach values of the order of $\hbar\Gamma$ or higher. This mean that one photon scattered by an atom saturates a close neighbourhood and the near-range terms

dominate the interaction. In this regime, the Beer-Lambert law does not apply anymore: absorption is intrinsically collective. Also, as a consequence of this strong interaction between the atoms, it is possible to observe the appearance of a big inhomogeneous broadening of the atomic resonance.

Studies about the decay dynamics of a dilute cloud shows that the initial decay rate of the excitation is proportional to b_0 (9), such that

$$\Gamma_n \propto b_0\Gamma \propto \frac{\Gamma N}{(k_0R)^2} \ . \tag{2.48}$$

Note that these initial decay rates Γ_n are related to superradiant modes which dominate the initial fast decay of the cloud excitation. Beside the superradiant decay rate, numerical simulations suggest that the whole distribution of decay rates (including also the subradiant ones) depends only on b_0 for a dilute cloud (7).

We can try to understand why the scaling parameter for subradiant and superradiant decay is b_0. In the calculations performed so far, we see that the decay of the atomic excitation is given by the coupling of the atoms and the vacuum modes of the electromagnetic field. If we consider an atomic cloud of finite size R radiating in space, we could ask how many independent modes are efficiently coupled to the sample considering the limitations produced by the boundary conditions. The electric field of the light emerging from the sphere points in all directions of the sphere and is determined by the shape of this electric field at the surface. Also, the variation of the electric field on the surface of the sphere have a minimum spatial size of the order of $\lambda = 2\pi/k_0$, which is the typical length scale of the variation of the electric field of light of frequency $\omega = ck_0$. In this way, the total number of collective modes N_m efficiently coupled to the sample is related to the sample surface divided by λ^2, i.e.

$$N_m \propto \frac{4\pi^2R^2}{\lambda^2} \propto (k_0R)^2 \ . \tag{2.49}$$

Another parallel discussion here can be the relation between the number of atoms N of the atomic sample and the number of collective modes N_m. If $N > N_m$, the emission will be cooperative since N/N_m atoms emit in the same modes; the atoms are coupled to each other via their common coupling to the electromagnetic mode. If $N_m > N$, each atom emits on average light through an independent mode, and their emissions will not be coupled. The ratio N/N_m is known as *cooperativity parameter* since determines the *collectiveness* of the atomic emission (3). Finally, using the equation (2.49), we can see that

$$\frac{N}{N_m} \propto \frac{N}{(k_0R)^2} \propto b_0 \ , \tag{2.50}$$

so the collective aspects of the atomic emission depend indeed on b_0, and these collectiveness begin to happen for $b_0 \gtrsim 1$.

The discussion made above, about the dependence of the collectiveness with b_0, is consistent with the ones made on the papers (10) and (57), in which it is studied the Dicke superradiance i.e. the superradiance when the atoms are enclosed in a volume much smaller than λ^3, so $R \ll \lambda$.

Studies of the collective Lamb shift of an atomic cloud with a dipolar transition, shows a dependence of this shift with the atomic cloud parameters (58); for the dilute regime:

$$\langle \Delta_n \rangle = -\frac{\xi \Gamma \rho}{k_0^3} \ , \tag{2.51}$$

where ξ is a numerical factor that depends on the geometry of the cloud: shape, size and atomic distribution. As the density ρ of the cloud is proportional to N/R^3, with R the size of the cloud, we will have that $\langle \Delta_n \rangle \propto \Gamma N/(k_0 R)^3$. This shift can be understood as an average value of the dipole-dipole interaction between the dipoles of the dilute cloud.

The spatial density of a cloud in the dilute regime is limited, but the optical depth can have any positive value, since the cloud just need to be large to access high values of b_0. As a consequence of this, even when collective Lamb shift is such that $|\langle \Delta_n \rangle| = |\xi \Gamma \rho / k_0^3| \ll \Gamma$, the superradiant decay rate Γ_n can be several times Γ for a low density cloud. For high density clouds, the collective Lamb shift can be bigger than Γ and none of the dependencies deduced here are valid; in particular, the superradiance and subradiance decay rates will not anymore respect the universal simple scaling with b_0. Also, for the coherent transmission spectra, a simple picture of broadening plus shift of the line is not enough to understand the behaviour of the experimental curves.

As the dense regime situation is so mysterious and unknown, we will tackle this specific case along this work. Specifically, we want to understand the behavior of the coherent transmission spectra.

3 ULTRA-COLD CLOUD OF STRONTIUM

In this chapter, we are going to be made a description of the experimental setup in order to explain how we obtain an ultracold atomic cloud from a hot gas of strontium, suited for probing light-matter interaction phenomena.

3.1 ^{88}Sr Structure

Strontium (Sr) is the chemical element that we use in our lab in order to obtain an ensemble of atoms and produce light-matter interaction studies. Its atomic number is 38 and, as an alkaline-earth element, it has two valence electrons. The electron configuration is given by

$$1s^2 2s^2 2p^6 3s^2 3p^6 3d^{10} 4s^2 4p^6 5s^2 \ .$$

This last characteristic allows the existence of two different kinds of energy levels: singlet, with the total electron spin $S = 0$, and triplet, with the total electron spin $S = 1$.

Strontium possess four stable isotopes: ^{84}Sr, ^{86}Sr, ^{88}Sr (that are bosonic species) and ^{87}Sr (that is a fermionic specie). In our experiment, we use specifically the isotope ^{88}Sr which is the most abundant with 82.58% of all natural strontium (59). A simplified

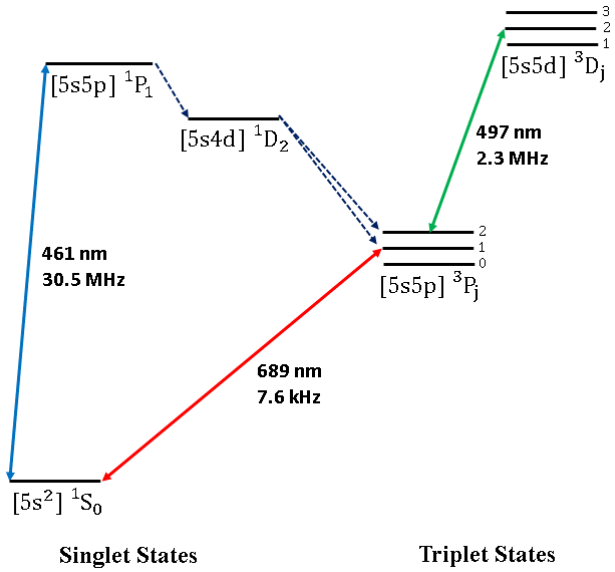

Figure 3 – Simplified Strontium Level Scheme. The blue, red and green lines represent the three atomic transitions that are relevant for our experiment.

Source: By the author.

diagram of energy is shown in figure 3, and here we can only see the atomic levels that are relevant for the description of our experiment.

The nuclear spin of all bosonic alkaline-earth elements is zero. This characteristic prevents the appearance of a hyperfine structure and is also responsible for a non-degenerate ground state, i.e. a ground state with a total angular momentum $J = 0$. As mentioned in the introduction of this document, the property of having a non-degenerate ground state makes the ^{88}Sr privileged for the study of light scattering in the dense regime. Also the ^{88}Sr has two dipolar transitions $J = 0 \leftrightarrow J = 1$ (that are accessible by the available commercial laser sources), which was the kind of transition considered in the calculations of the Coupled Dipole Model developed in the previous chapter.

Another important characteristic is the existence of metastable states, and atomic transitions with large and narrow linewidths. Large transitions allow to trap a large number of atoms in an atomic ensemble; narrow transitions allow to obtain a low temperature atomic cloud. In our experiment, we use both large and narrow transitions to trap and cool the ^{88}Sr atoms.

The colored lines in figure 3 represent the atomic transitions that we use to cool the atom system. There is a blue transition (461 nm) $^1S_0 \Leftrightarrow {}^1P_1$ with a wide linewidth of $\Gamma = 30.5$ MHz, a red transition (689 nm) $^1S_0 \Leftrightarrow {}^3P_1$ with a narrow linewidth of $\Gamma = 7.6$ kHz, and a green one (497 nm) $^3P_2 \Leftrightarrow {}^3D_2$ used to optically repump atoms. The whole process of cooling and trapping atoms is going to be explained later in this chapter.

Note that the red transition is a spin-forbidden transition, since does not obey the $\Delta S = 0$ dipole selection rule. However, the spin-orbit interactions induce mixing of states with the same total angular momentum J and different spin S. Then, the mix of some $^1P_1$ state contribution into the $^3P_1$ state, allows the transition $^1S_0 \Leftrightarrow {}^3P_1$ (with $\Delta S = 1$) to support dipole transitions (60).

3.2 Lasers and Frequency Stabilization

There are three lasers in our optical table that participate in the cooling process: blue (460 nm), green (497 nm) and red (689 nm). They are used to obtain two Magneto Optical Traps (Section 3.4). In the following sections we are going to give some details about the laser systems and the techniques that we use to stabilize the frequencies of these lasers. Frequency stabilization allows to correct any shift of the laser frequency, which is very important for atomic physics experiments.

3.2.1 Blue and Green Lasers

Both blue and green lasers used in our lab are frequency-doubled diode lasers bought from Toptica Photonics. The internal configuration for these kind of laser is shown

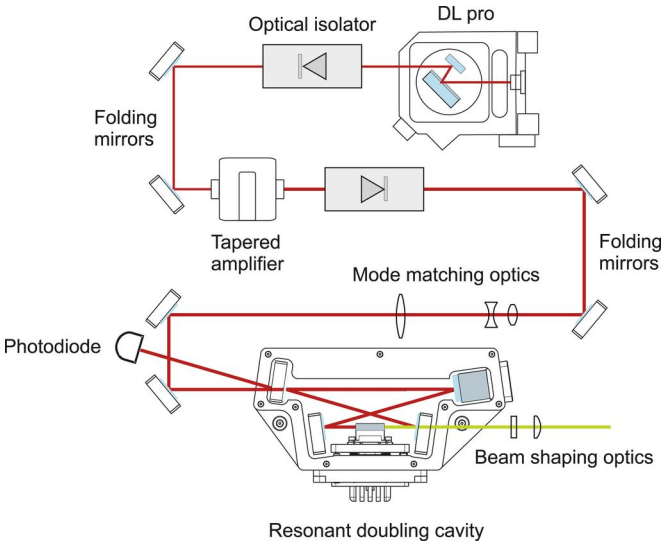

Figure 4 – Scheme of the internal configurations for a frequency-doubled diode laser.The only difference in the configurations of the Blue and the Green lasers is the absence of a Tapered Amplifier for the Green laser.

Source: Adapted from TOPTICA (61).

in figure 4. We can see that there is an infrared initial radiation, produced by a diode laser, entering in a bow-tie cavity with a crystal inside which doubles the frequency through a non-linear effect with a high χ_2 (second order of atomic susceptibility). In other words, these lasers contain a Second Harmonic Generator (SHG) to produce the light with the proper linewidth that we need in our experiment. The blue laser has also a Tapered Amplifier (TA) after the infrared radiation and, at the end, it has a total power of 700 mW at $\lambda_b = 460$ nm. The green laser does not have a TA and the total power is 55 mW at $\lambda_g = 497$ nm. Figure 5 shows a simplified scheme of the blue and green systems, after the output of the respective lasers.

BLUE LASER STABILIZATION

To stabilize the frequency of the blue laser, we use the *saturated absorption spectroscopy technique* (also known as *Doppler-free spectroscopy* (62)). For this purpose, two blue beams are used: a pump beam with high intensity and a probe beam with low intensity. Both beams, having the same frequency, are aligned to a cell containing strontium ("Sr cell" in fig. 5) at a temperature of around 350°C. The cell is wrapped in turn with glass wool and aluminum foil, in order to thermally isolate it from the environment. When both beams are simultaneously resonant near the blue transition for the same velocity class of atoms, the pump beam saturates the transition producing a dip in the absorption spectrum of the probe beam. This signal is used as a frequency reference and it is introduced in a commercial Lock-in circuit from Toptica, which generates a feedback that stabilize the

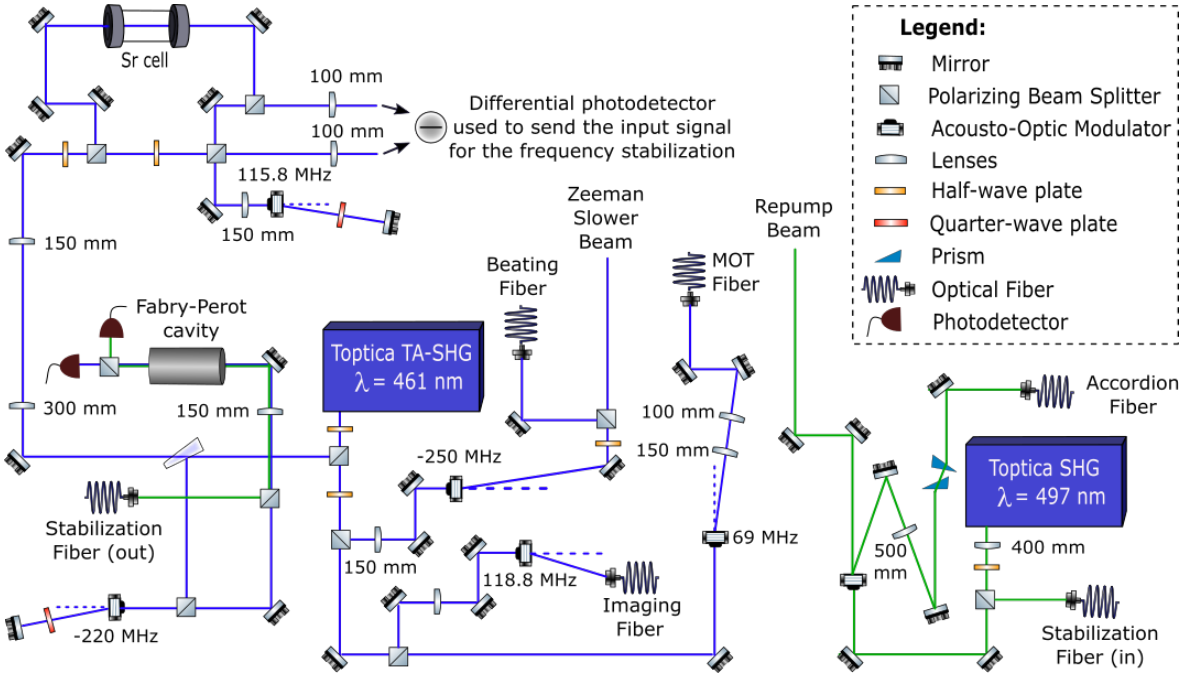

Figure 5 – Simplified scheme of the optical table for the blue and green lasers. We see how the light is distributed on the optical table, passing through lot of optical devices. The frequencies of the Acousto-Optic Modulators and the focal length of the lenses are shown in the figure.

Source: By the author.

laser on this frequency. At the end, we have an stability of the order of 1 MHz, which is good enough when compare with the linewidth of the blue transition (30.5 MHz).

GREEN LASER STABILIZATION

As the green transition does not start from the ground state (see fig. 3), it is not possible to apply the conventional Doppler-free spectroscopy to stabilize the green laser. This could be possible populating the metastable state $^3P_2$, but for that, we would need to use a Hollow-cathode lamp (63). Another way to stabilize the frequency of the green laser can be using a stable cavity. We do not have in our experiment a stable cavity that operates for the green wavelength, but following this idea, we implemented a regular Fabry-Perot cavity which length is previously locked using the blue laser as a frequency reference and then, we lock the green laser on the cavity.

The Fabry-Perot cavity used for the green laser stabilization has a free spectral range of $\Delta_{FSR} = \frac{c}{2L} = 3$ GHz, where L is the length of the cavity. This estimation of the free spectral range is only valid for the blue light, since we know that the mirrors of the cavity have the maximum reflectivity for the blue wavelength. For the green light, this value will be a little different. By some characterizations of the cavity, we measured a

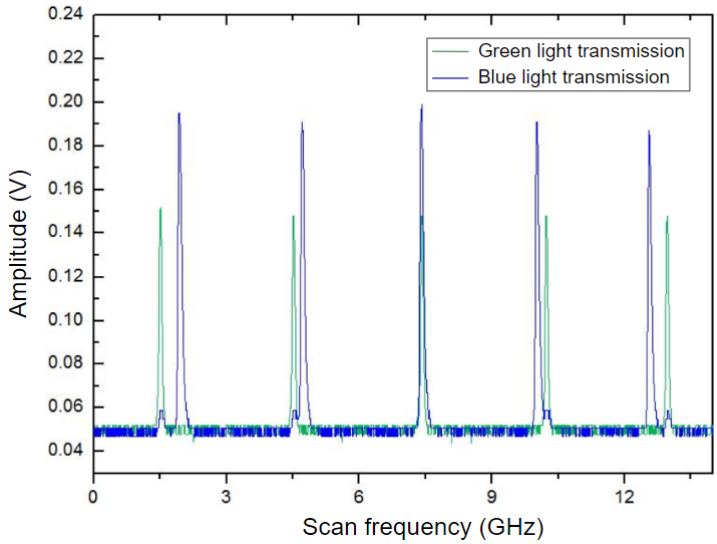

Figure 6 – Blue and green lights transmission peaks while scanning the length of the Fabry-Perot cavity.

Source: By the author.

finesse of $\mathcal{F}_b = 110$ for the blue wavelength and $\mathcal{F}_g = 50$ for the green one. Then, the width of the transmission peak for the green light is going to be $\Delta\upsilon = \frac{\Delta_{FSR}}{\mathcal{F}_g} \simeq 60$ MHz and we could lock the laser in a fraction of this value.

In order to transfer the stability from the blue laser to the green laser, we need both lasers simultaneously in resonance with the cavity. As the frequencies of these resonances are for $f_n = n\Delta_{FSR} = \frac{nc}{2L}$ with $n \in \mathbb{N}$ and the derivative of this expression is $df_n = -\frac{nc}{2L^2}dL$, we have that the minimal difference between a blue and a green resonance, when the cavity length is scanned by one blue free spectral range, is given by:

$$\Delta f = \Delta_{FSR}\frac{|\lambda_g - \lambda_b|}{\lambda_b} \approx 234 \text{ MHz} .$$

Then, considering the fraction of this value when compare with the free spectral range, scanning the length of the cavity by approximately $13 \times \Delta_{FSR}$ would be enough to find coincident resonances. A fine tuning of the blue resonance can be done by touching the Acousto-Optic Modulator (AOM) that is located before the blue light entering the cavity.

Note that here we used the relation $2L = n\lambda$ for the resonance condition, which is equivalent to saying that the length of the cavity must be equal to a multiple of the wavelength for the light to be in constructive interference with itself after a round trip inside the cavity.

In figure 6, there is an experimental observation of the transmission peaks for the blue and green beams that enter to the cavity while scanning the length of this cavity. We can see that we have a condition where both beams are simultaneously resonant

with the cavity and we select this specific peak for the system stabilization. To lock the length of the Fabry-Perot cavity, we used a homemade lock-in circuit and a Proportional–Integral–Derivative (PID) controller, that were built with this specific purpose.

ABSORPTION IMAGING TECHNIQUE

Continuing with the description of the system shown in fig. 5, we see that one of the beams of the blue laser is coupled into a fiber called "Imaging Fiber". This beam is used to characterize our atomic cloud by the Absorption Imaging technique. For the imaging, we send a resonant probe beam to the cloud (whose diameter is much larger than the size of the cloud) in order to record, by a CCD camera, the shadow produced by the atoms absorption. These images are taken after turning off the trap, letting the atoms fall by the effect of gravity. This time is known as *time-of-flight* and is usually of the order of a few milliseconds. Unfortunately, this imaging technique has limitations to probe dense atomic clouds (we will be back to this discussion later in this document), but is good enough to characterize the dilute clouds that we are describing in this chapter.

Summarizing all the information above, we have that the blue laser is divided into five principal beams: the doppler-free spectroscopy beam, the Zeeman slower beam (see section 3.3), the Magneto-Optical Trap beam, the Absorption Imaging beam and finally, a beam used to stabilize another blue laser that we have in our experiment (details of this are given in chapter 6). The green laser is divided in one beam used for the frequency stabilization, the repump beam sent to the science chamber, and a final beam with the purpose to produce an optical accordion trap (explanation in chapter 6).

Note, in the green laser system, that before the light entering in the accordion fiber, it passes through a prism pair (composed by two right angle prisms) that are used to reshape the beam correcting its ellipticity. Circularizing this elliptical beam allow us to obtain a better coupling of the light in the optical fiber.

3.2.2 Red Laser

Our red laser of $\lambda_r = 689$ nm (also from Toptica Photonics), is directly produced by a laser diode in a tunable extended cavity. We then must stabilize the laser frequency to a linewidth smaller than the natural linewidth of the red transition.

RED LASER STABILIZATION

To stabilize the frequency of this laser, we use an ultra-stable Fabry-Perot cavity made of Zerodur, bought from Stable Laser Systems. This super-cavity is kept at a vacuum of 10^{-7} Torr produced by an ion pump, that isolates it thermally from the external environment and has a system of temperature stabilization through a homemade PID

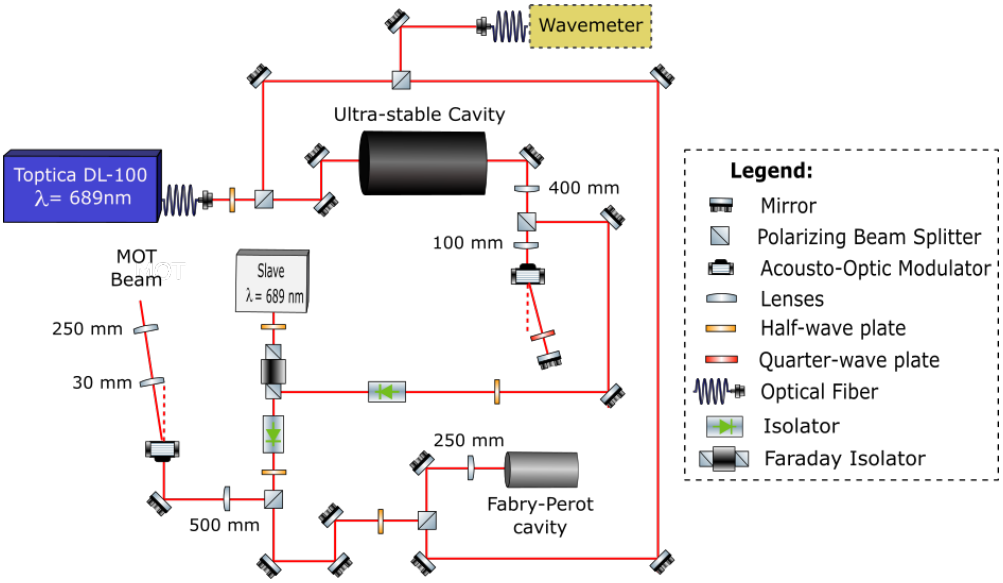

Figure 7 – Simplified scheme of the optical table for the red laser, where we can see the stabilization system and the injection locking configuration.

Source: By the author.

circuit. The cavity is used as a very stable reference since the frequency variation of its resonance is less than 5 MHz per year (corresponding to a length variation, for the 10 cm cavity, of less than 2 nm). In addition, this cavity has a high finesse of $\mathcal{F} = 6000$, which for a Free Spectral Range of $\Delta_{FSR} = 1.5$ GHz results in a transmission width of 75 kHz. The stabilization system for this laser is based on the Pound-Drever-Hall (PDH) technique that allows actively tuning the laser to match the resonance condition of the stable reference cavity. This technique can also decrease the linewidth of the laser if the optical cavity is more stable than the laser source.

In order to estimate the linewidth of the laser after the stabilization, it was made a beating between a laser beam of our red system and another red beam from a second experiment of Strontium, which is in a room next to ours. The red laser of this second experiment is also stabilized using a ultra-stable cavity with finesse of $\mathcal{F} = 20000$. The beating signal was recorded by a spectrum analizer with 10 Hz of resolution bandwidth. In these conditions, since the two lasers are uncorrelated, the width of the resulting beat signal is a convolution of the linewidths of the two light sources and the bandwidth of the spectrum analizer (64). The details of this measurement can be found in a master thesis of our research group (65) and the measured width for the beating signal was 0.9 kHz, indicating an upper bound for our laser linewidth. This linewidth of our red laser is good enough to operate with a narrow transition of natural linewidth equal to 7.6 kHz.

INJECTION LOCKING

The red laser has 12 mW of output power, and this is not enough power for the demands of the experiment. In order to increase the power of the red laser, we use a beam as a seed for another diode laser in a Master-Slave configuration. This technique is called Injection Locking (66), in which the slave laser synchronizes in phase with the master resulting in the same spectral characteristics (central frequency and also width) for both lasers. This synchronization allows to amplify the available power at the desired frequency, without affecting the spectral characteristics obtained with the frequency stabilization system.

Figure 7 shows the optical table configuration for the red laser, that includes the stabilization part and the injection locking system. We can also see here the use of a wavemeter to monitor the wavelength of the master laser and a Fabry-Perot cavity used to monitor the injection.

3.3 Vacuum System

In traditional cold atoms experiments, it is essential the control of vacuum since the lifetime of an atomic ensemble is often limited by the presence of residual background gases in the chamber. This is because the lifetime is inversely proportional to the pressure (67).

The vacuum system in our experiment is separated in two sections by a gate valve: the oven and the science chamber, as shown in figure 8. Both parts are constantly pumped by ionic pumps that are responsible to maintain pressures of 2.1×10^{-8} Torr in the oven section and 6.0×10^{-10} Torr in the science chamber section. Differential pumping stages are required to provide a high pressure difference between the two sections. The gate valve used to separate the two sections allows filling or exchanging the oven without affecting the ultra-high vacuum of the science chamber.

OVEN SECTION

In the first section, an oven contains metallic strontium and is heated until 550°C producing an atomic vapor. This oven is thermally insulated from the environment to minimize heat losses and maintaining the high temperature. The measurement of the temperature is made with thermocouples installed outside the oven. At the output of the oven, the atoms pass through a two-dimensional array of microtubes, that allows the production of a collimated atomic beam. The microtubes are arranged in a 4 mm diameter circle, and each microtube has an internal diameter of 130 μm, an external diameter of 300 μm, and a length of 8 mm. Another important information is that the microtubes are

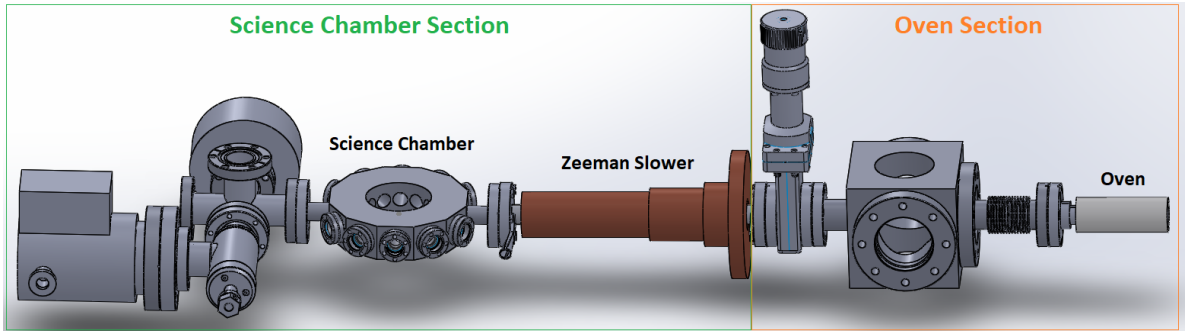

Figure 8 – Vacuum System. In the first section (right side) we have an oven that creates a collimated atomic beam which passes through a Zeeman Slower (left side) and arrives to the science chamber.

Source: By the author.

under a temperature of 600°C (even higher than the oven temperature), in order to avoid clogging by the strontium atoms.

The article (68), shows a characterization of the collimation of our atomic beam, and the measured value for the beam divergence was approximately 10 degrees. In that work, they directly measure (by a CCD camera) the fluorescence of a laser beam interacting with the atomic beam and then, they apply a model that relates this quantity with the collimation of the atomic beam, the temperature of the oven and the laser frequency.

After passing through the microtubes, the atomic beam travels down the main axis of the vacuum chamber with a flux of 10^{14} atoms per second and an average velocity of approximately 400 m/s (69). The entire oven section is mounted on a system with four degrees of freedom (transverse position and angles) so the atomic beam can be directed precisely to the center of the science chamber.

SCIENCE CHAMBER SECTION

In the second section, there is the Zeeman slower and the ultra-high vacuum chamber where the experiments take place. The Zeeman slower is responsible for decelerating the atomic beam with radiation pressure force. This force is exerted by a blue laser beam, detuned 370 MHz bellow the resonance of the ${}^1S_0 \Leftrightarrow {}^1P_1$ atomic transition, in the opposite direction to its propagation. In addition to the laser beam, it is used a magnetic field which varies over space in order to keep the laser resonant with the atoms, compensating the Doppler shift with the shift created by the Zeeman effect. The Zeeman slower is about 280 mm long with an inner diameter that changes gradually from 12 mm to 4 mm, acting as another differential pumping stage. Typically, the atoms reach velocities that are an order of magnitude smaller than the inicial velocity after passing through the Zeeman slower. The final part of the Zeeman slower is connected to the science chamber with good

optical access allowing the atoms to be trapped in its geometric center. This chamber has a two vertical entrance and 12 lateral viewports with anti-reflection coating.

3.4 Magneto Optical Trap (MOT)

When light interacts with an atom, besides changing the internal energy levels of the atom, it can also displace its center of mass because of the radiation pressure force. Depending on the way that the interaction is mediated, this force can have a decelerating character, so it can be used to cool atoms.

COOLING PROCESS

In 1975 Hänsch and Schawlow proposed the *optical molasses technique* (70) which consists in a configuration of two counter-propagating lasers red-detuned with respect to an atomic transition (i.e. $\Delta < 0$). At first, it may seem that this symmetrical arrangement has no effect on an atom, but this in only true for stationary atoms. The asymmetry in the absorption of photons by the atom from each of the lasers comes from the Doppler effect, which occurs when the atom is in motion.

In figure 9**a** we consider the case of one-dimensional optical molasses, where a pair of counter-propagating beams, that have the same frequency ω, are interacting with an atom of two levels: $|0\rangle$ ground state and $|1\rangle$ excited state. Considering what happens in the reference frame of the atom moving to the right, we see that the Doppler effect leads to a variation of the frequency of the beams so the two beams have different effects on the atom with velocity ν. Thus, the beam propagating in the same direction as the atom interacts with it with a frequency equal to $\omega - k\nu$ and the beam propagating in the opposite direction interacts with the atom with a frequency equal to $\omega + k\nu$, where k is the magnitude of the wave vector of light. As $\omega + k\nu$ is closer to the transition frequency $|0\rangle \leftrightarrow |1\rangle$, while $\omega - k\nu$ moves away from resonance, the photons of the beam propagating to the left are more likely to be absorbed by the atom than the photons of the beam propagating to the right. In this way, the force exerted on the atom by the laser that propagates in the opposite direction to its movement is greater than the force exerted by the beam that propagates in the same direction. This force exerted by the light results in the reduction of the atoms speed and, after a while, the atoms cool down until the two counter-propagating beams are at the same frequency in the frame of the atoms. In this situation, when the role of the Doppler effect decreases, the resulting force acting on the atomic system tends to zero.

Atoms in a gas move in all directions so, for the laser cooling process, is required to apply the one-dimensional scheme shown in figure 9**a** in the three spatial directions.

The beam configuration used in optical molasses reduces only the atoms speed but does not trap them. So, for the trapping process is needed a potential with a restoring

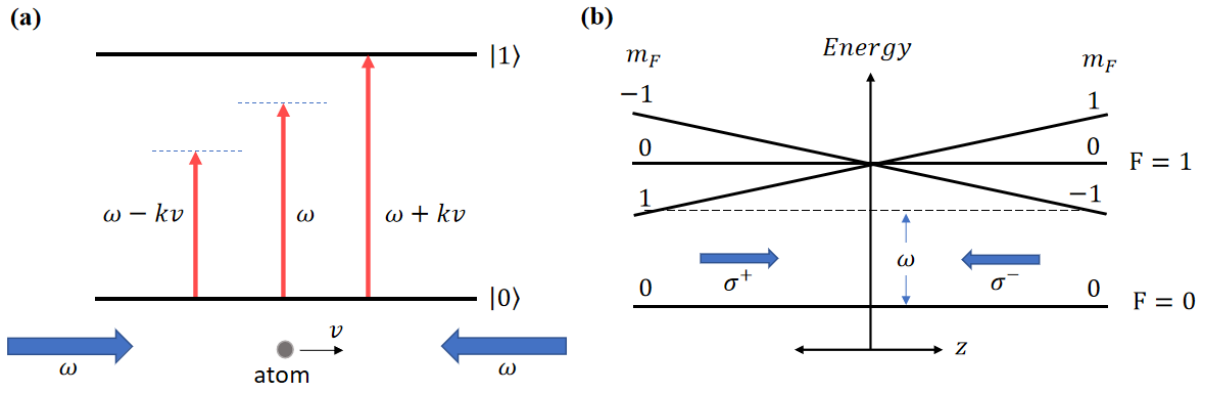

Figure 9 – Cooling and trapping processes. (a) The atom interact with two counter-propagating beams and the variation of the frequencies, produced by the Doppler effect, creates a force that reduces its velocity. (b) The combined effect of beams polarizations and a magnetic field gradient creates a force oriented to the center of the trap.

Source: By the author.

force that keeps all the atoms in the same position.

TRAPPING PROCESS

With circular and opposite polarizations for the pair of beams used for the optical molasses, this configuration can be turned into a trap by adding a magnetic field gradient that displaces atomic levels proportionally to the distance from a certain point in space, the center of the trap. This field can be produced by two coils with currents in opposite directions (anti-Helmholtz coils) that produce a quadrupolar magnetic field in the region between them.

The principle of operation of the trap, considering a simple transition from $F = 0$ to $F = 1$, is shown in figure 9**b**. In the center of the coils, the magnetic fields produced by them is zero. Around the null field there is a uniform gradient that disturbs the energy levels of the atom. The Zeeman effect produces a degeneracy of the level $F = 1$ into three sub-levels $m_F = 0, \pm 1$ and the energy shift vary linearly with the position of the atom on the z axis. As the lasers are red-detuned from the atomic resonance, for an atom in the position $z > 0$, the transition $\Delta m_F = -1$ approaches resonance with the laser frequency, while the transition $\Delta m_F = +1$ departs from resonance. This leads to a greater absorption of photons from beam with polarization $\sigma-$ in relation to the beam with polarization $\sigma+$, which produces a force that pushes the atom back into the center of the trap. One similar process occurs for an atom in the position $z < 0$; in this case, the Zeeman displacement and the selection rules favor greater absorption of the beam with polarization $\sigma+$ (which excites the transition $\Delta m_F = +1$), giving place to a force that takes the atom back to

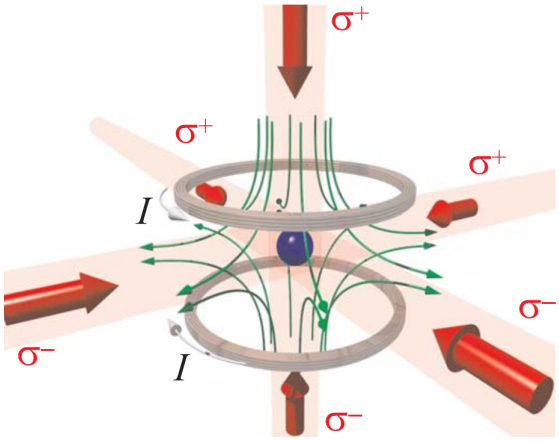

Figure 10 – Configuration of a Magneto Optical Trap with the three pairs of counter-propagating beams and the magnetic field created by the two anti-Helmholtz coils.

Source: Adapted from COURTEILLE (71).

$z = 0$.

A trap that operates in three dimensions requires three pairs of counter-propagating beams and a magnetic field gradient obtained by a pair of coils in the anti-Helmholtz configuration. This system of cooling and trapping atoms, illustrated in figure 10, is called Magneto-Optical Trap (MOT). In the next two sections will be explained how we obtain a MOT using the blue transition (blue MOT) of ^{88}Sr first and then another MOT using the red transition (red MOT). The red MOT is created from a narrow transition, so it is possible to produce a cold atom cloud with very low temperatures. On the other hand, because of the small velocity capture range of this MOT (since the maximum force is proportional to Γ), we need first to trap the atoms using the wide blue transition.

3.4.1 Blue MOT

In the first stage of cooling, after the atoms enter the science chamber, it is used the transition $^1S_0 \Leftrightarrow {}^1P_1$ to create a MOT formed by three pairs of retro-reflected blue beams with a waist of 5.6 mm and a power of Power(x,y,z)=(5.1mW, 4.8mW, 8.3mW). Then, the total intensity of the six beams at the center is equal to $1.8\mathrm{I}_{\mathrm{sat,blue}}$, where $\mathrm{I}_{\mathrm{sat,blue}} = 40.6\ \mathrm{mW/cm^2}$ is the saturation intensity of the atomic transition. The beams are around -1.25Γ detuned from the resonance, being $\Gamma_b = 30.5$ MHz the linewidth of the atomic transition. The laser detuning was chosen as the one that maximizes the optical density of the atomic cloud. The anti-Helmholtz coils used for this MOT creates a magnetic field gradient of 55 G/cm. All these parameters for the blue MOT are summarized in (72).

In the first part (blue part) of figure 12, we can find the experimental ramps for the blue MOT sequence. We can see that there is an initial capture of the atoms loading

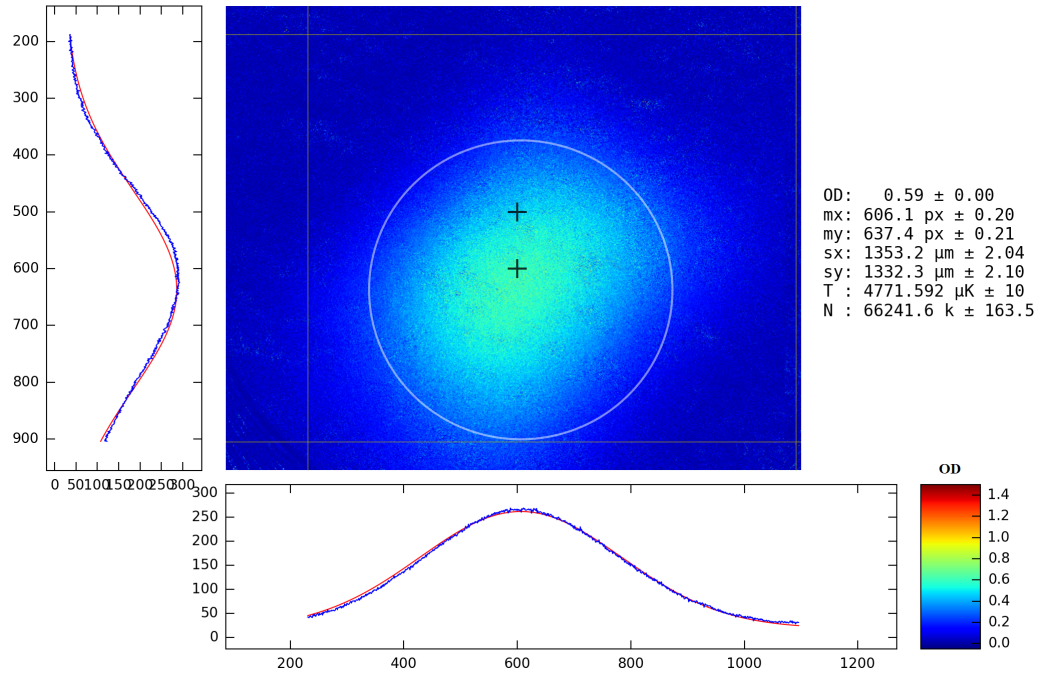

Figure 11 – Absorption Imaging for the blue MOT with a time-of-flight of 1 ms. The parameters of the cloud were obtained from a Gaussian fit of the atomic distribution.

Source: By the author.

the blue MOT for 1.5 s. Then, in order to reduce even more the temperature of the cloud, it is applied a power ramp in the trapping beams for 4 ms decreasing the power until less than 10% of its initial value. In that way, we should obtain a cloud of cold atoms with temperatures close to the Doppler limit of the blue transition, which is $T_D = \frac{\hbar\Gamma}{2k_B} = 720$ µK (73). In our experiment, we obtain a blue MOT of approximately 65×10^6 atoms with a temperature of 4 mK, as can be seen in the absorption imaging shown in figure 11. The difference of temperature with respect to the theoretical value, is probably related to a bad alignment of the MOT beams or imperfection on the profile intensity of this beams (65). The same problem was also reported in another experiments (74).

The transition used for the blue MOT is dipolar and it is not completely closed. From $^1P_1$ level there is a decay to the $^1D_2$ level with a probability of 1 : 50000. Atoms from this last level can also decay to the states $^3P_{1,2}$. Despite the low probability of transition, this mechanism is relevant due to the high rate of natural decay of the blue transition. From the $^3P_1$ state, with a lifetime of 21 µs, atoms will return to the ground state $^1S_0$.

The $^3P_2$ level is metastable (with a lifetime of about 500 s (59)), so the atoms in this level represent a loss for the MOT cycle since the blue laser can not interact with them. To solve this problem we use a green laser resonant with the transition $^3P_2 \Leftrightarrow {}^3D_2$. As this transition is also open, the atoms can decay to the states $^3P_{1,2}$ and from the level

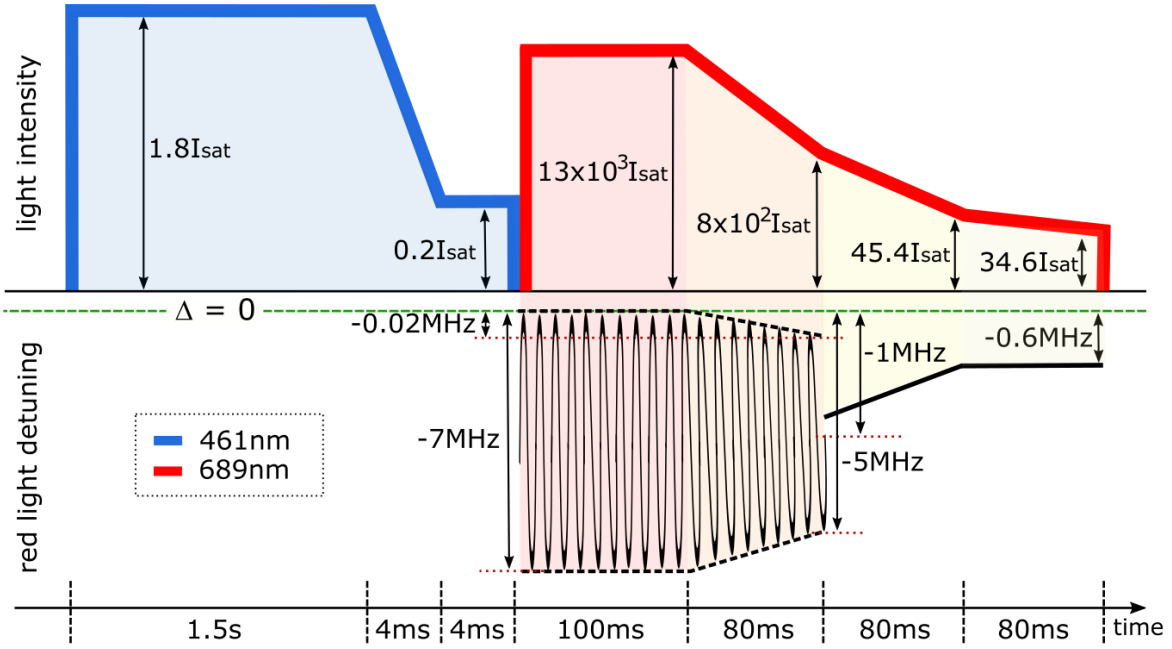

Figure 12 – Experimental ramps for both blue an red MOTs. This figure is divided in an upper and a lower part, separated by a horizontal black solid line; the upper part represents the power ramps, while the lower part represents the frequency ramps for the red light. The green dash line represents the detuning zero of the light with respect to the red transition.

Source: By the author.

$^3P_1$ they can go to the ground state $^1S_0$ where they can interact again with the blue laser. This kind of beams are usually called repump beam since they bring the atoms back to the MOT cycle.

3.4.2 Red MOT

The presence of narrow lines in ^{88}Sr offers the opportunity to add a second cooling stage in order to reduce the temperature and increase the density of the cloud. This second cooling stage consists in a red MOT, which is created using the transition $^1S_0 \Leftrightarrow {}^3P_1$ with a linewidth equal to $\Gamma_r = 7.6$ kHz.

After turning off the blue MOT beams, the red MOT beams are immediately turned on. The magnetic field is also switched from 55 G/cm to 6.5 G/cm with a small delay of 30 µs. Following the idea described by Simon Stellmer in his PhD thesis (59), we perform four frequency and power ramps of the red MOT beams during the cooling process. The details can be seen in the second part (red part) of figure 12 and the corresponding explanation is the following:

- The first ramp has a duration time of 100 ms and the total intensity of the six beams

at the center is kept in $13 \times 10^3 I_{sat,red}$. The detuning is scanned from a minimum value of -7 MHz to a maximum of 0 MHz detuning, with a frequency of 35 kHz. This technique, called Multichromatic laser cooling (75), allows to artificially broaden the narrow transition. A broadening of the transition improves the cooling efficiency, since the MOT beams can interact with a larger span of atomic velocities.

- The second ramp of 80 ms continues the multichromatic spectrum but now the minimum value of the detuning is varied from -7 MHz to -5 MHz, while the maximum has a small variation of -0.02 MHz. During this time is also performed a power ramp from $13 \times 10^3 I_{sat,red}$ to $8 \times 10^3 I_{sat,red}$.

- In the third ramp, with duration time of 80 ms, the light spectrum is reduced to a single frequency one, and the detuning is shifted closer to resonance from -1 MHz to -0.6 MHz, while the power is dramatically reduced to $45.4 I_{sat,red}$. The decreasing of the detuning provides compression of the atomic cloud, while the decreasing of the beams intensity provides cooling.

- In the fourth ramp, of 80 ms, the frequency keeps constant at the final value of the third ramp while the power is slightly changed from $45.4 I_{sat,red}$ to $34.6 I_{sat,red}$. The selection of these values is based on improving the transfer of atoms from the Red MOT to an Optical Dipole Trap.

All the frequencies mentioned before represent the detuning with respect to the atomic resonance (green dash line in fig. 12). The intensities are shown in terms of $I_{sat,red} = 3.04\ \mu W/cm^2$, which is the saturation intensity of the red atomic transition. For the red transition the Doppler temperature is $T_D = 182$ nK, bellow the recoil temperature $T_R = \frac{\hbar^2 k^2}{2mk_B} = 460$ nK (73), which represents the minimal possible temperature. Clouds with temperatures bellow 1 μK are called *ultracold*.

Since the red transition is so narrow, the radiation pressure force exerted by the light is not very strong, so the atoms can be affected by gravity, making the cloud compressed in the z direction. As a consequence, the atoms of the Red MOT live in a very thin shell interacting predominantly with the upward propagating beam, i.e. the beam propagating on $+z$ direction. Then, for a low intensity of the MOT beams, some atoms are at risk of not absorbing a photon and escaping from the cloud. This situation limits the lifetime of the cloud to a few milliseconds.

After the ramps implemented to transfer the atoms from the blue MOT to the red one, we obtain a cloud of approximately 15×10^6 atoms with temperature of 2 μK. An absorption imaging of this cloud can be found in figure 13, where we had to apply a long time-of-flight in order to have a non-saturated probing of the atomic ensemble.

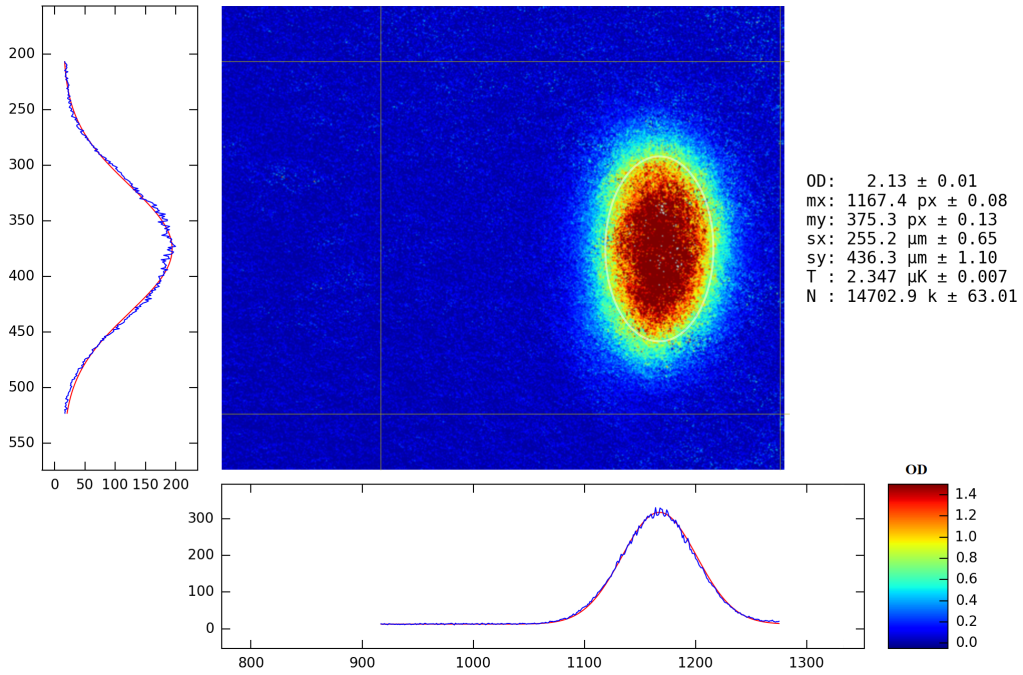

Figure 13 – Absorption Imaging for the red MOT with a time-of-flight of 24 ms. The colored scale represents the optical depth of the cloud.

Source: By the author.

4 DENSE CLOUD OF STRONTIUM

In this chapter we will continue with the description of our atomic ensemble. Specifically, it is going to be explained how we reach the atomic dense regime from the Red MOT described in the previous chapter. We will also discuss the strategies to improve our cloud and the challenges to characterize a cloud with very high optical depth.

4.1 Infrared Laser

In order to obtain a dense atomic cloud, we implemented an Optical Dipole Trap produced by an infrared laser whose frequency is very far from any atomic resonance. The infrared laser that we use in our lab is a Mephisto MOPA bought from Coherent. This laser incorporates a Mephisto laser with power up to 2W to seed cascaded amplification stages, resulting in a Master Oscillator Power Amplifier (MOPA) configuration. The seed and amplification stages are fully integrated in a single box and does not require mechanical adjustments. The output power of our laser should be 25 W with 1064 nm of wavelength, but unfortunately we have observed a decreasing of this power over the time and currently we are using less than 11 W for the whole infrared system. Some properties of these lasers

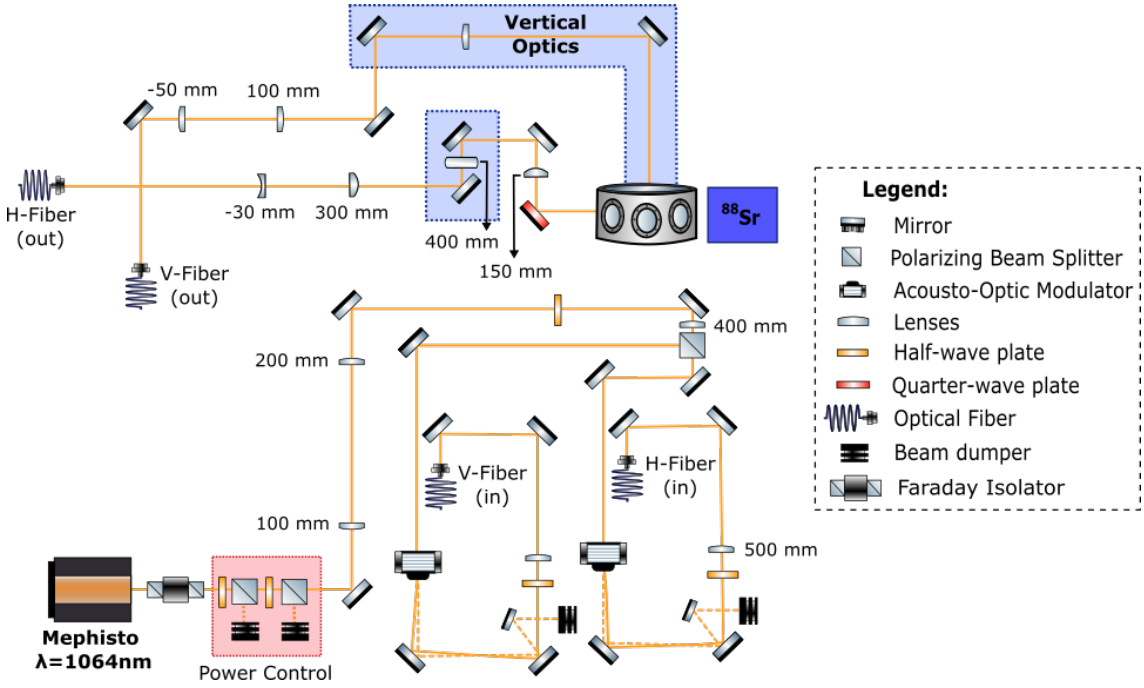

Figure 14 – Simplified scheme of the optical table for the infrared laser. The use of several beam dumpers is fundamental due to the large power of this laser.

Source: By the author.

are ultra-narrow linewidth of 1 MHz and extremely low-intensity noise. Since we use this laser in a far from resonance configuration, no stabilization technique is necessary.

The infrared laser is divided in two beams in order to create a crossed optical dipole trap, which is the combination of two optical dipole traps in the horizontal and vertical directions. This can be seen in figure 14, which shows the part of the optical table for the infrared laser. An important detail in this scheme is that the beams pass through Acousto-Optic Modulators and we chose contrary diffraction orders in the alignment just to create a frequency difference between the two beams, which is important to avoid interference effects between them.

The horizontal and vertical beams are coupled in fibers (H-Fiber and V-Fiber in fig. 14), and before entering to the science chamber, several circular and elliptical lenses are used to focus the beams at the Red MOT position with the desired geometry for each of them. More details of this system are going to be given in the next section.

4.2 Optical Dipole Trap (ODT)

Contrary to the Magneto-Optical Trap, which depends on the radiation pressure force, the Optical Dipole Trap (ODT) depends purely on the dipole force. If the laser field interacting with a two level atom system is spatially inhomogeneous, the associated energy level shift of the atoms (consequence of the Stark effect or light shift) varies in space and therefore produces a potential (73). The force from this potential is the dipole force. When the laser frequency is tuned below atomic resonance ($\Delta < 0$), the sign of the interaction is such that atoms are attracted to the maximum of laser field intensity. However if $\Delta > 0$, the attraction is to the minimum of field intensity.

The dipole force is conservative, so it is possible to assign a potential to it, called dipolar potential, given by (76)

$$V_{dip}(\mathbf{R}) = \frac{3\pi c^2}{2\omega_0^3}\,\frac{\Gamma_0}{\Delta}\,I(\mathbf{R})\ . \tag{4.1}$$

Here, $I(\mathbf{R})$ is the intensity distribution of the incident beam and, for a Gaussian elliptic beam propagating in the z direction, can be expressed by:

$$I(R,z) = I_0 \frac{\mathrm{w}_{0,x}\mathrm{w}_{0,y}}{\mathrm{w}_x(z)\mathrm{w}_y(z)} \exp\left(-\frac{2x^2}{\mathrm{w}_{0,x}^2}\frac{1}{1+(z/z_{R,x})^2}\right)\exp\left(-\frac{2y^2}{\mathrm{w}_{0,y}^2}\frac{1}{1+(z/z_{R,y})^2}\right)\ , \tag{4.2}$$

where w_i is the waist of the beam at the i axis and $z_{R,i}$ its Rayleigh range. The parameter $I_0 = \frac{2P}{\pi \mathrm{w}_{0,x}\mathrm{w}_{0,y}}$ is the maximum intensity of the beam and P its power.

On the other hand, around the ODT minimum, the potential can be expanded as a three-dimensional harmonic oscillator,

$$V_{dip} = \frac{1}{2}m\Omega_x^2 x^2 + \frac{1}{2}m\Omega_y^2 y^2 + \frac{1}{2}m\Omega_z^2 z^2 + V_0\ , \tag{4.3}$$

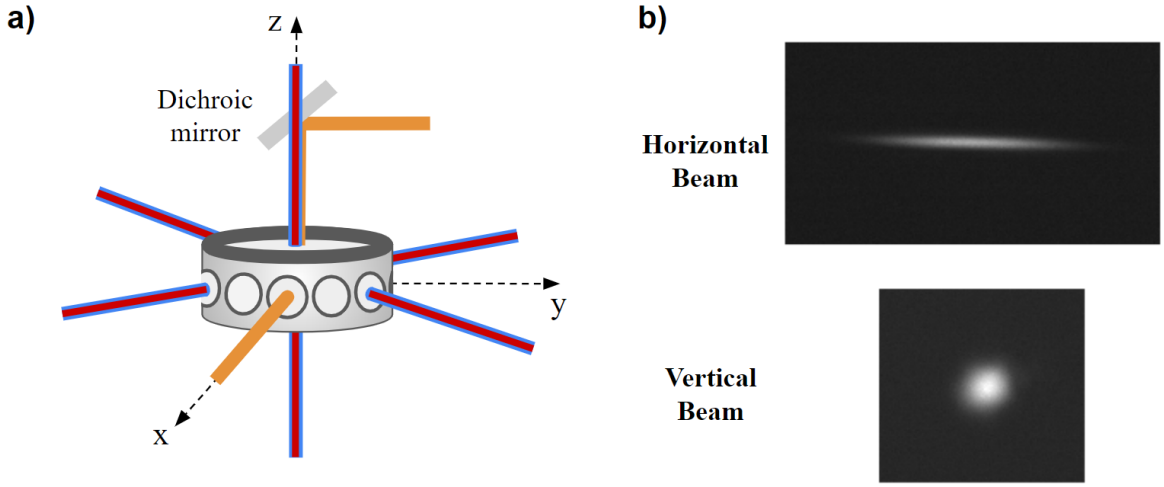

Figure 15 – a) All MOTs beams (blue and red) and both ODT beams (orange) entering to the science chamber. b) Transverse images of the horizontal and vertical beams of the ODT at the focus position.

Source: By the author.

where Ω_x, Ω_y and Ω_z represent the oscillation frequencies of the trap. For a thermalized cloud, its spatial density depends on the trap frequencies as follows:

$$\rho(x,y,z) = \rho_0 e^{-\frac{m\Omega_x^2 x^2}{2k_B T}} e^{-\frac{m\Omega_y^2 y^2}{2k_B T}} e^{-\frac{m\Omega_z^2 z^2}{2k_B T}} \ , \tag{4.4}$$

where the density at the middle of the cloud is

$$\rho_0 = \rho(0,0,0) = \Omega_x \Omega_y \Omega_z \left(\frac{m}{2\pi k_B T}\right)^{3/2} N \ . \tag{4.5}$$

Equalizing the two equations above for the dipole potential (i.e. equations (4.1) and (4.3)), we can find expressions for the oscillation frequencies as a function of the intensity, waist, Rayleigh range and detuning of the beam. However, due to the Gaussian distribution of the beam, we must make a quadratic expansion around the center of the beam, demanding the need of performing numerical calculation in order to find the frequencies.

Defining the size of the atomic Gaussian cloud as the radius at $1/\sqrt{e}$, the oscillation frequencies are also related to the size through the following expression:

$$s_i = \frac{1}{\Omega_i}\left(\frac{k_B T}{m}\right)^{1/2} \quad \text{for} \quad i \in (x,y,z) \ . \tag{4.6}$$

It is then possible to express the spatial density of equation (4.4) as a function of the size:

$$\rho(x,y,z) = \frac{N}{(2\pi)^{3/2} s_x s_y s_z} e^{-\frac{x^2}{2s_x^2}} e^{-\frac{y^2}{2s_y^2}} e^{-\frac{z^2}{2s_z^2}} \ . \tag{4.7}$$

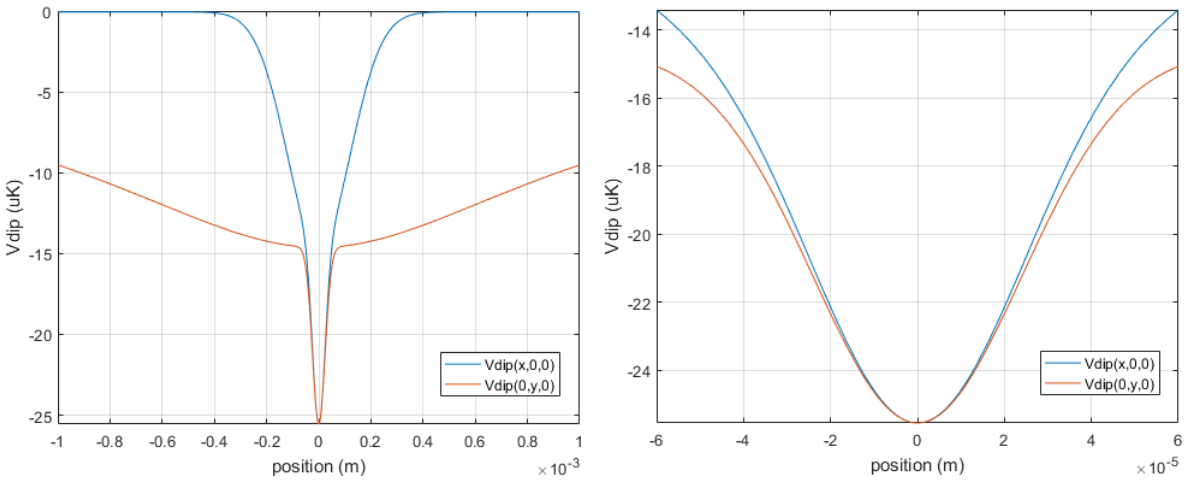

Figure 16 – Dipolar potential in the x and y directions. The graphic of the right is the same as the left one but in a different scale closer to the minimum of the potential.

Source: By the author.

The most common way of producing an ODT is with a red-detuned Gaussian beam. In our experiment, we use an infrared laser with 1064 nm, so $\Delta < 0$. Specifically, we create a crossed optical dipole trap (crossed ODT) (77) and, for this purpose, we use two beams: a Gaussian elliptic beam propagating in the horizontal direction and a Gaussian circular beam that propagates in the vertical direction. As can be seen in figure 15**a**, the ODT vertical beam combines with the MOTs vertical beams by using a shortpass dichroic mirror with a cut-off wavelength of 805 nm. Transverse images of the two infrared beams at the focus position can be found in figure 15**b** and the waists for the elliptic horizontal beam are $w_{H,x} = 240$ μm and $w_{H,y} = 17$ μm, while for the circular vertical beam is $w_{V,x} = w_{V,y} = 48$ μm.

SIMULATING THE DIPOLAR POTENTIAL CREATED BY OUR ODT

We use powers of $P_H = 1.78$ W and $P_V = 0.75$ W for the horizontal and vertical arms of ODT, respectively. Under these conditions and, considering the other parameters for the beams mentioned before, we can simulate the characteristics of the dense cloud that we should obtain in the experiment. Our crossed ODT creates a dipolar potential as the one shown in figures 16 and 17, for each spatial direction. For the potential in x and y directions, is clear the observation of a combined effect between both ODT beams. The graphic of fig. 16(right) allow us to observe the harmonic behavior of our trap at the minimum of the potential. In the graphic that represents the potential in the z direction, we can observe an asymmetry that is related to the effect of gravity. Here, we also signalized the points use to calculate the differential trap depth, which is 12 μK. This means that

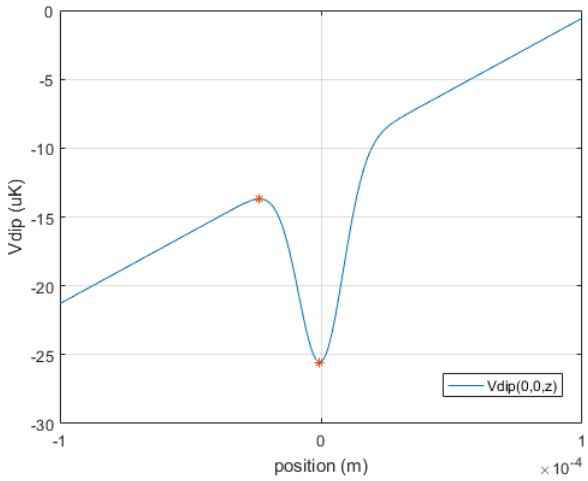

Figure 17 – Dipolar potential in the z direction. The red dots are the points used to calculate the trap depth on z.

Source: By the author.

only the atoms with a thermal energy (divided by the Boltzmann constant k_B) less than 12 μK will be trapped by the ODT.

The simulations mentioned above are well explained in the master thesis of one of the students of our lab (78). For the characteristics of the ODT beams given above, we calculated oscillation frequencies: $F(x, y, z) = \Omega/2\pi = (218,\ 213,\ 694)$ Hz. If we also consider in these simulations a number of atoms of $N = 0.5 \times 10^6$ with 1.0 μK of temperature, we should have a cloud with the following characteristics:

- Spatial density at the center of the cloud: 2.77×10^{14} atoms/cm^3.
- Spatial density at the center, in unities of $1/\lambda^3$: $\rho\lambda^3 = 27.1$.
- Sizes of the cloud at $1/\sqrt{e}$, in (x, y, z): $(7.07,\ 7.25,\ 2.23)$ μm.

An spatial density of $\rho\lambda^3 = 27.1$ represents the atomic dense regime, since $\rho\lambda^3 \gtrsim 20$; we should then observe density effects using a cloud with these characteristics. In the experimental point of view, we need to measure the parameters above for our crossed ODT in order to be sure that we reached the dense regime.

4.2.1 Experimental Cloud

In the description of the red MOT experimental ramps (section 3.4.2), we mentioned that the parameters used in the last ramp were chosen in order to increase the atomic transference from the red MOT to the ODT. This is because the ODT beams are turned on 300 ms before the end of the Red MOT sequence.

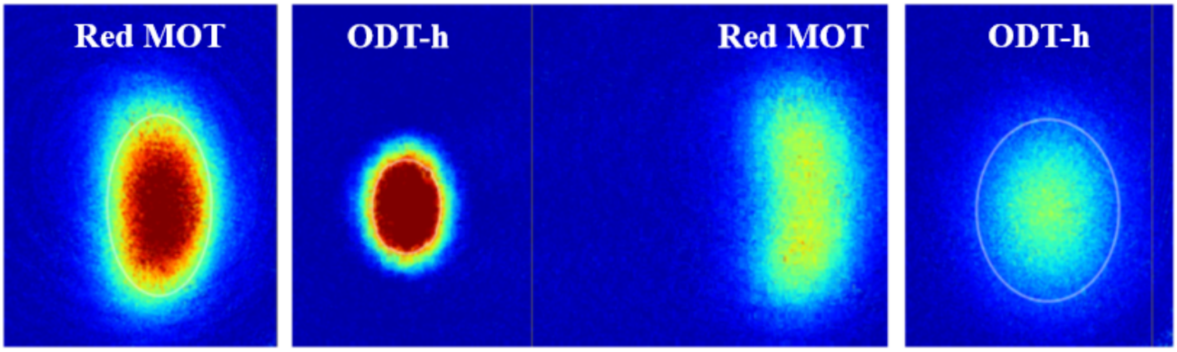

Figure 18 – Transference process from Red MOT to the horizontal ODT. On the images, gravity is oriented from left to right. This images represent: (a) only Red MOT with ToF = 25 ms, (b) both clouds for the best atomic transference condition with ToF = 10 ms, (c) only ODT-h with ToF = 25 ms.

Source: By the author.

The ODT alignment process starts by a superposition of an image of the ODT horizontal beam and the red MOT in the camera. After observing a first signal, we improve the alignment of the beam until reaching the maximum number of atoms. Figure 18**a** shows an absorption image of the initial red MOT with 13.4×10^6 atoms and 2.5 μK of temperature, measured after a time-of-flight (ToF) of 25 ms. In figure 18**b** we can see the cloud of atoms captured by the ODT horizontal beam, that we call horizontal ODT (ODT-h in the figure), and the rest of the uncaptured atoms from the red MOT. This image was taken after a ToF of 10 ms. Finally, figure 18**c** shows the horizontal ODT for a ToF = 25 ms, so we can measure the properties of this cloud. For the red MOT described before, we obtained a ODT-h cloud of 6.5×10^6 atoms (representing a 48 % of transference) and 2.2 μK. We have small fluctuations around these values day by day, but the transference from the Red MOT to the ODT-h use to be of approximately 50 %.

The images shown on figure 18 are taken from the camera with the line of sight in the horizontal x direction, this is what we call horizontal imaging. For the alignment of the ODT vertical beam, it is convenient to put the camera at the vertical axis. Figure 19**a** shows a vertical image of the ODT-h *in situ*, i.e. with ToF = 0 ms. Once we observe the influence of the ODT vertical beam on the ODT-h, we continue the alignment until observing a denser region at the center of this cloud. In figure 19**b** we can see this effect, which becomes more clear observing the Gaussian profile at the left. In these first two vertical images, we kept the ODT beams "on" for 40 ms after turning off the red MOT beams. This time (that we call holding time) of 40 ms is the minimum necessary to observe the ODT without the remaining atoms from the red MOT. If we increase the holding time, the atoms out the potential created by the superposition of horizontal and vertical beam,

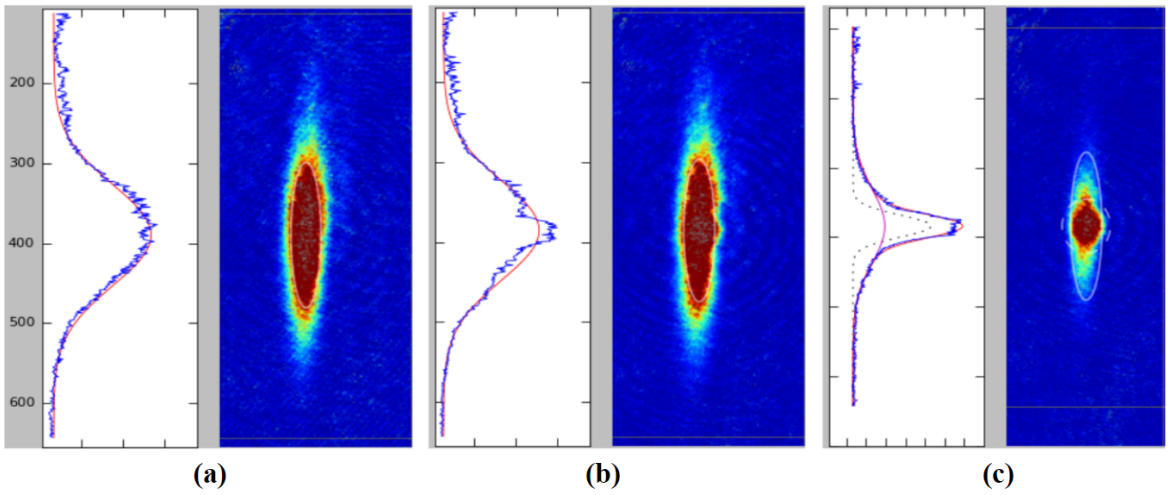

Figure 19 – Transference process from ODT-h to the crossed ODT. This images represent: (a) only the ODT-h, (b) superposition of ODT-h with the ODT vertical beam, (b) crossed ODT after a holding time of 1 s.

Source: By the author.

are going to escape from the cloud. Figure 19**c** shows our pancake shape crossed ODT cloud after 1 s of holding time. We implemented a double Gaussian fit in order to identify the behavior of the denser crossed dipole trap.

In the absorption images of figure 19, we can see a saturation of the camera. This represent a limitation on the characterization of our cloud since we cannot extract the optical depth and the sizes of the cloud by realizing a fitting of the images. To solve this problem, we found the need of implementing another observation technique called Phase Contrast Imaging used to observe dense atomic clouds *in situ*.

LIFETIME MEASUREMENT

Even with the limitations of the absorption imaging technique, if we apply a ToF of a few milliseconds, we can decrease the optical depth of the cloud allowing to measure the number of atoms of the crossed ODT by the use of the double Gaussian fit. Doing this, we can perform some characterization of the ODT such as the lifetime measurement. The result of this measurement is shown on the left graphic of figure 20, where we plotted the number of atoms for holding times varying from 300 ms to 8.5 s. Applying an exponential fitting we can extract a lifetimes of (4.03 ± 0.45)s for the crossed ODT. The obtained value is considerably short and the reason could be problems with the ODT beams alignment or with our vacuum system. Note that the fitting was done using the part of the curves after 2 s of holding time, for smaller times the quality of the double Gaussian fit is not good enough to separate the characteristics of ODT-h and crossed ODT.

In order to understand the reason of the short ODT lifetime, we also measured the

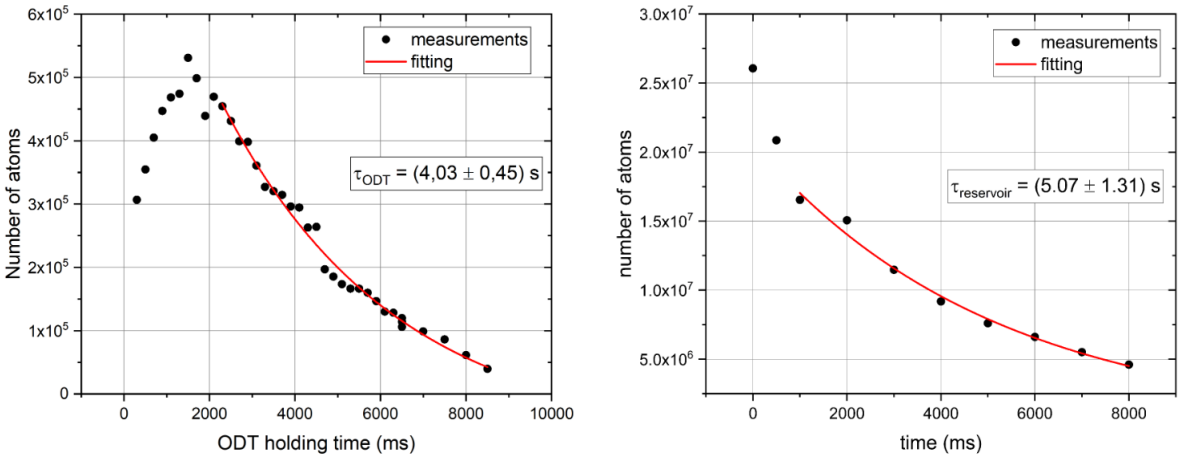

Figure 20 – Lifetime measurements for (left) the crossed ODT, and (right) the magnetic trap created by the MOT coils. The black and blue dots represent the experimental data, while the red line is the fitted exponential decay curve.

Source: By the author.

lifetime of atoms trapped in a deep magnetic trap created by the MOT coils. Since the bosonic Sr atoms have no magnetic moment in the ground state, for magnetically trapping we pump them to the $^3P_2$ metastable state, which has a lifetime of over 500 s. We obtain a lifetime of the magnetic trap of (5.07 ± 1.31)s (right graphic of figure 20). The magnetic trap has a lifetime slightly longer than the ODT but still very short, proving that the lifetime limitation is probably related to the quality of the vacuum rather than to the traps themselves. Despite that, the lifetime is certainly long enough to allow for sequential loading and performing the measurements of our interest.

OSCILLATION FREQUENCIES MEASUREMENT

To measure the oscillation frequencies we need to compress, decompress, or shift the sample for a short period of time (76). Then, when the cloud is released to the original trap it starts to oscillate. Some techniques to measure the trap frequencies are: Parametric Heating (79), Release and Recapture (80), and Breathing Mode (81). In our experiment, we applied the last two methods at the same time. For this, we made a power modulation produced by switching off (or releasing) the trap for a short time of 0.6 ms so the cloud is decompressed and its center of mass is shifted. The release and recapture method allow us to extract the frequency of oscillation by observing the variation in the position of the cloud for different waiting time between the release of the atomic cloud and the recapture moment. This technique works only for measuring the oscillation frequency in the z direction, since the atoms are pulled from its center of mass by the effect of gravity. In the other hand, the breathing mode method consist in exciting a radial oscillation mode by a compression and decompression of the trap. Experimentally, we extract the size of the

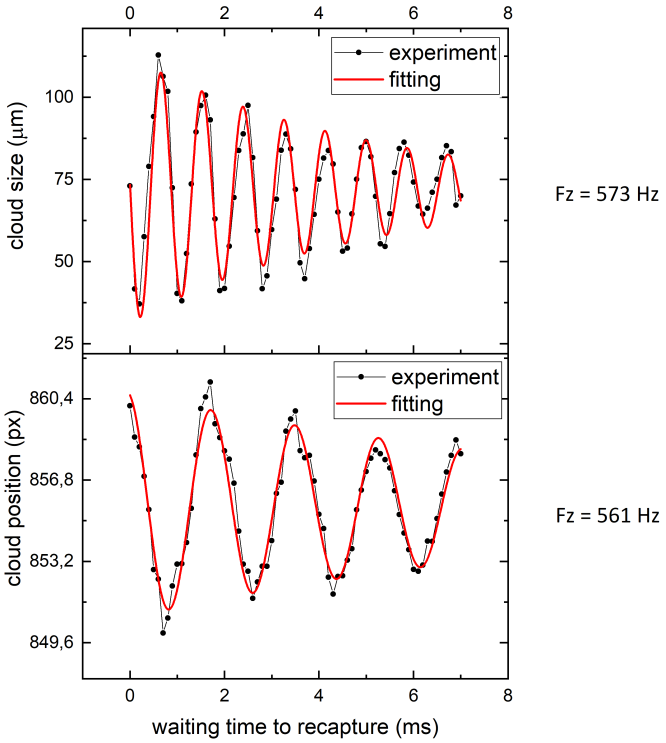

Figure 21 – Oscillation frequency measurements in the z direction by using: (top) Breathing Mode and (bottom) Release and Recapture technique. The black dots represent the experimental measurements and the red line is the damped sine function fitting. The obtained values for the frequencies can be seen in the right side of each graphic. Here, we already used the relation $F_B = 2F_z$, mentioned in the main text.

Source: By the author.

cloud for various holding times after producing the power modulation. This last technique can be used to measure the oscillation frequencies in the three spatial directions, however we just performed it for the z direction since the characteristics of the cloud in the two other axis will be extracted by using the Phase Contrast Imaging system.

When exciting a radial oscillation mode, the observed breathing mode frequency F_B is in general related to the oscillation frequency of the trap, but in a very complicated way. This relation, depends on the geometry and dimensionality of the system, if whether the potential is in the harmonic regime or not, or even on the scattering length of the atomic system (82, 83). For classical ensembles in a 3D harmonic potential, the breathing mode frequency is twice the oscillation frequency ($F_B = 2F_z$) (81).

Examples of the frequency measurement can be seen in figure 21, where we have the measurement by the breathing mode technique (top graph) and the measurement by the release and recapture technique (bottom graph). The respected measured values were extracted by fitting a damped sine function and can be seen in the figure. By doing an

average between these two results, we obtained an oscillation frequency of $F(z) \approx 567$ Hz.

The measured value of the trap frequency, turned to be different to the one expected from the theoretical calculations $F(z) = 694$ Hz. We believe that the difference is related to the fact that the power of the ODT beams considered in the simulations is higher than the actual power of the light trapping the atoms; this is because we have some power loss while the light passes through the optics or even through the science chamber windows.

4.3 Phase-Contrast Imaging

The remaining characterizations of the crossed ODT were done by the implementation of a Phase-Contrast Imaging (PCI) system. Contrary to the Absorption Imaging (AI), the PCI is a non-destructive technique that, by applying an off-resonance laser beam, allows the calculation of the accumulated phase of the light after interacting with the atomic sample (84), which is used to obtain the density profile of the atomic cloud, integrated in the propagation direction of light.

4.3.1 PCI Theory

ABSORPTION IMAGING THEORY REVIEW

For both AI and PCI techniques, we need to measure the 2D density profile $\rho_{2D}(x, y) = \int_{-\infty}^{\infty} \rho(x, y, z)$ of the atomic cloud. In the case of the AI, this is obtained through the optical depth of the sample at transverse position $b(x, y)$, since the intensity of the transmitted light, recorded by the camera, is given by

$$I_t(x, y, \Delta_{AI}) = e^{-b(x,y)}\ I_0\ . \tag{4.8}$$

Then, for an imaging beam resonant with any atomic transition that goes from the ground state to an excited state, we have the 2D density profile:

$$\rho_{2D}(x, y) = \frac{b_0(x, y)}{\sigma_0} = -\frac{1}{\sigma_0} \ln\left(\frac{I_t(x, y, \Delta_{AI} = 0)}{I_0(x, y)}\right)\ . \tag{4.9}$$

This last equation can be generalized for the case of a non-resonant imaging beam, using

$$b(x, y, \Delta_{AI}) = \sigma_0\ \frac{1}{1 + 4\frac{\Delta_{AI}^2}{\Gamma^2}}\ \rho_{2D}(x, y)\ , \tag{4.10}$$

allowing to perform the AI for probing clouds with high optical depth.

For a dense atomic sample, where not only we have a too high optical depth but also a high spatial density, the equations above are not valid since we cannot consider a linear behavior of $\rho_{2D}(x, y)$ with the refractive index of the sample. This represents an important limitation of the AI to quantitatively obtain the density profile of a dense cloud.

PHASE CONTRAST IMAGING THEORY

In the PCI case, the 2D density profile is obtained through the measurement of the phase shift induced by the atoms on the incident light, which is related to the optical depth at resonance:

$$\phi(x, y, \Delta_{\mathrm{PCI}}) = -\frac{\frac{\Delta_{\mathrm{PCI}}}{\Gamma}}{1 + 4\frac{\Delta_{\mathrm{PCI}}^2}{\Gamma^2}}\, b_0(x, y)\ . \tag{4.11}$$

In order to apply this technique, we need to choose a large detuning for the imaging beam, such that the light absorption is negligible and we will have only dispersive effects on the light. We can estimate the value of the detuning by noticing that for having a good signal-to-noise ratio on the phase shift measurement, its maximum value $\phi_{\max}$ should be close to one. Then, for a cloud of $b_0 \gg 1$, we obtain the order of magnitude of the light detuning as follows

$$|\Delta_{\mathrm{PCI}}| \sim b_0\ \frac{\Gamma}{4}\ . \tag{4.12}$$

The phase induced by the cloud in the PCI is not simply obtained by the intensity distribution of the transmitted imaging beam. This makes the PCI protocol more complicated than the AI, being necessary to perform a kind of interferometric measurement between the incoming electric field and the electric field scattered by the atoms (85).

Let us first, separate the transmitted light as a combination of the incoming $E_{probe}(\mathbf{r})$ and the diffracted $E_d(\mathbf{r}, \Delta_{\mathrm{PCI}})$ electric fields:

$$\begin{aligned}\mathbf{E}_{t,\mathrm{PCI}}(\mathbf{r}, \Delta_{\mathrm{PCI}}) &= E_{probe}(\mathbf{r}) + E_{probe}(\mathbf{r})\left(e^{i\phi(x,y,\Delta_{\mathrm{PCI}})} - 1\right) \\ &= E_{probe}(\mathbf{r}) + E_d(\mathbf{r}, \Delta_{\mathrm{PCI}})\ .\end{aligned} \tag{4.13}$$

Including a controlled phase shift ϕ_P on the non-diffracted part of the transmitted light, the detected electric field at the camera position becomes:

$$\begin{aligned}\mathbf{E}_c &= e^{i\phi_P} E_{probe}(\mathbf{r}) + E_d(\mathbf{r}, \Delta_{\mathrm{PCI}}) \\ &= \left(e^{i\phi_P} + e^{i\phi} - 1\right) E_{probe}(\mathbf{r})\ .\end{aligned} \tag{4.14}$$

In this situation, the intensity recorded by the camera is given by

$$I_c(x, y) = I_0(x, y)\left[3 - 2\cos\phi(x, y) - 2\cos\phi_P + 2\cos\left(\phi(x, y) - \phi_P\right)\right]\ , \tag{4.15}$$

and the phase induced by the atoms can be calculated as a function of ϕ_P and the intensity of the transmitted light

$$\phi(x, y) = \phi_{atoms}(x, y) = \arcsin\left[\frac{\frac{I_c(x,y)}{I_0(x,y)} + 2\cos\phi_P - 3}{4\sin\frac{\phi_P}{2}}\right] + \frac{\phi_P}{2}\ . \tag{4.16}$$

In figure 22, we have shown the behavior of the equation (4.15) for different values of ϕ_P. Here, we can see a periodical dependence of I_c on ϕ_{atoms}, meaning that there is an infinite

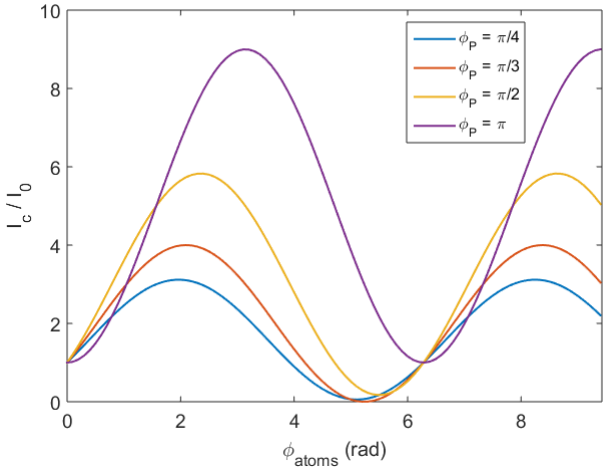

Figure 22 – Intensity detected at the camera v.s. the phase induced by the atoms, for different controlled phase shifts ϕ_P.

Source: By the author.

ensemble of values of the accumulated phase that gives the same transmission intensity. Note that the equation (4.16) is only valid for the interval $(\phi_P - \pi)/2 \leq \phi_{atoms} \leq (\phi_P + \pi)/2$. For other values of ϕ_{atoms} we would observe phase jumps in the recorded image and it would be necessary to implement an algorithm to unwrap the phase.

Another thing to discuss about the graph of fig. 22 is the choice of the value for the phase shift ϕ_P. We can use any value on the experimental implementation of the PCI system but there are some advantage and disadvantages. For example, the phase $\phi_P = \pi/3$ keeps the minimum value of I_c strictly zero, yielding a better contrast on the image since $(I_{max} - I_{min})/(I_{max} + I_{min}) = 1$. The phase $\phi_P = \pi$ guarantees a maximum absolute amplitude of $(I_{max} - I_{min}) = 8I_0$ but its behavior is quadratic for small values of ϕ_{atoms}, which adds noise to the measurement of lower density regions within the sample, like the wings of a Gaussian cloud, for example. The phase shifts $\pi/2$, $\pi/3$ and $\pi/4$ have an approximately linear response for small accumulated phases, making them more suitable for the PCI system.

4.3.2 PCI Setup

Experimentally, we can produce the controlled phase shift mentioned above by using a phase spot placed in the focal plane of the non-diffracted probe beam, which is the plane wave part of the beam. In figure 23 we can see a simplified scheme for a common PCI system where the phase shift is created by a glass plate with a spot at the center. Here, the blue color represents the non-resonant probe beam and also the non-diffracted part of the light after the atoms position; the red color represents the light diffracted by the atoms. The atoms are imaged with the first lens of focal length f_1, placed at the distance

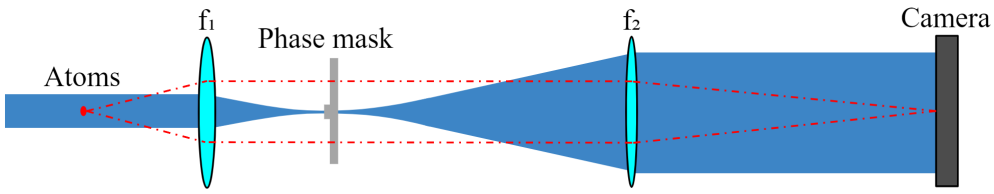

Figure 23 – Schematic representation of the PCI setup. The blue non-resonant beam interact with the atoms and, with the use of two lenses, an image of magnification $M = f_2/f_1$ is created at the camera position. The phase spot in placed in Fourier plane of the first lens.

Source: By the author.

f_1 from the atomic ensemble. An image is created by placing a second lens of focal length f_2, at the distance $f_1 + f_2$ from the first lens and the distance f_2 from the camera.

The light used for this imaging system is taken from an extra blue laser available in our lab that we call "Baby Blue". The details of this laser system will be given in the next chapter. The important thing to remark here is that we are able to lock this laser for several frequencies until approximately 1400 MHz from the resonance condition of the blue transition.

In our lab, we do not have a glass plate to create the phase shift, so we used an Spatial Light Modulator (SLM) instead. Our real experimental setup is shown in figure 24. We first expand the incoming beam with a telescope until a waist of 680 µm, which is good enough to image our dense cloud since the ODT should have a transverse size of approximately 7 µm. After passing through the atoms, the non-diffracted light is focused by a lens of 150 mm and the SLM is placed at the Fourier plane of this lens. The phase pattern introduced to the SLM was made in Matlab and it is shown in figure 25, where we see the phase disk at the center allowing to shift only the phase of the probe light but not the light diffracted by the atoms. After being reflected by the SLM, the image is built by the use of a second lens of 500 mm and the magnification is $M = 500\text{mm}/150\text{mm} = 3.33$. The image of the atomic cloud is captured by a CMOS camera with 5 µm of pixel size.

Using a SLM to filter the light have some advantages and disadvantages, or specific considerations to take into account in order to have a proper application of this device. An important step to start using the SLM is to use a lookup-table that will provide a linear phase response to the gray levels introduced to the device. This lookup-table, shown in figure 26, was generated following the recommendations of the SLM manual and we got a linear behavior of the phase from 0 to 2π in relation with the gray levels from 0 to 256.

Another consideration to use the SLM is that its pixelated nature produce diffraction effects which give place to noise in the light reflected by the SLM itself. This problem

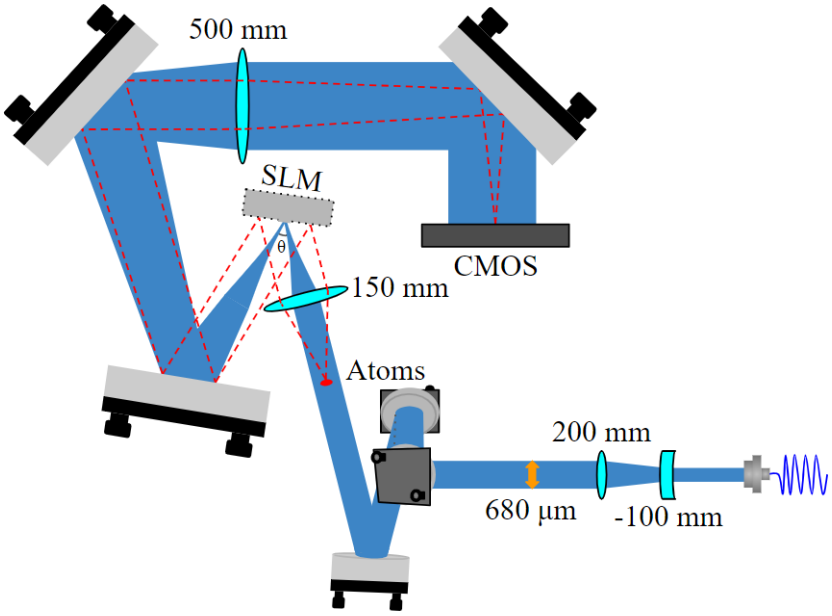

Figure 24 – Real experimental setup of our PCI system. Similar as the previews figure, the blue and red colors represent the non-diffracted and the diffracted parts of the imaging beam. The angle of reflection on the SLM is $\theta/2 = 16.4°$.

Source: By the author.

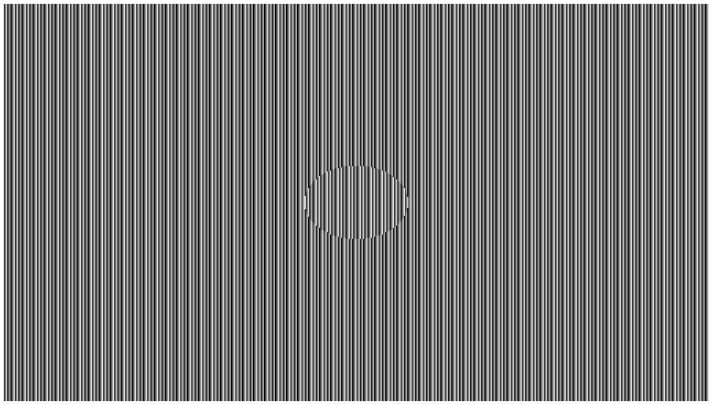

Figure 25 – Pattern introduced to the SML, which is a superposition of a phase disk with a diffraction grating. The elliptical shape of the phase disk is related to the projection of the light due to the angle of incidence on the SLM plane.

Source: By the author.

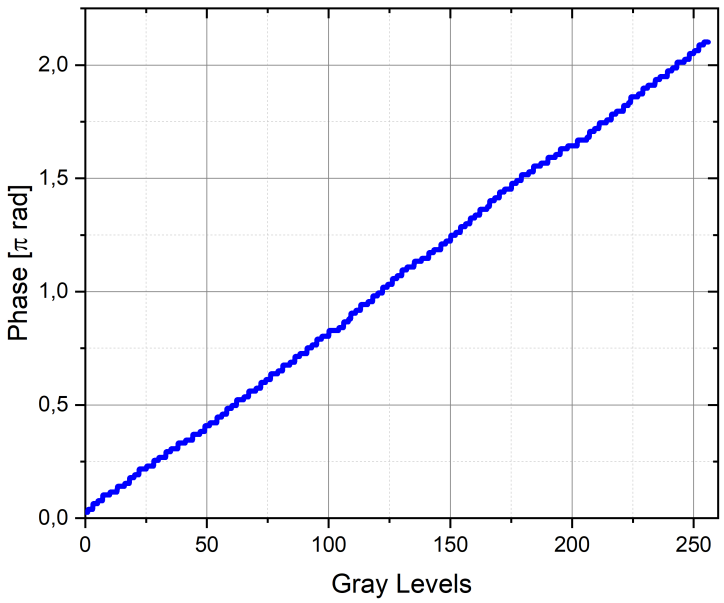

Figure 26 – Lookup-table generated in order to calibrate the SLM device.

Source: By the author.

can be addressed by adding a separate diffraction grating to "clean" the light (see fig. 25). In this way, the zero-order of diffraction will contain the noisy light that does not experience any phase shift due to the SLM pattern, and the first-order of diffraction that contains the phase shift imprinted by the SLM. In our scheme for the experimental setup of fig. 24, we just considered the first-order of diffraction since is the one relevant for the PCI system. The grating separation was chosen to be 10 px (being the pixel size equal to 8 μm); higher separations lead to a better efficiency in the intensity of the first-order of diffraction, nevertheless, in these conditions, all diffraction orders are not well separated, which is a problem for the experimental implementation of the imaging system.

Note that the system described in figure 24 works not only for producing Phase Contrast Imaging but also for Absorption Imaging. In order to make the AI, we just need to put the imaging beam on resonance and to eliminate the phase disk of the SLM pattern.

The elliptical shape of the disk is because of the angle of incidence of the light on the SLM screen, which is 16.4°. As the waist of the imaging beam is $w_0 = 680$ μm, we can calculate its waist at the focus after passing by the lens of focal length $f = 150$ mm: $w_f = \frac{\lambda f}{\pi w_0} = 31.8$ μm. Our SLM accepts a maximum intensity of approximately 2 W/cm^2; for the waist calculated before, we have that the power limit for the beam is $P_{max} = \frac{\pi I_{max} w_f^2}{2} = 31.75$ μW. We usually use values between 20 μW and 25 μW for the power of the PCI beam.

For these conditions of the imaging beam, we can estimate the radius of the phase disk R_P. As all the non diffracted light must be phase shifted by the disk, the radius of this disk should ideally be $R_P \gtrsim 3\mathrm{w}_f = 95.4$ μm. At the same time, in order to implement the interferometric measurement described before, no diffracted light should suffer a phase shift, and this will represent an upper limit for the parameter R_P.

The main advantage of using a SLM is to be able of controlling every parameter of the phase mask. We ended up using phases of $\phi_P = \pi/4$ or $\phi_P = \pi/3$ for the disk since these values suited well to observe the crossed ODT in every condition of the atomic cloud. The phase $\pi/4$ give place to an image with a small contrast (when compare with the other phases considered in fig. 22), allowing the probing of a dense cloud without being necessary the use of a very large detuning for the imaging beam.

Using the flexibility of the SLM, we experimentally investigated the effect of the phase disk radius R_P on the image of the atomic cloud. As we can see in figure 27, measuring the number of atoms for an specific condition of our crossed ODT, we identify a plateau at the range 100 μm $\lesssim R_P \lesssim$ 250 μm, which is compatible with the predictions made before. For values of $R_P \lesssim 100$ μm, the non-diffracted part of the light is not fully contained within the phase disk, and the number of atoms drops quickly to zero when R_P drops to zero. This is expected since the absence of a phase disk leads to no signature of the phase shift caused by the atoms at the camera position. For $R_P \gtrsim 250$ μm, the phase disk will also shift in phase part of the diffracted light, affecting the information of the atomic profile and producing a reduction of the measured number of atoms.

In order to validate the implemented imaging system, we wanted to find a condition where it is possible to compare the characteristics of the atomic cloud by using simultaneously the Phase Contrast Imaging and the Absorption Imaging techniques. With this goal, we created an experimental sequence that makes a PCI of the cloud in the vertical direction and, after a time-of-flight of 4 ms, produces an AI of the cloud in the horizontal direction. This is only possible due to the nondestructive behavior of the PCI technique.

For the set of measurements used to make a comparison between the AI and PCI, we kept the phase disk constant in $\phi_P = \pi/3$ and used four different detunings for the PCI beam. We explored different conditions for the cloud, increasing the number of atoms and the optical depth, by changing the power of the Blue MOT experimental ramps. The left graph of figure 28 shows the obtained values for the number of atoms when using both imaging systems. We can find here two realizations of the measurements for each detuning, which help us to visualize that the dispersion of the results is not related with the detuning but with a shot-to-shot fluctuation. Even when we have these fluctuations, it is clear the linear correspondence between the measured values for all conditions.

Another test that we made using the same set of measurements was to check the linear correspondence between the optical depth multiplied by the square of the cloud size

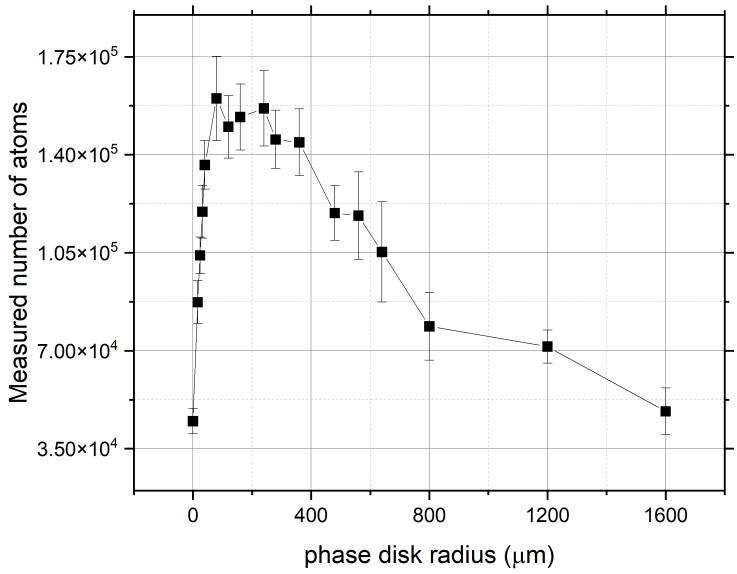

Figure 27 – Number of atoms measured by imaging the atomic cloud using the PCI technique as a function of the radius of the phase disk produced with the SLM.

Source: By the author.

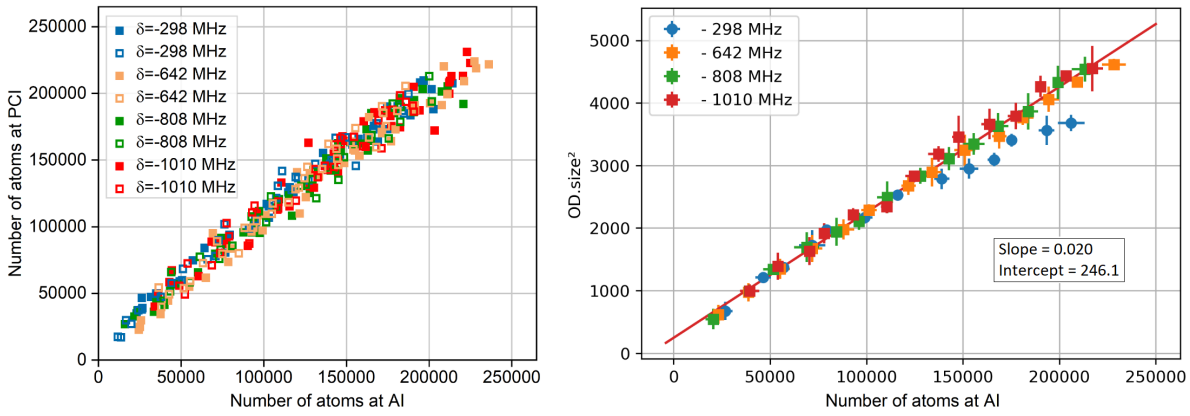

Figure 28 – Set of measurements performed to compare the Absorption Imaging and Phase Contrast Imaging techniques. (Left) Measurement of the number of atoms by using both imaging systems. (Right) Measurement of the optical depth multiplied by the square of the cloud size at PCI as a function of the Number of atoms at AI. The results of the linear fit, represented by the red line, can be seen at the graphic.

Source: By the author.

$(b_0 \cdot R^2)$, measured using the PCI technique versus the Number of atoms N using AI. For a Gaussian cloud, these parameters are related through the expression $N = (b_0 R^2 k_0^2)/3$, whose deduction will be shown at the next chapter. In the right graph of figure 28, we can see the expected linear behavior for detunings greater or equal to 642 MHz. Note that here, we made an average of the parameters N, b_0 and R^2 by dividing the data in 15 small squares that represents subsets with similar number of atoms. The error bars in the graph are the standard deviation on each subset. The red line represents a fitting of the data and the results of the slope and intercept were (0.020 ± 0.002) μm^2 and 246.1 ± 27, respectively. According to the value of wavenumber k_0 associated to the atomic blue transition, we should have an slope of ~ 0.016 μm^2, which is close to the measured value.

The data for the 298 MHz detuning does not follow a linear behavior due to saturation of the phase contrast imaging for high optical depths. This saturation effect gave place to the observation of an smaller optical depth but an slightly higher size of the cloud, coincidentally remaining the number of atoms at PCI linear with the number of atoms at AI. That is the reason why the saturation is clear at the right graph but not the left one. The detuning of 298 MHz was not included in any fitting procedure.

4.4 Optical Molasses

Due to the small volume of our crossed ODT, we have a small efficiency of the atomic transference from the Red MOT to this new trap. In order to circumvent this, we implemented an additional stage of cooling by performing an optical molasses with the 689 nm red light. The application of this technique demands a cancellation of the external magnetic field, since an uncompensated magnetic field can give place to regions where the equilibrium velocity is not zero, producing a lost of atoms during the cooling process. A magnetic field of $B = 5$ mG is already enough to shift the energy levels in a unity of $\Gamma = 7.6$ kHz, which is the natural linewidth of the red transition. Therefore, we need a cancellation of the magnetic field with a very high precision.

4.4.1 Magnetic Field Cancellation

Around the science chamber, we have implemented three pairs of Helmholtz coils that allow us to introduce a magnetic field in the three spatial directions. The cancellation of the magnetic field consist in finding the right values for the coils' current that compensates the external magnetic field, creating an environment of B = 0 at the position of the atomic trap.

As we needed a very good accuracy in the cancellation of the magnetic field, we developed the following procedure. First, we implemented a molasses stage at the end of the Red MOT sequence with a duration time of 24 ms. Scanning the frequency of this red light used for the molasses stage, we are able to identify the three magnetic sublevels

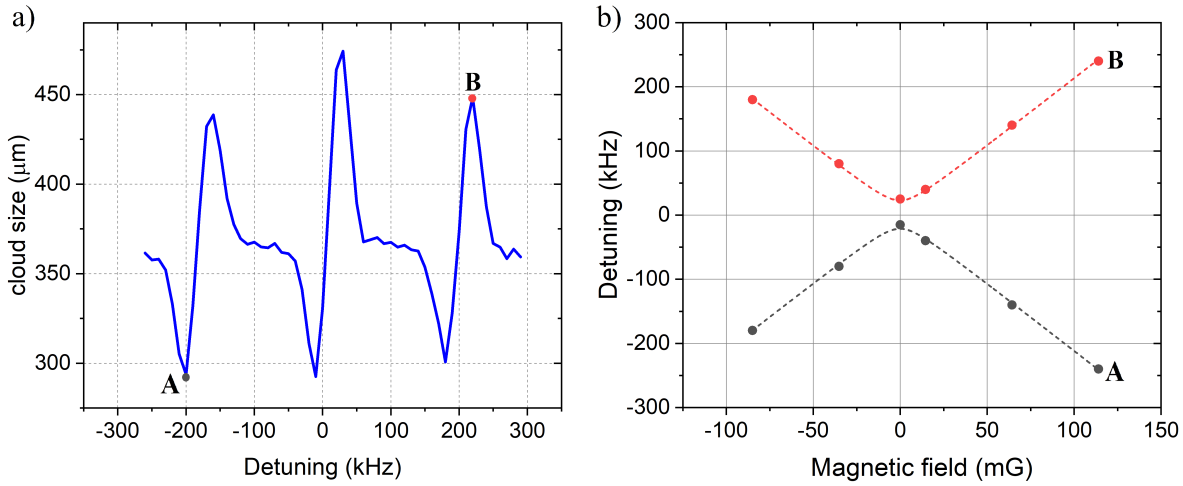

Figure 29 – Magnetic field cancellation process: a) Measuring the size of the cloud varying the detuning of the molasses light, it can detected the position of the magnetic levels. The points **A** and **B** represent the positions for the levels $m_j = -1$ and $m_j = 1$, respectively. b) Repeating the measurement for different values of the magnetic field, it will be observed a shifting of the levels $m_j = -1$ and $m_j = 1$, and the magnetic field is zero when the positions **A** and **B** get closer.

Source: By the author.

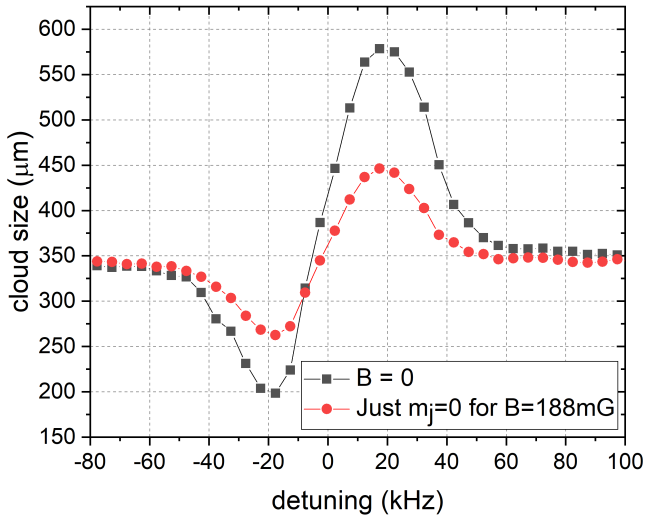

Figure 30 – Comparison of the cooling efficiency between the dispersive curve of just the central level $m_j = 0$ for a non-zero magnetic field of $B = 188$ mG and the collapse of the three dispersive curves in just one curve once the magnetic field is cancelled.

Source: By the author.

$m_j = \{-1, 0, 1\}$ of the $^3P_1$ state. When the magnetic field is different than zero, the Zeeman effect leads to an splitting of the excited state, separating the levels $m_j = -1$, $m_j = 0$ and $m_j = 1$. The figure 29**a** shows a graphic of the size of the cloud as a function of the detuning between the molasses light and the $^1S_0 \Leftrightarrow {}^3P_1$ transition. Here, we can observe three dispersive curves around the resonance condition of the three excited levels. This behavior is expected for the optical molasses since the beam below the resonance will cool the cloud while above the resonance will heat the cloud. As a consequence of these variations in the temperature, the cloud will be compressed or expanded and the effect is visible while measuring the cloud size.

Changing the magnetic field, we observe a frequency shifting of the excited levels $m_j = -1$ and $m_j = 1$, while the level $m_j = 0$ remains at the same position. Plotting the position of the levels $m_j = -1$ and $m_j = 1$ (represented by the points **A** and **B** in fig. 29), we stop when the three dispersive curves collapse in just one curse at the position of the $m_j = 0$ resonance. This condition is the one when **A** and **B** get closer, as we can see in figure 29**b**. Note that the position of the levels is determined by the center of the dispersive curves, not by the extremes. But following the extremes is a better way to follow the positions of each level. This procedure need to be done for every spatial direction in order to fully cancel the magnetic field.

In order to compare the effect of the optical molasses for a zero and non-zero magnetic field, we made the graphic shown in figure 30. Here, we plotted the only dispersive curve observed when the magnetic field is completely cancelled and just the central level $m_j = 0$ for a magnetic field of $B = 188$ mG. Comparing these two curves, we see an improvement of the cooling for a cancelled external magnetic field, since for a small red detuning of the molasses light, we obtain a significant compression of the atomic cloud.

4.4.2 Experimental Ramps and Calibrations

Once the magnetic field was completely cancelled, we included the molasses stage in the experimental sequence used for creating the crossed ODT. At figure 31, we can see the whole experimental sequence very well detailed, with the corresponding values of the light intensity and frequency for each temporal stage. The part of the experimental sequence used to create the blue and red Magneto Optical Traps, were already explained in the previous chapter. The main difference here is the presence of the infrared light to produce the crossed ODT and the optical molasses stage during the superposition of the red light with the ODT beams.

As mentioned before, both horizontal and vertical ODT beams are simultaneously turned on 300 ms before turning off the red light and kept on more 40 ms of holding time. After the fourth ramp of the red MOT, we turn off the magnetic field of the MOT coils but keep the red light for 70 ms in order to produce the optical molasses. During this

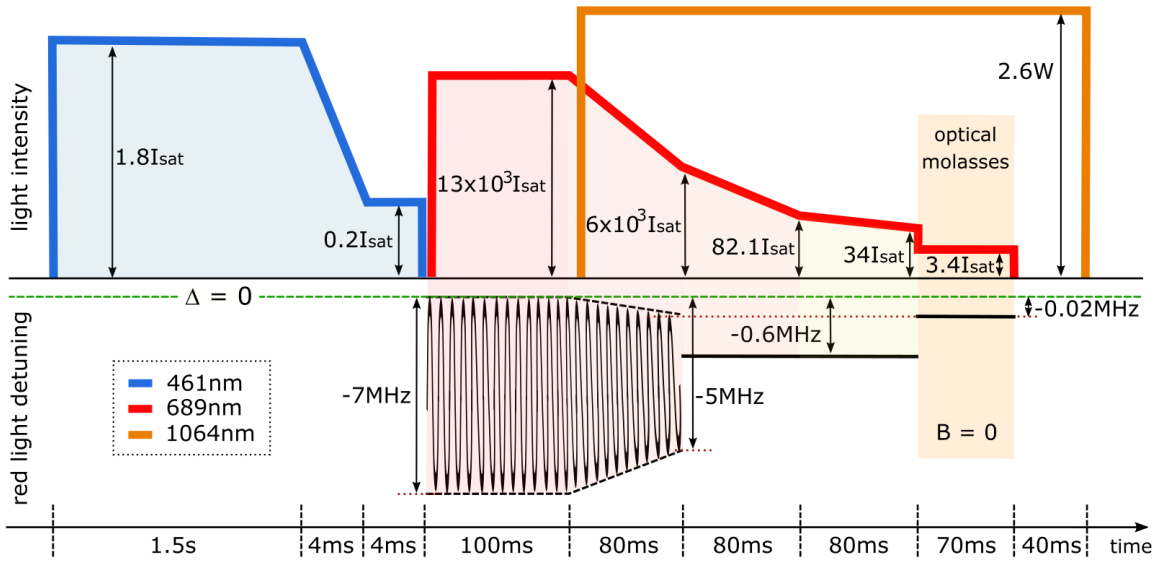

Figure 31 – Experimental sequence for obtaining the crossed ODT. The blue, red and orange colors represent the power ramps used for the light with wavelengths 461 nm, 689 nm and 1064 nm respectively. For the molasses stage, the quadrupolar magnetic field of the red MOT is off and also the external magnetic field is cancelled.

Source: By the author.

stage, the intensity and detuning of the red light are kept constant at the values $3.4I_{sat,red}$ and -0.02 MHz respectively. At figure 32 can be found optimization curves for the duration time of the molasses stage (fig. 32**a**) and the power of the molasses red light (fig. 32**b**). In both cases, we plotted the behavior of the optical depth and the size of the crossed ODT. We chose the values that present a higher optical depth with the lower size, since is the condition with the best density at the lower temperature. We found in both measurements regions where the optical depth remained approximately constant in a maximum value while the size continued decreasing. Therefore, the optimal values for the molasses time and the power are 70 ms and 2.6 μW (equivalent to $3.4I_{sat,red}$) respectively.

Another important optimization is the detuning of the molasses light. At this point we need to worry about the differential AC Stark shift that the ODT beams produce in each transition of the $^3P_1$ state. We performed some calculations that simulate the Stark shift considering the powers and the real configuration of polarization for both ODT beams: polarization π for the horizontal beam and polarization $\sigma+$ for the vertical beam, taking z as the quantization direction. As we can see in figure 33**a**, with these polarizations we minimize the Stark shift of the $m_j = -1$ level. In this graph, the calculations are made along the center profile of the x direction (same propagation direction of the ODT horizontal beam) for the crossed ODT. These simulations were mainly carried out by Pablo Gabriel Santos Dias, one of my laboratory colleagues.

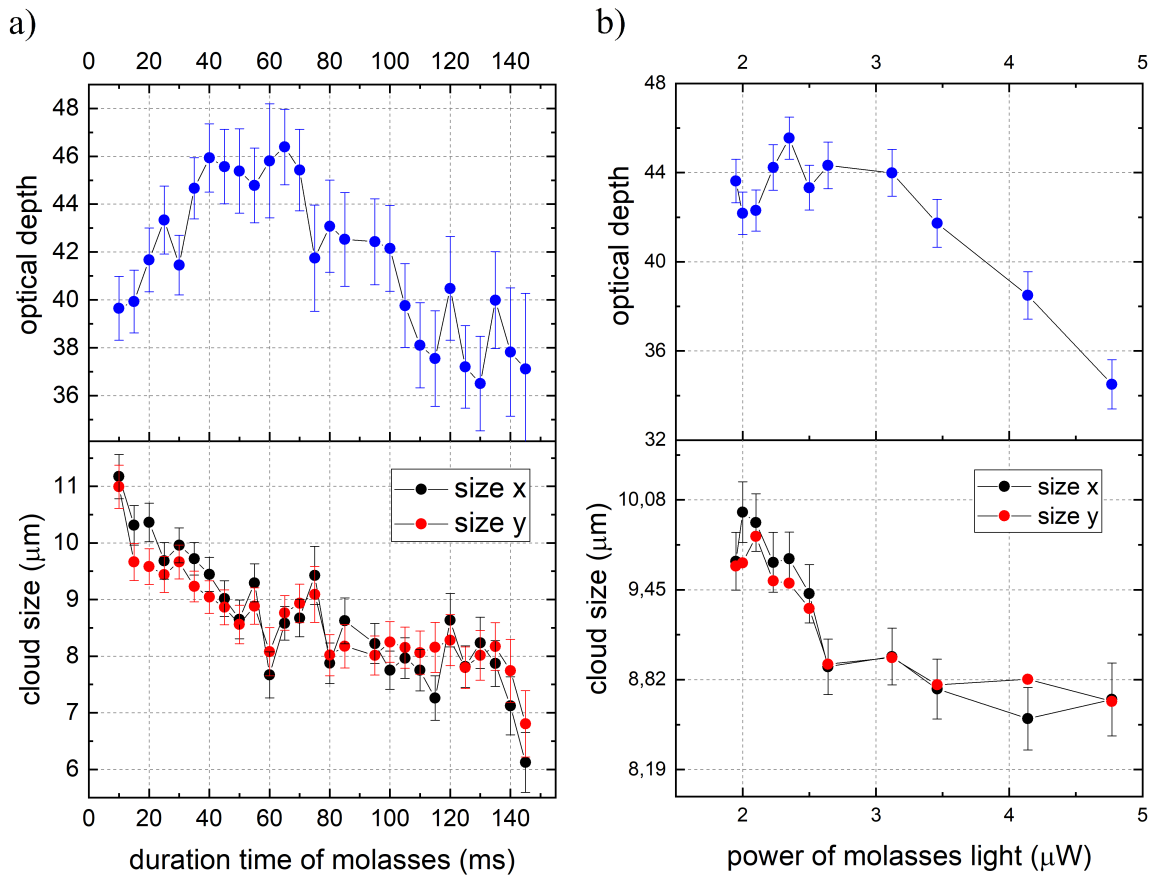

Figure 32 – Optimization curves for the crossed ODT. (a) optical depth and size of the cloud for different duration time of the molasses light pulse, and (b) optical depth and size of the cloud for different powers of the molasses light.

Source: By the author.

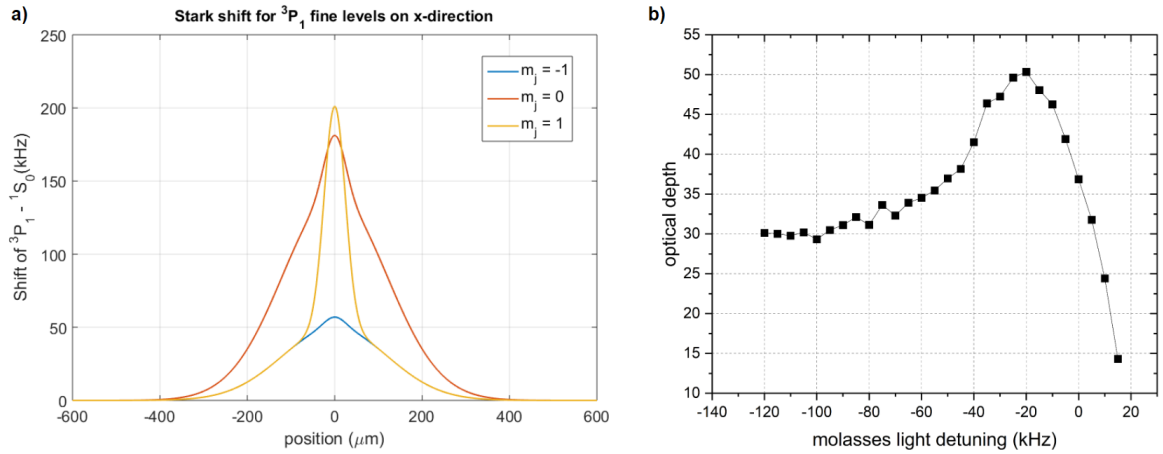

Figure 33 – (a) Calculated Stark shift produced by the ODT beam on the $^3P_1$ levels. (b) Optical depth v.s. the detuning of the molasses light.

Source: By the author.

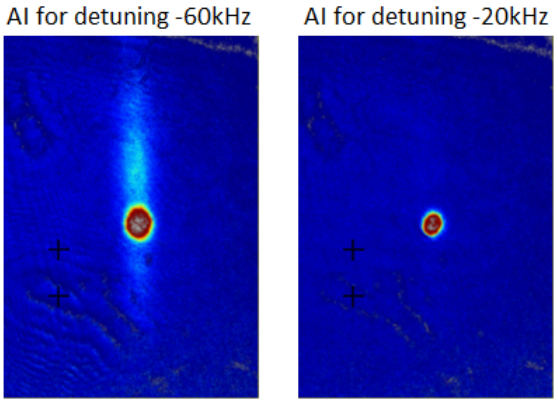

Figure 34 – Absorption images for two different conditions of the molasses detuning curve of figure 33**b**, which gives a qualitative information of the effect produced by the optical molasses.

Source: By the author.

Figure 33**b** shows the behavior of the optical depth while scanning the detuning of the molasses light. Even when we were expecting a shift of the $^3P_1$ levels due to the presence of the infrared beams, the implementation of the molasses showed that the maximum optical depth is for the same detuning as the molasses without the ODT beams (see fig. 30), which is -20 kHz. With this result, we can conclude that the biggest effect of the molasses produced during the superposition with the ODT is for cooling the atoms that are not in the deeper crossed potential, but the ones that remained in the more shallow potential created by the horizontal ODT beam only. Complementing this interpretation, we produced two absorption images with qualitative information of the crossed ODT at the molasses detunings -60 kHz and -20 kHz. The images can be seen at figure 34, and here it is clear how the implemented extra stage of cooling, recycles atoms that remained outside the crossed ODT after the transference from the Red MOT.

4.5 Final Characterization of the ODT

The final characteristics of our crossed ODT can be obtained by producing a PCI to probe the atomic system in situ. Most part of the parameters can be directly extracted by this image: as the number of atoms, the size in the transverse direction and the optical depth. The size in the longitudinal direction can be calculated considering the characteristics of the ODT beams and the measured oscillation frequency in the z axis. Then, the temperature can be estimated by using the values for the size of the cloud.

Summarizing the characteristics of our ODT, for the specific cloud shown in figure 35, we have:

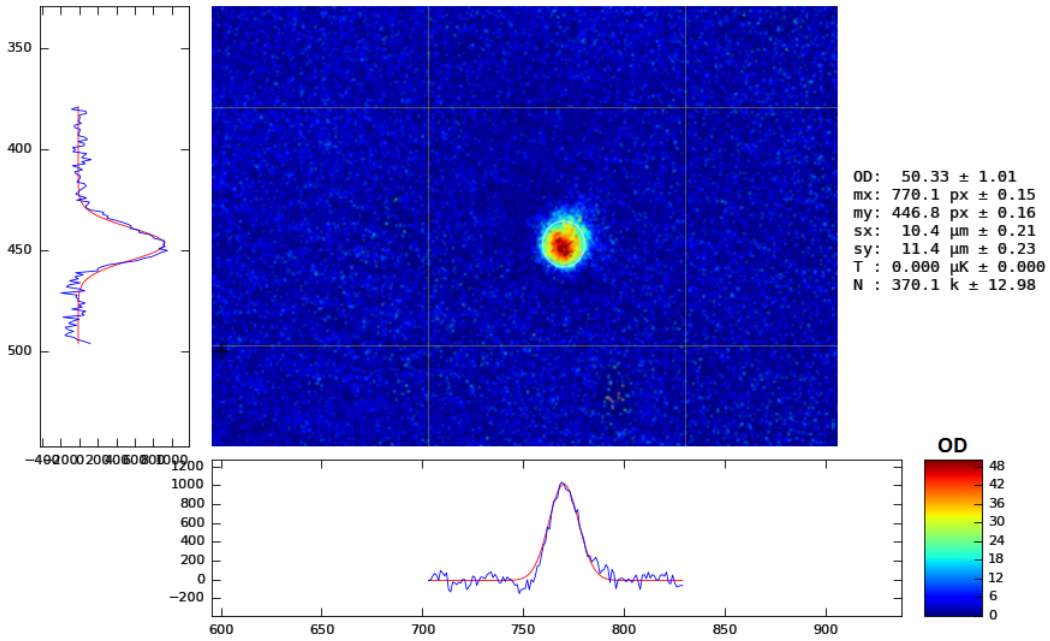

Figure 35 – Phase Contrast Imaging for the crossed ODT in situ. The colored scale represents the optical depth of the cloud.

Source: By the author.

- Number of atoms: 370000
- Optical depth: 50.33
- Sizes of the cloud at $1/\sqrt{e}$, in (x, y, z): $(10.4,\ 11.4,\ 4.1)$ µm.
- Temperature: 1.43 µK
- Spatial density at the center, in unities of $1/\lambda^3$: $\rho\lambda^3 = 4.4$.

The value for the spatial density seems to be kind of low when compare to the Ioffe-Regel criterion presented in the introduction of this document. However, we decided to move on and try investigate the presence of density effects using this cloud.

Both processes implemented for cooling and imaging of our dense cloud, represent important experimental results of this PhD project, and we are writing an article that should be submitted in the next weeks.

5 SIMULATIONS BASED ON COUPLED DIPOLE MODEL

In this chapter will show and discuss the results of some simulations applying the coupled-dipole model. These simulations are about the first set of measurements that we want to perform in the dense regime: coherent transmission measurements of a light beam focused on the atomic cloud.

5.1 Geometry of the Cloud

The first step of the simulations consists in creating an atomic cloud. For this purpose, there is a random selection for the position of N atoms according to some geometry and probability density $\rho(x, y, z)$. In these simulations, we are able to produce clouds with different geometries: Gaussian cloud, uniform sphere, uniform cube or uniform slab.

As we saw in Chapter 2, the optical depth at the center of the atomic cloud, i.e. position $(x = 0, y = 0)$, is given by

$$b_0 = \sigma_0 \int_{-\infty}^{\infty} \rho(0, 0, z)\, dz \ , \tag{5.1}$$

where $\sigma_0 = \frac{3\lambda^2}{2\pi} = \frac{6\pi}{k_0^2}$ is the cross-section at resonance, λ is the wavelength of the incoming light at resonance and k_0 is the modulus of the wavevector of light.

In our simulations we usually introduce the parameters of the cloud: b_0, transverse length R and spatial density in units of $\rho\lambda^3$. Thus, depending on the geometry, we can estimate the number of atoms N and the longitudinal length L.

The real atomic cloud that we obtain in the lab has a Gaussian distribution, however we are also interested in the uniform slab geometry since it was used for some tests in order to validate the simulations.

5.1.1 Gaussian Cloud

The density profile of a Gaussian cloud of N atoms, with transverse and longitudinal radius at $1/\sqrt{e}$ equal to R and L respectively, is given by

$$\rho(x, y, z) = \frac{N}{(2\pi)^{3/2} R^2 L} e^{-\frac{x^2+y^2}{2R^2} - \frac{z^2}{2L^2}} \ , \tag{5.2}$$

The optical depth at the center of the cloud, using (5.1), is equal to

$$b_0 = \frac{6\pi}{k_0^2} \int_{-\infty}^{\infty} dz \frac{N}{(2\pi)^{3/2} R^2 L} e^{-\frac{z^2}{2L^2}} = \frac{3N}{(k_0 R)^2} \ . \tag{5.3}$$

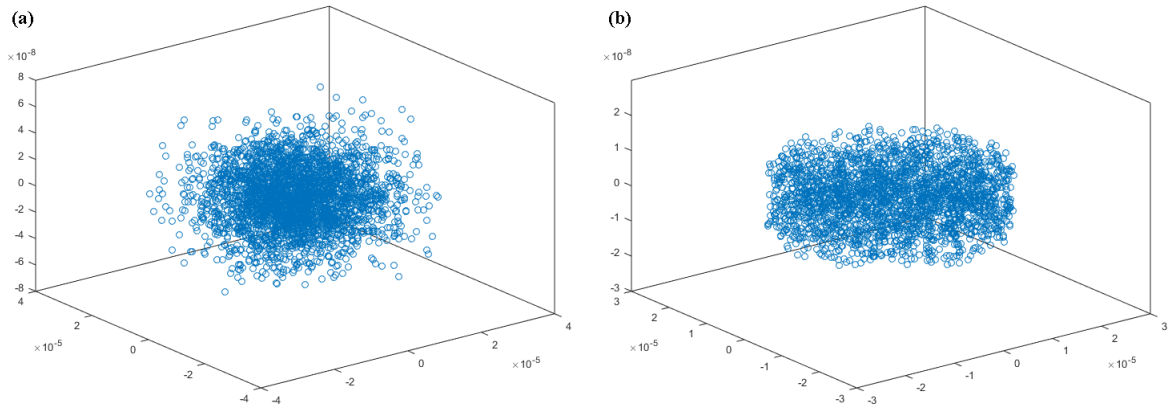

Figure 36 – Random distribution of the atoms position following (a) a Gaussian geometry and (b) an uniform slab. All three axis are in micrometer scales.

Source: By the author.

In this case, for introduced values of b_0, R and $\rho\lambda^3$, we have:

$$N = \frac{b_0(k_0R)^2}{3} \tag{5.4}$$

and

$$L = \frac{N(2\pi)^{3/2}}{(\rho\lambda^3)R^2k^3} \ . \tag{5.5}$$

An example of a Gaussian cloud produced by the simulations can be seen in figure 36a. Here we considered a large number of atoms and sizes of $R = L = 1$ μm.

5.1.2 Uniform Slab

The density profile of a slab of N atoms with uniform density, which transverse and longitudinal radius are R and L respectively, is given by

$$\rho(x,y,z) = \begin{cases} \frac{N}{\pi R^2 L} & \text{if} \quad \sqrt{x^2+y^2} \leq R \quad \text{and} \quad |z| \leq \frac{L}{2} \\ 0 & \text{otherwise} \end{cases} \ , \tag{5.6}$$

The optical depth at the center of the cloud, using (5.1), is equal to

$$b_0 = \frac{6\pi}{k_0^2}\int_{-L/2}^{L/2} dz \frac{N}{\pi R^2 L} = \frac{6N}{(k_0R)^2} \ . \tag{5.7}$$

In this case, for introduced values of b_0, R and $\rho\lambda^3$, we have:

$$N = \frac{b_0(k_0R)^2}{6} \tag{5.8}$$

and

$$L = \frac{8N\pi^2}{(\rho\lambda^3)R^2k^3} \ . \tag{5.9}$$

An example if this kind of atomic distribution can be seen in figure 36b, where it was considered $R = 2$ μm and $L = 1$ μm.

5.2 Incident Beam

In our simulations, the atomic sample is excited by an incoming light beam that propagates along the z direction. The simulated beam can have a Gaussian distribution for the electric field amplitude or either being a plane wave. Here, we do not use a plane wave approximation since we are interested in the case where the transverse size of this beam is smaller than the transverse size of cloud. Therefore, the simulated beam is Gaussian as the one we are going to use for the coherent transmission experiments. For simulating the atomic excitation, the focus of the Gaussian beam coincides with the center of the atomic cloud, i.e. position $(x, y, z) = (0, 0, 0)$.

A Gaussian beam with electric field of amplitude E_0 at center and waist w_0 at the focus position, has a complex amplitude E_l of the electric field that depends on the position $\mathbf{R} = (x, y, z)$ as

$$E_l(\mathbf{R}) = E_0 \frac{\mathrm{w}_0}{\mathrm{w}(z)} e^{-\frac{(x^2+y^2)}{\mathrm{w}(z)^2} + ikz + i\frac{k(x^2+y^2)}{2R_c(z)} - i\phi_G(z)} , \tag{5.10}$$

where $\mathrm{w}(z)$ is the waist of the beam, given by

$$\mathrm{w}(z) = \mathrm{w}_0 \sqrt{1 + \left(\frac{z}{z_R}\right)^2} . \tag{5.11}$$

Here, z_R is the Rayleigh range, related to the wavelength of the light and the waist through the expression $z_R = \pi \mathrm{w}_0^2/\lambda$. Others physical quantities introduced in equation (5.10) are the radius of curvature of the wavefront $R_c(z)$ and the Gouy phase $\phi_G(z)$, given respectively by

$$R_c(z) = z\left(1 + \left(\frac{z_R}{z}\right)^2\right) \tag{5.12}$$

and

$$\phi_G(z) = \arctan\left(\frac{z}{z_R}\right) . \tag{5.13}$$

We can see in these expressions that the shape of a Gaussian beam of a given wavelength λ is governed solely by one parameter: the beam waist at the focus w_0. Hence, w_0 is the parameter of the beam that we introduce in the simulations, and from it we can estimate the Rayleigh range z_R, which is another relevant parameter for the simulations.

Note that the scalar function E_l, represents just the spatial dependence of the modulus of the electric field. Therefore, properties as the temporal dependence of the electric field or its polarization are not included in this function.

5.3 Applying the Coupled Dipole Model

To apply the Coupled Dipole Model, we simulate the atomic cloud and the incoming beam with very specific conditions, and study the optical response of the cloud using equation (2.42) considering the complex amplitude of the incoming beam as shown in equation (5.10). The atomic coherences in the steady state regime are computed by a diagonalization of the matrix kernel of the dipoles interaction (K). As the matrix K has dimension $3N \times 3N$, the greater the number of atoms, the longer it will take to perform the simulation and more memory will have to be allocated to the program. This represents a limitation of our simulations and we actually observed an upper limit of around 7000 atoms in the computer we used (with 16 GHz of RAM).

There are some important considerations that we must take into account while performing the simulations. First, we are interested in studying the case in which the transverse size of the cloud is greater than waist of the incoming beam ($R > \mathrm{w}_0$), so the light interacts with an approximately homogeneous region of the cloud in the transverse directions. In the other hand, we need to guarantee that the waist of the beam is larger than the wavelength of the light ($\mathrm{w}_0 \gtrsim \lambda$) so the paraxial approximation is valid. Considering $\mathrm{w}_0 \gtrsim 2.5\lambda$ should be enough for the application of the coherent transmission equation (2.42) (56). A second consideration is that the longitudinal size of the cloud needs to be smaller than the Rayleigh range of the incident beam ($L < z_R$) in order to guarantee that the whole beam is interacting with the atomic cloud.

Since the positions of the atoms inside the cloud are random, even when the system follows a specific distribution, the optical response of the cloud is going to be different in each realization of the simulation. For this reason we need to make more than one simulation for each condition and compute the average over the number of realizations. In the simulations that are going to be shown below, we took the average over more than 30 realizations.

In order to validate our simulations, we made some tests on the dilute regime since the optical response of low density atomic clouds is well known both experimentally and theoretically.

5.3.1 Beer-Lambert Law

In the section 2.3, it was discussed about a law that represents a relationship between the attenuation of light through a sample and the properties of that sample. According to this law, which is called Beer-Lambert law, the transmitted light through the sample follows an exponential decreasing behavior in relation to the optical depth at resonance, i.e. $T = e^{-b_0}$. This relation is only true for low density samples, where the absorption of the incoming light happens independently for each atom withing the atomic

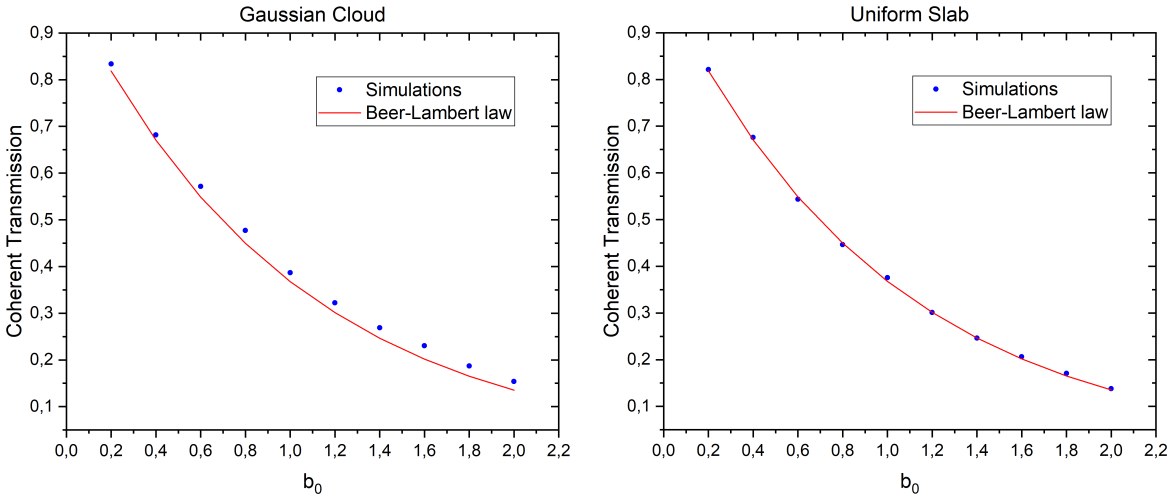

Figure 37 – Comparison of the simulations with the expected behavior according to the Beer-Lambert law. Both geometries considered are shown at the top of the graphics.

Source: By the author.

cloud.

The first test that we made using the simulations based on the vectorial CDM consisted on checking the compliance of the Beer-Lambert law in the dilute regime. For this, we considered both geometries mentioned before: a Gaussian cloud and a uniform slab. In both cases, the transverse size of the cloud was fixed on $R = 7$ µm and the spatial density $\rho\lambda^3 = 0.5$ (or $\rho/k_0^3 = 0.002 \ll 1$). The optical depth was varied from 0.2 to 2 and, at the same time, the number of atoms N and the longitudinal size of the cloud L changed. The waist of the beam was fixed at $w_0 = R/2$ and the Rayleigh range was greater than any value of L for each condition of the cloud.

In figure 37 we can see a perfect correspondence of the simulations and the Beer-Lambert law for the case of the uniform slab and a slight divergence of the curves for the case of the Gaussian cloud. This can be explained by the fact that the Beer-Lambert law used to compare considers an homogeneous density of the sample in the transverse direction, which can be fully guarantied only for the uniform slab geometry. However, we also observe a good agreement for the Gaussian cloud case.

5.3.2 Coherent Transmission Spectra

Simulating the real conditions of our atomic cloud, obtained by the Optical Dipole Trap, is impossible for us because of the number of atoms limitation ($N \lesssim 7000$). We could only simulate the real size of our cloud in the dilute regime, but the dense regime requires a larger number of atoms. In order to create similar conditions with respect to the

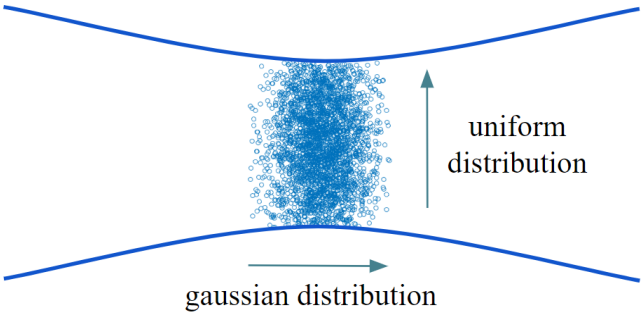

Figure 38 – Atomic cloud considered in the simulations, in which we have two different distributions for the transverse and longitudinal directions. The two blue lines represent the Gaussian beam focused at the center of the cloud, with waist equal to the transverse size of the atomic distribution.

Source: By the author.

experiment, we created a model that consider a cloud with a Gaussian distribution in the longitudinal direction and a uniform transverse distribution, as can be seen in figure 38. The longitudinal size is $L = 2.23$ μm, similar to our experimental cloud. The transverse size of the sample, as well as the waist of the incident beam, is $R = \mathrm{w}_0 = 1$ μm. The uniform transverse distribution allow us to simulate the interaction of the beam with an homogeneous part or the cloud, that would be the experimental case of a beam smaller than the Gaussian atomic cloud. Also, the condition $R = \mathrm{w}_0$ is equivalent to consider only the atoms of the cloud that actually interact with the beam. The longitudinal Gaussian distribution, apart from being the actual geometry of our real cloud, is also important for the simulations since allow us to avoid cavity effects inside the cloud.

In the conditions described above, we performed a first group of simulations building coherent transmission spectra for different values of N. As both sizes of the cloud were fixed, increasing N is equivalent to simultaneously increase the spatial density and the optical depth. The spectra are shown in figure 39 with their respective densities. For a spatial density of $\rho\lambda^3 = 0.1$, we observe a symmetric spectrum with a linewidth of approximately Γ, as we should expect in the dilute regime. The other curves show the behavior of the coherent transmission at high density where we can see a broadening of the spectra and the appearance of an splitting. The broadening of the transmission curves are a consequence of collective effects between the atomic dipoles, as it was explained in chapter 2. The splitting of the transmission curves, which is more clear in the logarithmic scale (right graphic of fig. 39), is a behavior that we never observed before in the bibliography. The distortion of the spectral profile indicates that we entered into a different physical regime, which is plausible due to the complex propagation effects of light in a dense atomic sample.

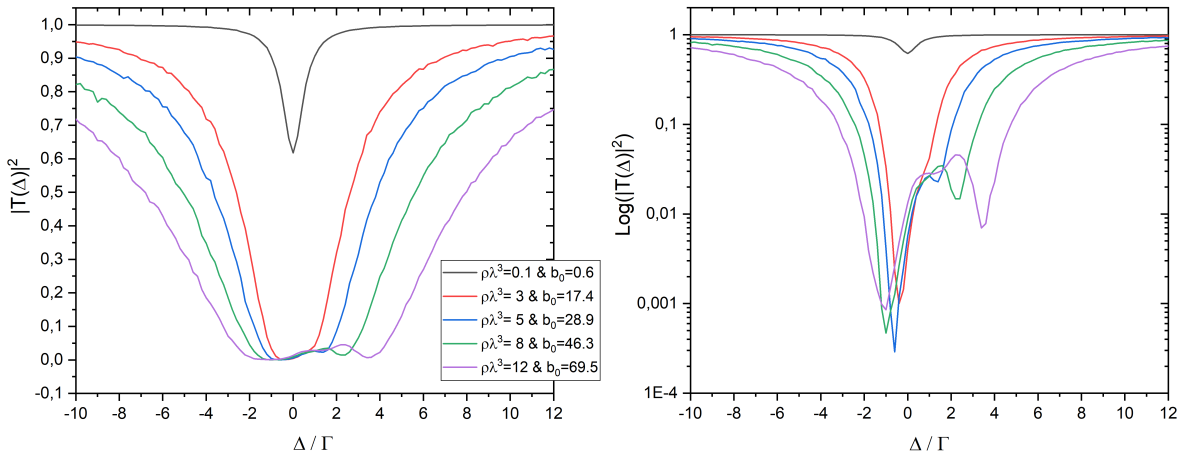

Figure 39 – Coherent transmission spectra for different atomic densities. The black line represents the dilute regime and the colored lines are for the dense regime spectra.

Source: By the author.

In order to understand the splitting of the transmission spectra, we made some new simulations: We fixed the optical density at a value for which the splitting is clear ($b_0 = 24.5$) by fixing the number of atoms at $N = 760$. The transverse size of the cloud was kept at the same value considered before ($R = 1$ μm), while the longitudinal size was varied in order to decrease the spatial density. These new spectra are shown in figure 40 and we can see a disappearance of the splitting for lower spatial densities. Then, we can conclude that the splitting in the transmission curves is an effect of the high spatial density rather than an effect of the high optical density. The increasing of the transmission shown in these graphics, for values of $L \geq 4$ μm, is unexpected since the optical density remained constant. This is provably related to the fact that the Rayleigh range of the incoming beam is no longer greater enough than the longitudinal size of the cloud.

Another interesting thing we can observe in this last set of graphics is the presence of a red-shift for the lower spatial densities. This is the collective Lamb shift, and its behavior is similar to the observed in some previous works (33, 49).

Even when we do not have an interpretation for the observed splitting, it would be very interesting to observe this effect on the coherent transmission experiments and check that is related to the complexity of the dense regime.

More recent simulations in the dense regime suggested that the splitting could be related to incoherent scattering of the incident light transmitted in the forward direction. This incoherent transmission would be given by multiple scattering of photons that end up projected in the incident light mode. In these simulations, it was filtered the polarization of the transmitted light selecting the same linear polarization of the incident beam and

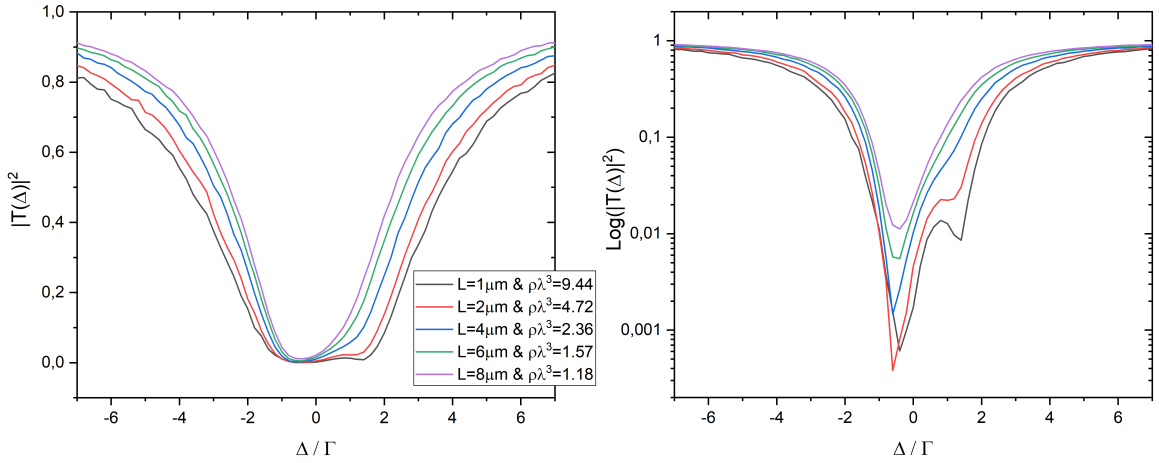

Figure 40 – Coherent transmission spectra for a fixed optical depth but different spatial densities.

Source: By the author.

the perpendicular one. The light with perpendicular polarization could only be given by incoherent transmission, and we realized that it has amplitude closer to the light transmitted with parallel polarization around the resonance condition of the transmission spectrum. So far, these are just assumptions and we would need to make a detailed study to have a conclusive interpretation of the splitting observed in the simulations showed in this chapter.

6 COHERENT TRANSMISSION

In this chapter, we will describe the experimental system implemented for the coherent transmission measurements. Specifically, we are going to give details about the laser used to perform these measurements, its frequency stabilization and the characteristics of the coherent transmission beam. Then, we will show some characterizations using the first coherent transmission spectrum in the dilute regime, and finally we will show the obtained results in the dense atomic regime.

6.1 Baby Blue Laser

We installed a new blue laser in our lab which is a tunable diode laser (DL pro) from Toptica Photonics, that operates at 461 nm. This laser is considerably smaller and simpler than our principal blue laser (TA-SHG), for this reason we use to call it "Baby Blue". In this kind of laser, a diffraction grating is used to foster single-frequency emission of the laser light. As different wavelengths of light are bent at different angles by the grating, the variation of the frequency could be done by modulating the grating angle of the laser diode.

Figure 41 shows the optical table for the Baby Blue laser, separated by three different sections. Following the order of the figure, we have the first section containing the laser itself and the light distributed to be coupled in three optical fibers. One of the fibers is used to monitor the frequency of the laser using a wavelength meter (or just wavemeter). A second fiber (Beating Fiber) is used to the frequency stabilization of the DL pro by performing a beating with a beam of the principal blue laser. A third fiber, which is a

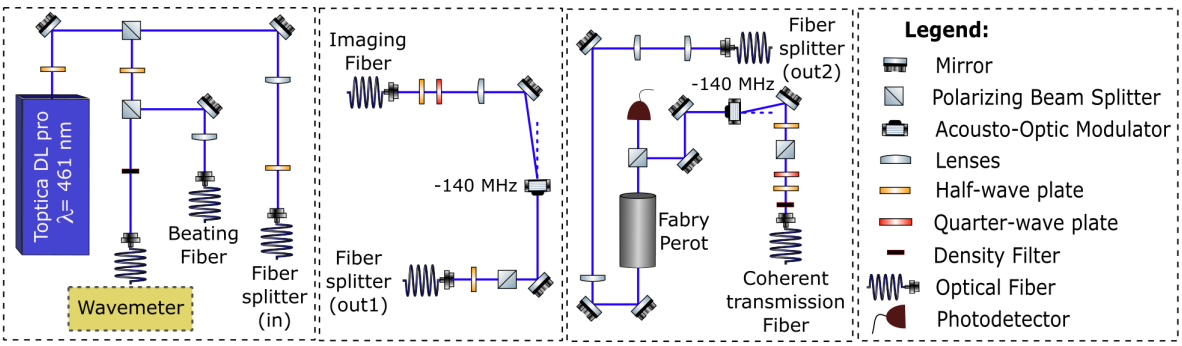

Figure 41 – Simplified scheme of the optical table for the Baby Blue laser. We see how the system is separated in three sections that are described in the main text.

Source: By the author.

combiner/splitter fiber, is used to split the light that will enter to the other two sections of the baby blue system.

The second section is where we prepare the laser beam before the Phase Contrast Imaging system, described in Chapter 4. Here, we basically just shift the frequency of the beam 140 MHz below the reference of the laser and couple the light on a fiber (Imaging Fiber) that brings the beam closer to the science chamber.

In the third section, we prepare the beam for the Coherent Transmission system. We first, shape the beam with lenses to enter in a Fabry-Perot cavity used to spectrally filter the light coming out from the diode laser. After the cavity, the light passes through an AOM that shift the frequency but also allow to make light pulses with small duration time. Finally, we control the power of the beam and couple it in a fiber. The light pulses are used to perform the coherent transmission measurements.

6.1.1 Frequency Stabilization

For the stabilization of the frequency, we implemented a frequency offset locking. First, we capture the beating signal between a beam of the principal blue laser (stabilized by the saturated absorption spectroscopy technique) and a beam of the laser we want to stabilize. This beating is done by introducing small portions of both laser beams in a combiner fiber, and the superposition of the beams at the fiber output is connected in a photo-detector. The offset locking technique is based on the frequency-dependent phase shift experienced by the beat note of the two laser frequencies when it propagates through a coaxial cable (86).

Both coherent transmission and phase contrast imaging systems demand being able of locking the laser at detunings which are several unities of the natural width away of the condition of resonance. According to the frequency shifts produced by the AOMs in the two beams of the beating, the frequency of resonance between the Baby Blue laser and the blue transition corresponds to a beat note of approximately 505 MHz. In general, for any value of the baby blue frequency υ_{bb}, the beating signal will have a frequency given by $\Delta\upsilon = \upsilon_{bb} - \upsilon_b$, where υ_b is the frequency of the beam of reference that we use from the main blue laser.

Figure 42 shows the electronic scheme implemented to create the frequency offset locking. The photo-detector used to capture the beat note has 2 GHz of bandwidth, setting a limitation for our locking system of about 1.5 GHz from the resonance condition. Here we use two amplifiers to amplify the beating signal until approximately 16 dBm after being captured by the photo-detector. After that, the signal passes through a Directional Coupler which takes a sample of the input to be used as a monitor when connected to a Spectrum Analyzer. Subsequently, the signal is mixed with the output of a Signal Generator at υ_{SG} and then, the signal with frequency $|\Delta\upsilon - \upsilon_{SG}|$ is filtered by a Low pass filter with cut-off

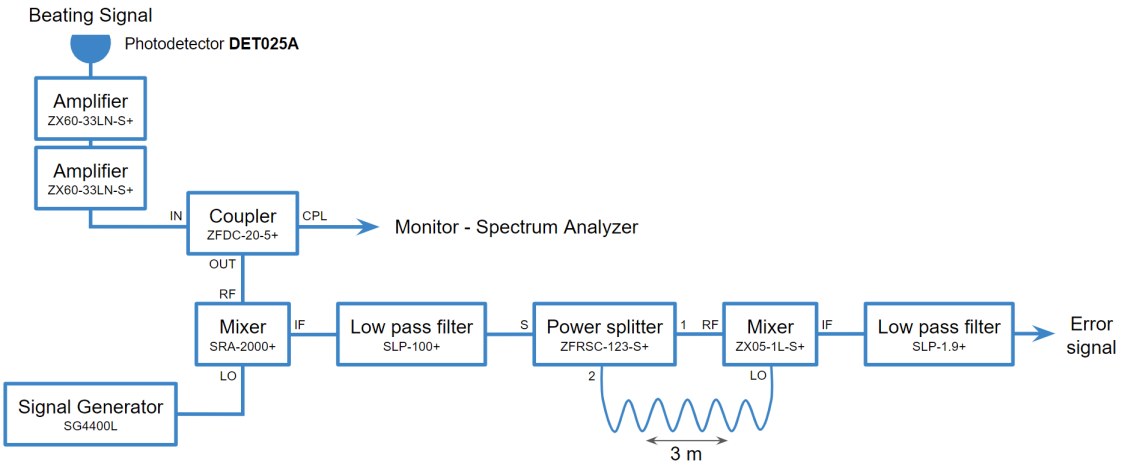

Figure 42 – Scheme of the tunable frequency offset lock. Most of the electronic components are from Mini-Circuits company and the specific information can be found with their respective codes shown in the figure.

Source: By the author.

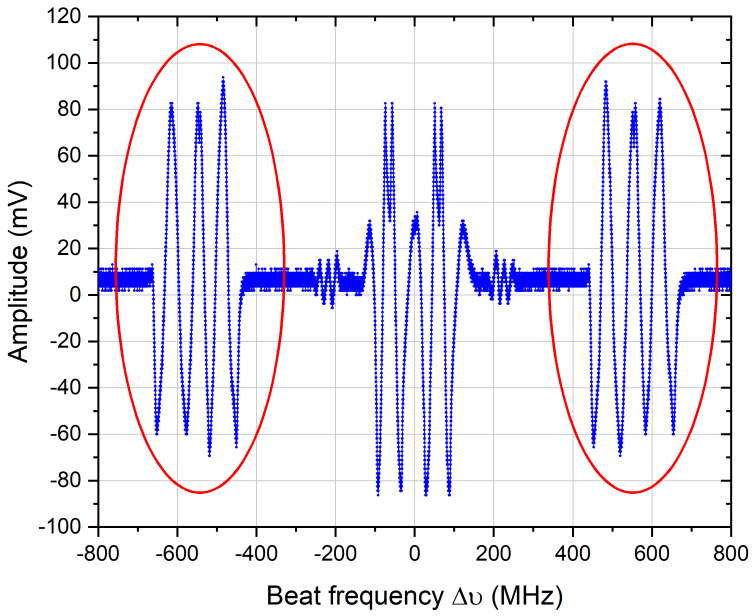

Figure 43 – Output voltage of the frequency offset locking circuit as a function of the beat frequency $\Delta\upsilon$ between the two lasers. The error signal produced by the circuit is represented by the oscillations of the extremes of the graph, inside the red circles. The behavior of the center (close to the zero frequency of the beat note) is a spurious effect that can affect the laser's locking in that specific range of frequency.

Source: By the author.

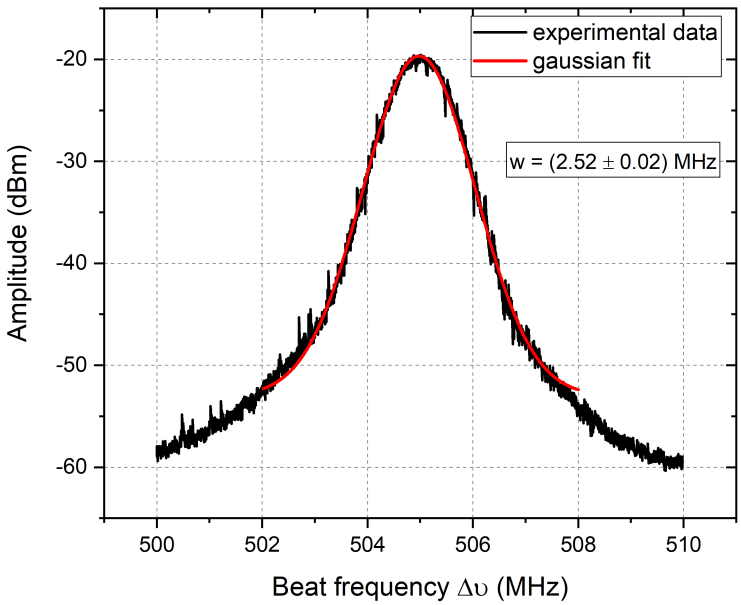

Figure 44 – Beating signal between the principal blue laser and the baby blue laser after the frequency stabilization. The black line represents the experimental curve captured by the Spectrum Analyser and the red line is the Gaussian fit to extract the width of the peak function.

Source: By the author.

frequency of 100 MHz. This last signal is split into two equal parts which are recombined on a mixer, after one part has been delayed by a 3 meters coaxial cable. The mentioned mixer works as a phase detector since the output at twice the frequency is blocked by a low pass filter with a cut-off frequency of 1.9 MHz. The resulting output voltage of the phase detector varies as $\cos\Phi$ where the phase shift Φ introduced by the cable is proportional to the frequency $\Delta\upsilon - \upsilon_{SG}$.

The output signal of the offset locking circuit is shown in figure 43 as a function of the beat frequency. In this graphic, the beat frequency is scanned over more than 1 GHz by varying the frequency of one of the lasers. The oscillatory behavior at the center, near the frequency zero for the beating, is a spurious effect caused by the DC behavior of the mixer that combines the beating signal with the output of the Signal Generator. The oscillations inside the red circles are the actual cosine curve of the offset locking circuit and can be used as error signals for locking the frequency of the baby blue laser. The size of the envelope in the error signal is related with the Low Pass Filter of 100 MHz used after the first mixer.

Finally, the error signal is introduced to a DigiLock in order to create a correction in the current of the laser and lock the frequency with approximately 2.5 MHz of accuracy.

The locking point can be tuned by simply varying the reference frequency of the Signal Generator. At the end, we verified that the implemented locking system allow us to lock the frequency of the Baby Blue laser approximately 900 MHz above the resonance with the atomic transition, and -1400 MHz below the resonance. Also, because of the noise around the zero frequency of the beating signal, we are not able of locking the laser for frequencies between -600 MHz and -400 MHz.

The accuracy of the locking system was estimated by fitting the beating signal once the laser frequency is stabilized. Figure 44 shows the Gaussian fit of the beat note extracted from the Spectrum Analyzer used to monitor the lock frequency. Here, we measured a width of (2.52 ± 0.02) MHz, which indicates an upper bound for the Baby Blue linewidth.

6.1.2 Spectral Filtering

As we saw in the previous chapter, the theoretical coherent transmission spectra showed a very low transmission signal (or the order of 10^{-3}) for high density samples. For this reason, the experimental implementation of these measurements requires a good spectral resolution of the transmission beam and a large signal-to-noise ratio, allowing the detection of low intensity signals by minimizing the background noise.

We used a Fabry-Perot cavity to produce a spectral filtering of the probe beam used for the coherent transmission measurements. The cavity has the function of reducing the high-frequency noise, thus improving the relative amount of light close to the central frequency. This system is shown in the third section of figure 41. The Fabry-Perot, through a constructive interference process, will selectively transmit or reflect certain wavelengths of light while blocking others, resulting in spectral filtering effects.

The mirrors of our Fabry-Perot cavity seems to have a coating with a considerably absorption index that make them unsuitable for a good cavity. This problem give place to a loss of power in every reflection of light within the cavity and, at the Fabry-Perot output, we have a transmission of less than 5% from the power of the incident light.

In order to use the filtered light that comes from the cavity transmission, it is necessary to implement a locking system for this cavity. As the baby blue laser is stabilized, we can use it as a reference of frequency and lock the cavity length in one of the transmission peaks. We first tried to use a Digilock to produce an error signal of the cavity transmission and being able to lock the cavity at the top of a transmission peak, but the signal was too noisy probably due to a bad spectral quality of our laser and the fact that we have a very low transmitted light power. At the end, we used the same transmission signal as an error signal and produced a sideband locking. The transmission signal can be seen on figure 45**a**, where the width is approximately 27 MHz, since the free spectral range is $\Delta_{FSR} = 3$ GHz and the finesse is $\mathcal{F} = 110$ for the 461 nm blue light. In the Digilock, it is possible to change the offset of the signal and lock the cavity in one of the peak sides around the

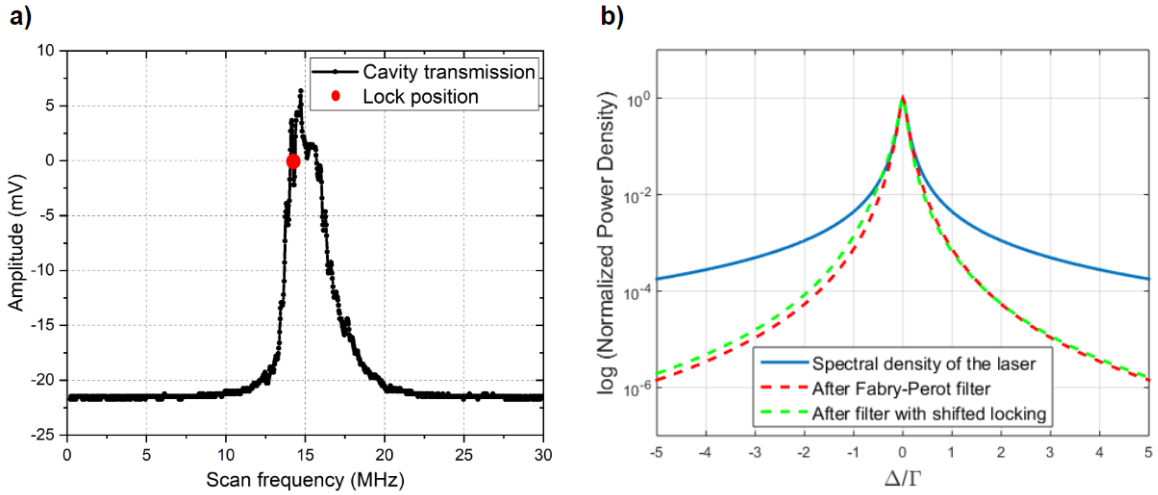

Figure 45 – (a) Signal of Fabry-Perot transmission, taken from the Digilock, used as a signal error to lock the cavity. The red dot represents the position where the cavity is locked. (b) Estimation of the light filtering when using the Fabry-Perot cavity, considering the asymmetry produced by the locking position.

Source: By the author.

offset zero. We usually select the left side of one transmission peak to stabilize the cavity; this position is represented by a red dot in the figure. This sideband locking reduce even more the power at the cavity output, since the lock is not happening at the top of the transmission, but have the advantage of being robust against power fluctuations.

In order to estimate how much the cavity is filtering the incident light, we first made a simulated representation of the spectral density of the Baby Blue laser, considering a linewidth of 1 MHz, as measured in the previous section. This spectral density can be found in the blue line of figure 45**b**, where the plot was made in a logarithmic scale. Considering that the transmission peak behaves like a lorentzian curve with equation $1/(1+4\Delta^2/\Delta_c^2)$ (where $\Delta_c = 27$ MHz is the width of this curve), by doing a convolution of this curve with the spectral density of the laser, we can observe the spectral density of the filtered light (see red dash curve of figure 45**b**). By a visual comparison of the blue and red curves, we already see an improvement of the spectral resolution of the beam, with a clear decreasing of the power density for values with non-zero detunings. For example, considering a detuning equal to the linewidth of the transition $\Gamma = 30$ MHz, the filtered light presents a power 6 times smaller when compare with the non-filtered light.

As the locking position for cavity presents a shift of frequency with respect to the center of the transmission curve, we need to consider this to estimate the real filter that we are producing in our system. Considering a shift of $\Delta_c/3$ in the spectral filtering, we obtained the curve represented with the green dash line of figure 45**b**. It is clear here the appearance of an small asymmetry in the spectral density of the filtered light, however the

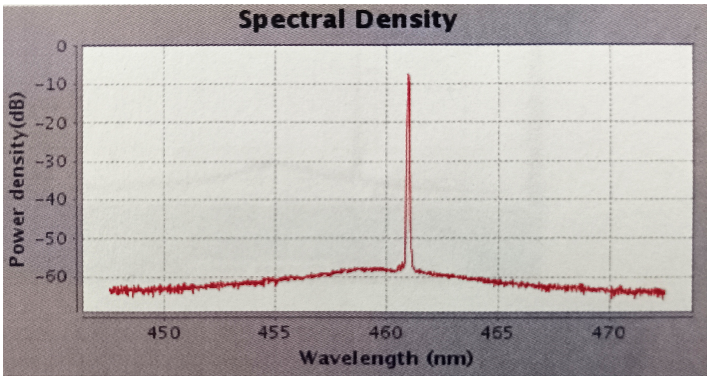

Figure 46 – Real spectral density of the Baby Blue laser.

Source: Adapted from the TOPTICA (87).

filtering is approximately of the same order of the filter produced that we would produce locking the cavity at the peak of the transmission curve.

In figure 46, we can see the spectral density of the Baby Blue, taken from the Toptica data sheet, in our real conditions where the maximum power density is centered in a wavelength of 461 nm. We believe that the main effect of the filter produced by the cavity is to reduce the pedestal below the peak of the maximum gain of the laser. In other words, we can say that main reduction of the power density will be for frequencies far from the resonance condition showed in figure 45**b**, since the pedestal span a frequency range of several THz, which is much bigger than the free spectral range of the cavity. A way to estimate how much of this pedestal is reduced by the spectral filter, can be done by considering the area under the transmission peak after the Fabry-Perot cavity and dividing it by the frequency range over which the cavity exhibits multiple transmission peaks due to interference. As the area under the transmitted lorenztian curve is given by:

$$\int \frac{d\Delta}{1+4\Delta^2/\Delta_c^2} = \frac{\pi\Delta_c}{2} \ , \tag{6.1}$$

and the area between two transmission peaks is given by the free spectral range of the cavity, we obtain a filtering index of

$$filter \approx \frac{\pi\Delta_c/2}{\Delta_{FSR}} = \frac{\pi}{2\mathcal{F}} \approx 0.014 \ . \tag{6.2}$$

Finally, we can say that the reduction of the power density, which is calculated by the inverse of the filtering index, is approximately 70 times less than the non-filtered light.

6.2 Preparation of Coherent Transmission Beam

To measure the transmission spectrum of near-resonant light, we need a $J = 0 \leftrightarrow J = 1$ transition such as ${}^1S_0 \Leftrightarrow {}^1P_1$ (461 nm) or ${}^1S_0 \Leftrightarrow {}^3P_1$ (689 nm). We are going to use

the first one, which is practically closed for short excitation times, so we can consider that no atom will decay to other levels. The choice of the blue transition is motivated by its significantly higher saturation intensity compared to that of the red transition. This allows us to utilize an excitation beam with higher power, resulting in a greater signal when generating coherent transmission spectra using a low-intensity beam. Even if we were to increase the saturation parameter of the incoming beam, to being able of using the red transition, we would place the system in a condition where the scattering rate is larger than the linewidth of the atomic transition. In this situation, a single photon scattering event could be sufficient to shift the atom out of resonance with the incoming beam, causing Doppler broadening of the transition. Summarizing, using the blue transition ${}^1S_0 \Leftrightarrow {}^1P_1$ will provide more signal and would not be subjected to Doppler broadening.

The Baby Blue laser beam is coupled on a Polarization Maintaining Singlemode Fiber (see figure 47) and, at the output of this fiber, we have a fiber collimator from Schäfter + Kirchhoff (60FC-L-4-M20L-01) with focal length 20 mm that allow us to obtain a large beam diameter. We performed the *knife-edge technique* to measure the size of the collimated beam and we obtained a waist of $w_0 = 2.4$ mm. With an achromatic lens of 50 mm, we decrease the waist of the beam to be smaller than the atomic cloud size at the focus position. The relation between the focal length f and the beam waist at the focus of the lens w_f is given by $w_f = \lambda f/\pi w_0$, so we should obtain a waist of 3.06 μm. We experimentally confirmed that it is possible to obtain a very small waist of less than 4 μm, but the precise measurement of the beam size is described in the next section. Since the radius of the atomic cloud is slightly smaller than 10 μm, in the mentioned conditions we guarantee the interaction of the beam with an approximately homogeneous region of the cloud in the transverse directions. On the other hand, the waist of the beam needs to be significantly larger than the wavelength λ so the paraxial approximation is valid.

The incident beam has an angle of approximately 25 degrees with respect to the vertical direction. This angle was unavoidable in our experimental conditions but the transverse size of 0.5 inches for the 50 mm lens allowed us to reduce this angle and align the coherent transmission beam without blocking any other light beam of the experiment, such as the MOTs beams.

After the interaction of the beam with the atoms we use another lens of 75 mm to collect the transmitted beam that, with the help of a telescope, is coupled into another singlemode fiber connected to a photodetector. With this configuration, we guarantee the measurement of the coherent transmission (49, 56). The photodetector that we use is a avalanche photodiode (APD) from ID Quantique, visible single-photon detector with great timing resolution of only 40 ps and low dead time of 45 ns. This APD, which is a module from the ID100 series, is able to detect weak optical signals down to the single photon level and has excellent timing stability up to count rates of 20 MHz. The ADP is connected to a

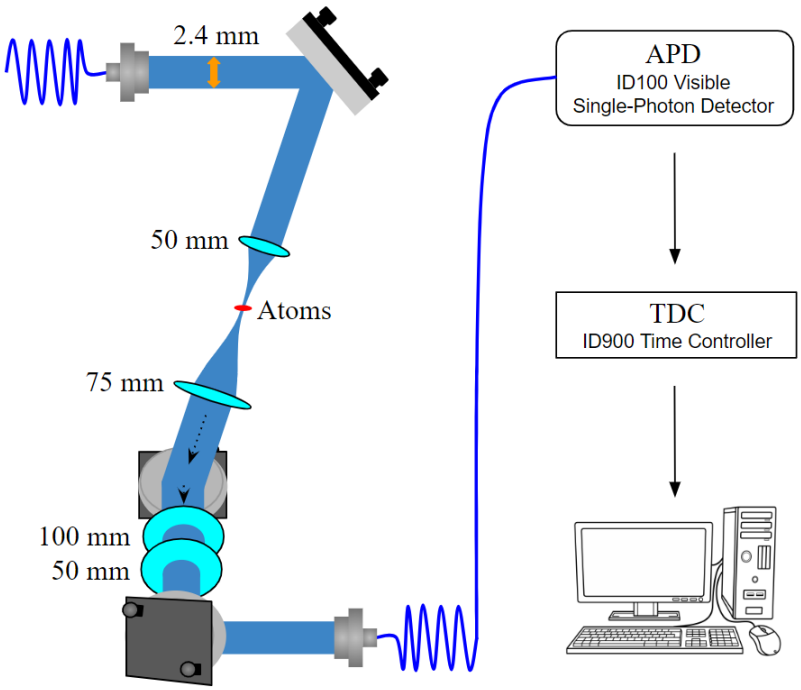

Figure 47 – Setup for coherent transmission measurements: The light beam is focused at the center of the atomic cloud and the transmission is coupled in a singlemode fiber. This collection fiber is connected to as avalanche photodiode (APD) and then to a time-to-digital converter (TDC) which sends the information to a computer.

Source: By the author.

time-to-digital converter (TDC), also from ID Quantique, which is a device for recognizing events and providing a digital representation of the time they occurred. Specifically, our TDC (ID900 Time Controller) output the time of arrival for each incoming light pulse or each incoming photon. Finally, the TDC is connected to a computer in order to process the recorded data.

We measured the power efficiency of our system to find the relation between the light power that hits the atomic cloud and the light that arrives at the photodetector. We have some lost of power while the light passes through the optics, but the main lost is in the coupling of the collection fiber. This problem is because the entrance of light in the APD has a PC (Physical Contact) connection, so we used a PC fiber to collect the light transmitted by the atoms. However, we did not have a PC collimator available in our lab and ended up using an APC (Angled Physical Contact) one. Then, the coupling of the light when using the APC collimator and the PC fiber was not so good, and the collected light has a power of 19% of the light reaching the atoms.

For the coherent transmission measurements, we send an incoming light pulse to the dense atomic cloud and record the transmitted light during the time of the pulse. We

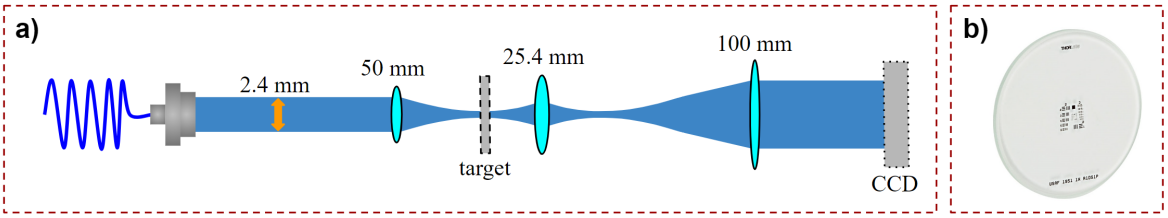

Figure 48 – Setup for the measurement of the coherent transmission beam waist: (a) There is a resolution target at the focus of the beam and it is produced an image of the plane of the target with magnification 4. (b) Details of the transparent target with the pattern imprinted at the center.

Source: By the author.

use two channels of the TDC: a first one to detect the time for the beginning of the light pulse and a second one to detect the time for the arrival of each transmitted photon. With a MatLab program, we count the number of detected photons after the starting of each pulse. The duration time of the light pulse needs to be characterize and its characterization will be shown later in this same chapter.

6.2.1 Characterization of the Beam

Measuring the size of the light beam it is not usually a difficult experimental procedure if we can use a camera with a spatial resolution considerably smaller than the beam size. Unfortunately, this was not our case since we know that the coherent transmission beam has approximately 3 μm and the available camera had a resolution of 3.79 μm per pixel. We had to implement a new system to obtain the waist of the beam by using a resolution target.

For this measurement, we mounted in another place of the optical table, the configuration shown in figure 48. Here, we use the same collimator and the 50 mm lens of the coherent transmission setup. At the focal plane of the lens, we put a resolution target (1951 USAF Resolution Test Target from ThorLabs) which is in a translation stage that allow us to scan its transverse position. With the help of the next two lenses, we image the plane of the target at the CCD camera with magnification 4. The procedure consisted in keeping the beam focused on the target and scan the transverse position of the target in order to capture the transmission of the beam between the black lines. The experimental section of figure 49 shows with a red line the direction that we follow to scan the target. We produce six images corresponding to the different separations between the lines of the target. The red dot represents a position where the beam does not interact with the black lines, so we can make an image in this condition and use it to normalize the transmission.

The separation between the black lines of the target can be extracted from its

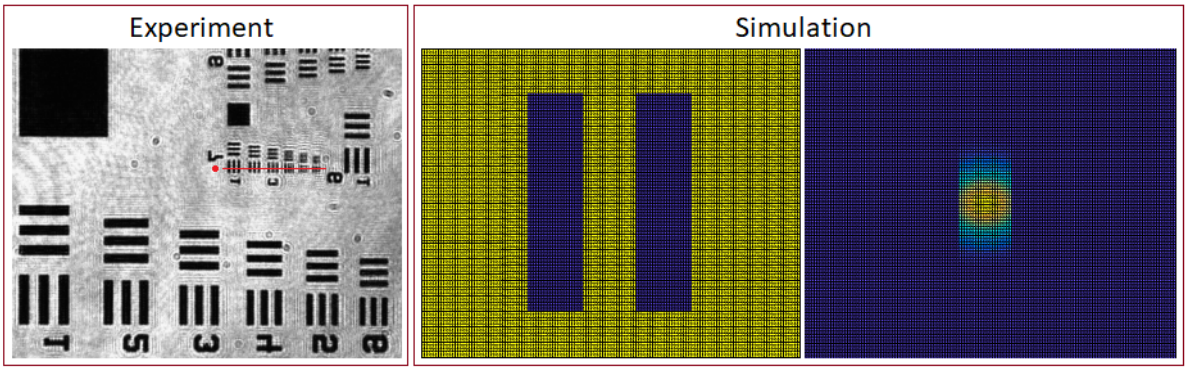

Figure 49 – Experiment and simulation performed to measure the size of the coherent transmission beam.

Source: By the author.

ThorLabs manual: 7.8 μm, 6.9 μm, 6.2 μm, 5.5 μm, 4.9 μm and 4.3 μm (from the first black lines closer to the red dot until the end of the red line). With this information, we can simulate a mask representing two black lines blocking part of the Gaussian beam that passes between them (see the simulation section of figure 49). This simulation relates the waist of the beam with the normalized transmitted light while passing through the blocking lines considering the six different separations. In order to estimate the waist of the beam, the simulation considers beams with different sizes and make a comparison with the experimental results, detecting the value with the minimum mean square error. At the end, we obtained a value of (3.28 ± 0.42) μm for the waist of the coherent transmission beam.

6.2.2 Alignment of the Beam

The alignment of the coherent transmission beam on the crossed ODT was a difficult process due to the small size of the cloud and the beam itself. In order to observe the effect of the beam on the cloud, we implemented an experimental sequence that creates a pulse of the transmission beam during the imaging of the cloud by the Absorption Imaging technique. With a high enough power of the transmission beam, it will saturate the image in regions where the atoms are present. After observing the first effects of the beam, we corrected the position of the focusing lens until having the smallest hole produced by the beam in the middle of the ODT. Figure 50 shows the AI of the crossed ODT without and with the presence of the coherent transmission beam aligned at the center of the atomic ensemble.

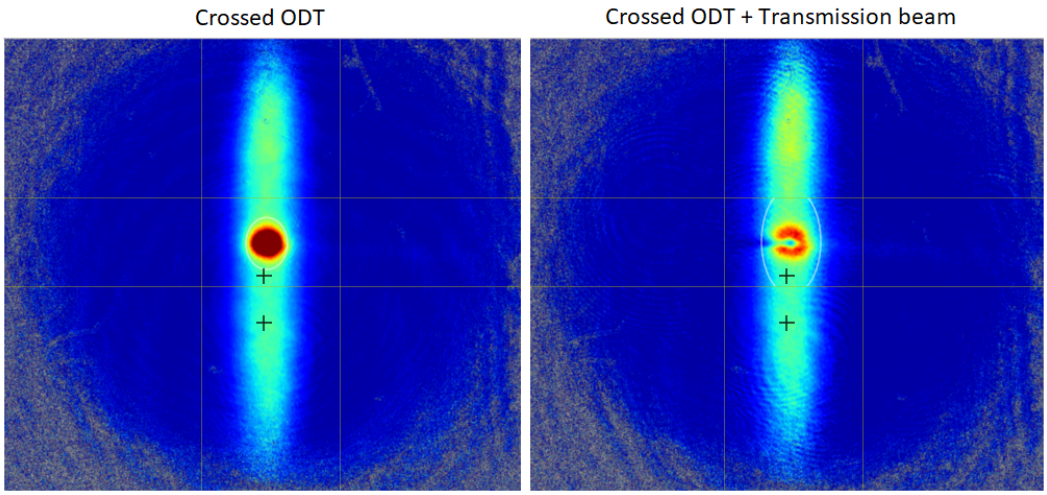

Figure 50 – Absorption imaging of the crossed ODT without and with the superposition of the coherent transmission beam.

Source: By the author.

6.3 Coherent Transmission Measurements

Before starting the coherent transmission measurements in the dense regime, we made some characterizations of our experimental system using a dilute cloud. These characterization consisted in determining the duration time of the exciting light pulse, in centering the position of the beam withing the cloud, and observe the first coherent transmission spectra for a low density cloud.

6.3.1 First Characterizations

In order to characterize the duration time for the coherent transmission light pulse, we considered a cloud with $b_0 = 3$. We performed two different measurements of transmission: considering the atomic cloud and without the presence of the atoms. The measurements without atoms were used only for normalization of the counting rate of photons.

This measurement, and most part of the coherent transmission measurements, were done using a power of 133 pW of the light beam at the atomic cloud position, which corresponds to a saturation parameter of $s = 4 \times 10^{-3}$. Considering the loss of light power from the atoms position until the APD, the mentioned power of 133 pW produces a counting rate of 5 MHz.

For processing this set of measurements, we selected different times for the integration of the light pulse, counting the number of photons for each time interval and normalizing with the corresponding time interval in the experiment without atoms. The normalized counting rate as a function of the light pulse time, can be found in figure 51.

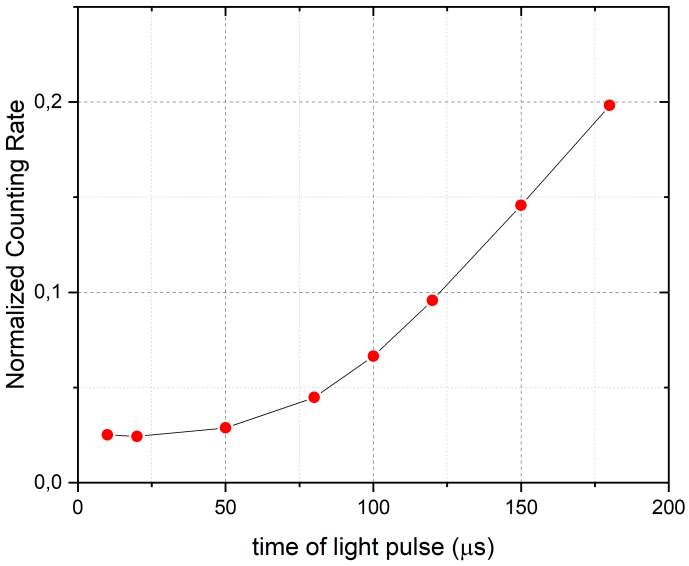

Figure 51 – Measurements for the characterization of the duration time for the transmission light pulse.

Source: By the author.

Here, we see as the counting rate remains constant at the beginning of the curve and then start to increase in an exponential way. The increasing is related to the heating of the cloud produced by the incident beam, which also decreases the density of the cloud allowing for higher transmission of the beam. The results show that the time of the light pulse should be around 50 μs.

The next characterization consisted in scanning the frequency of the incident beam, in order to produce an spectrum of the dilute cloud. We considered similar conditions for the cloud and the beam described above, e.i. a cloud with optical depth $b_0 = 3.2$ and a power of the beam corresponding to a saturation parameter of $s = 4 \times 10^{-3}$. The results for this measurement can be seen in figure 52, where we plotted the normalized counting rate using also a logarithmic scale that allow us to see the behavior of the spectrum with more details. The detuning in this curve is normalized by the linewidth of the atomic transition $\Gamma = 30$ MHz.

The expected result in the dilute regime is an spectral curve centered at the resonance condition and presenting a symmetrical behavior. This spectrum can be use to detect the exact resonance condition and correct the frequency shift in this spectrum and the next measurements that we will produce in the dense regime. With a lorentzian fit, we can extract the full width half maximum (FWHM) and the depth of the curve, which give information about Γ and b_0, respectively. The obtained values were: FWHM =

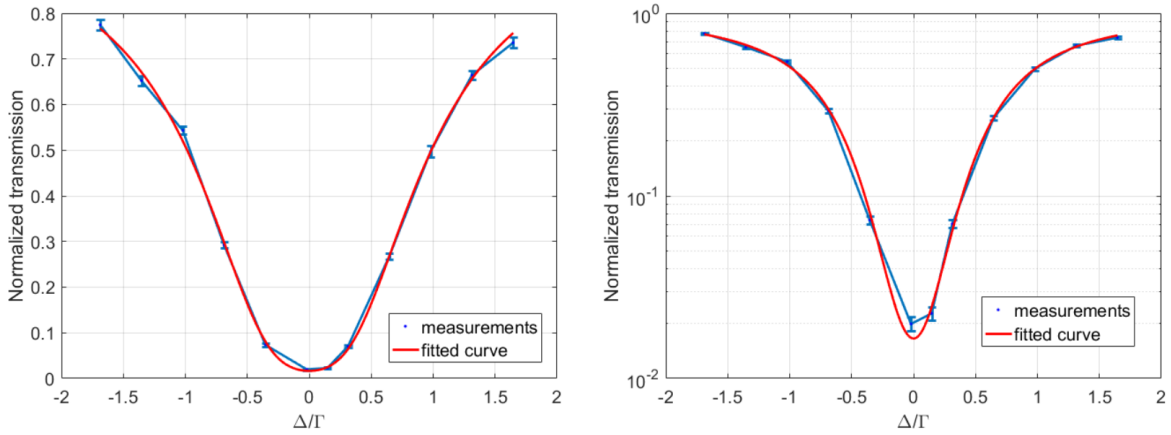

Figure 52 – Coherent transmission spectrum for a dilute cloud of $b_0 = 3.2$. Both graphs represent the same set of measurements but the right one is in a logarithmic scale. The red line of the left graph represents a lorentzian fit.

Source: By the author.

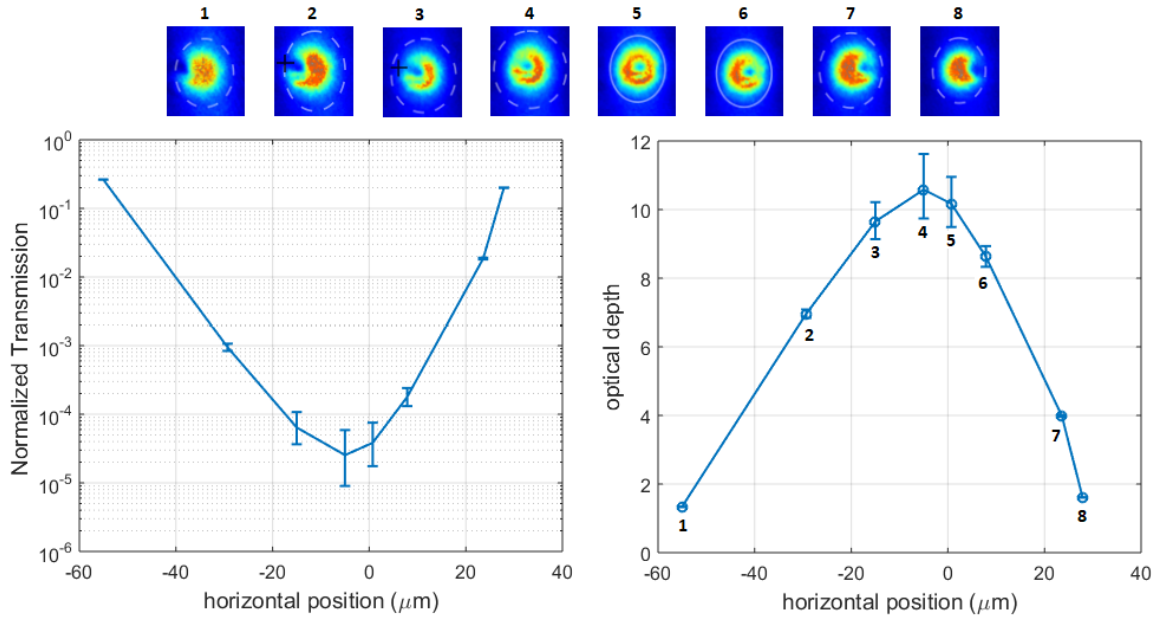

Figure 53 – Transmission of the atomic cloud with a resonant incident beam, while scanning the horizontal position of the beam across the vertical center of the cloud. The considered positions for the beam can be seen at the top of the image.

Source: By the author.

$(0.89 \pm 0.09) \times \Gamma$ and $b_0 = 4.1 \pm 0.6$. The value for Γ was slightly lower than expected, but this could be related to the resolution with which the detuning was scanned, and the fact that we did not complete the curve at the extremes of the spectrum. The value for b_0 was slightly higher than 3.2, which can be related to two different things: a bad resolution of the curve around the resonance (which is very clear in the spectrum with logarithmic scale), and the angle between the coherent transmission beam and the vertical direction, which makes the beam interact with a larger region of the atomic ensemble. We estimated the correction of the optical depth, according to the angle, and the real value should be approximately 10% higher than the measured one.

A final characterization, using a dilute cloud, was motivated by the existing angle between the coherent transmission beam and the vertical direction in the experimental setup of figure 47. Because of this angle, the observed hole produced by the beam at the cloud (presented in figure 50), it is a projection of the real effect of the beam in the imaging plane. Then, we were not sure in which condition the incident beam is actually centered at the cloud. In order to find the right alignment condition, we scanned the horizontal position of the beam, following the vertical center of the ODT. For this graphs, we set the position zero at the center of the crossed ODT (taken from the Gaussian fit of the cloud), then the other positions where calculated considering the pixel size and magnification of our imaging system. At the end, the experimental results of this measurement (shown in figure 53), indicates that the minimum of transmission is not where the hole produced by the beam is at the center of the cloud when observed by AI. So, the best alignment condition is indeed a few µm to the left of this centered hole, where the optical depth is also higher. The graph of the optical depth as a function of the horizontal position can be found at the right graph of figure 53. Here, we also see that even observing a slightly different b_0 around the center of the atomic cloud, this region is approximately homogeneous as we considered in the simulations described in the previous section.

6.3.2 Measurements in the Dense Regime

For the first set of measurements in the dense regime, we used a cloud with the highest optical density that we could obtain. Unfortunately, at that time we had not finished the characterizations of the phase contrast imaging system and we were not sure about the quantitative information of our atomic cloud. However, we believe that this cloud used for the coherent transmission measurements in the dense regime, had a higher density that the final ODT described at the end of the Chapter 4. This is because at some point, during the dense regime measurements, we had to refill the oven and recover the vacuum of our experimental system. After that, we were not able of reobtaining the same number of atoms that we had before. In addition, we know that the power of the infrared laser (used to create our crossed ODT) is lower now, due to the gradual loss of power that we have been observing during the last months.

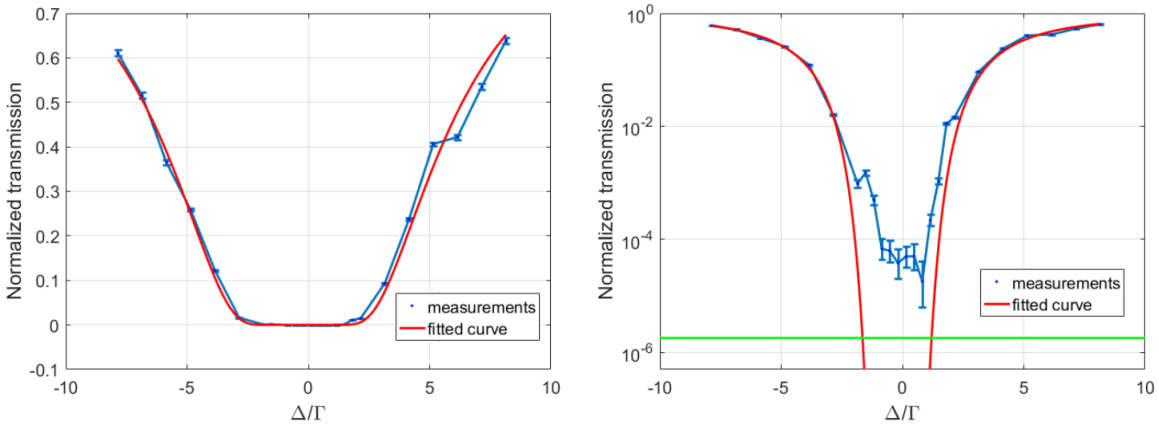

Figure 54 – Coherent transmission spectrum for a dense cloud. Both graphs represent the same set of measurements but the right one is in a logarithmic scale. The red line of the left graph represents a lorentzian fit, using $\Gamma = 1$ as a fixed parameter. The green line represents the dark count of our APD.

Source: By the author.

In order to produce the first transmission spectra using a dense cloud, we had to take lots of measurements, averaging over approximately 500 realizations for detunings close to the resonance condition, and approximately 150 realizations for larger detunings. Each realization consisted in a light pulse of 100 μs, where we counted the number of photons detected during the first 50 μs. This spectrum can be seen in figure 54, in two different scales: linear and logarithmic. The obtained spectrum shows an asymmetry with respect to the resonance, which is expected in the dense regime. Nevertheless, we did not observe the behavior predicted by the simulations.

With a Loretzian curve, we fitted the wings of the spectrum fixing the linewidth, which was characterized using the dilute regime spectrum, i.e we considered $\Gamma = 1$. The fitting gave an optical depth of $b_0 = 120.4 \pm 4.9$, suggesting a very high density of the cloud, and a red shift of $-(0.23 \pm 0.08) \times \Gamma$. The saturation of the curve, and also the red shift, are signatures of density effects in the atomic cloud.

In order to show that the saturation is not a technical limitation of our detection system, we included the dark count of the APD in the graph (green line in figure 54). The dark count was measured by counting the number of photons arriving to the APD while running many times the experimental sequence in the same condition that the measurements were taken, but with the coherent transmission beam off. Then, collecting all arrival events and dividing it by the time, we measured a dark count of 9 Hz. This value represents a transmission of 1.8×10^{-6} when normalized by the counting rate of the incident light used to produce the spectra, which is 5 MHz.

After these results in the dense regime, we still had some questions about what

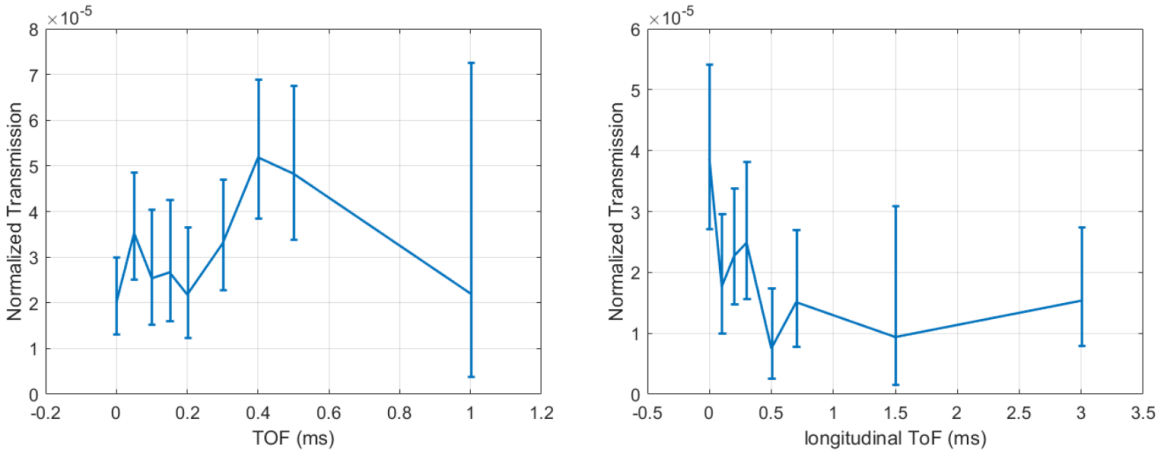

Figure 55 – Light transmission as a function of the expansion time of the cloud in two different conditions: (left) global time-of-flight, and (right) longitudinal time-of-flight

Source: By the author.

determines the saturation of the spectrum around the resonance condition. One of the hypothesis was the possibility of a stray light going to the photodetector. We though that maybe the wings of the beam was being transmitted without interacting with the cloud, because the transverse size of the ODT is not higher enough than the waist of the incident beam. In order to test this specific questioning, we developed some new measurements consisting in applying different time-of-flights to let the atomic cloud expand. Then, we measured the transmission of the light as a function of the expansion time. The experimental results can be seen at the left graph of figure 55. We did not know exactly the temperature of the cloud that we used for these measurements, but we believe that was or the order of 2 μK, so we were expecting a fast expansion of the ODT. We observed that the transmission remained almost constant during this set of measurements.

In the case were the wings of the beam would be passing through the borders of our atomic cloud, a transverse expansion of the cloud would change this situation and, as a consequence, we should have a decreasing of the transmission. Even when the error bars of these measurements are too big, the fact that we did not observed a dramatic change in the transmitted signal, made us eliminate this possibility.

Another test that we made, consisted in letting the cloud expanding while applying a special time-of-flight (ToF). We liberated the cloud turning off only the horizontal beam of the ODT, so the expansion was happening only in the vertical direction (longitudinal direction according to the direction of propagation of the excitation beam). In these conditions, we would preserve the optical depth of the sample but we would have a decreasing of the spatial density. Producing this longitudinal ToF, the atomic system

would transition from the dense to the dilute regime, and a decrease in the transmission is expected. The results of this experiment can be seen at the right graph of figure 55. Here, we observed a slight decrease in the transmission signal, but not as fast as we were expecting, and also the error bars are too big to detect any clear behavior of this curve. To be more precise, we would need to make simulations of this specific situation in order to confirm quantitatively the expected behavior for the measurements.

Unfortunately, all results that we have so far in the dense regime, even where they probe the possibility of the presence of density effects, are very preliminary. Maybe we just need to make more measurements to reduce the error and completely solve the structure of the coherent transmission spectra, but we still have some hypothesis that we need to verify. First, we should increase the intensity of the beam in order to have more output signal and improve the detection rate. For this, we could use a saturation parameter of $s = 1$, that even when we might think that violates the linear regime, as the optical depth of the cloud is very large, most part of the light would be absorbed by the first layers of atoms and the rest of the atoms would interact with a low intensity beam.

The final hypothesis relies in the recent simulations that was mentioned at the end of Chapter 5. We believe that our detection can be affected by incoherent transmission going to the forward direction. In order to understand the influence of this incoherent transmission, we can filter the polarization of the transmission light, separating parallel and perpendicular polarization states, and measure both signals. All signal measured with a polarization perpendicular to the one of the incident light, will be purely incoherent. Then, assuming that the incoherent light is completely unpolarized, we would have a measurement of the incoherent part and we could subtract from the transmission in the parallel polarization, to try to find the coherent part.

7 CONCLUSIONS

A system for obtaining a dense atomic cloud trapped in a crossed Optical Dipole Trap, suited for studying collective effects in the high density regime, was implemented. In the characterizations of our atomic cloud, we faced some problems to obtain the quantitative information of our ensemble, due to the saturation of the Absorption Imaging when the optical depth of the sample is larger than 4. In order to circumvent this situation, and being able to measure our cloud *in situ*, we implemented a Phase Contrast Imaging system that allows the characterization of samples with optical depths of the order of 100. This new imaging technique was crucial for the final optimizations of our dense cloud.

As part of the optimizations of our atomic cloud, we implemented an extra stage of cooling after the atoms being transferred to the Optical Dipole Trap. This stage of cooling consisted in an Optical Molasses using the red transitions of ^{88}Sr. The improvement in our cloud, when applying the Optical Molasses, was mainly due to the cooling of the atoms that remained in the more shallow part of our trap, allowing them to move to the deep potential at the bottom of our crossed ODT. At the end of the optimizations, we obtained a pancake shape cloud with approximately 370 000 atoms, an optical depth of 50 and spatial density (in unities of $1/\lambda^3$) of $\rho\lambda^3 = 4.4$.

Simulations of coherent transmission spectra, using the equations of the Coupled Dipole Model, were performed. The theoretical results showed the presence of density effects through a saturation and splitting of the spectral curves. As these simulations were done in conditions that model characteristics similar to those we have in the experiment, we should then observe similar experimental spectra. The simulations were also relevant to pointing out the difficulties of producing these kind of measurements. As we observed theoretical spectra with large width and low transmission values (of less than 10^{-3}), in order to perform the coherent transmission measurements, we found the need of producing an spectral filtering of the incoming beam, and also of implementing a tunable locking system that allow us to scan the frequency for a range of more than $10 \times \Gamma$ around the condition of resonance. The spectral filter was done by using a Fabry-Perot cavity with a finesse of $\mathcal{F} = 110$, and we estimated a reduction of the noise of 70 times less than the non-filtered light.

A setup for coherent transmission measurements was implemented, introducing the necessary equipment to perform these experiments. Several characterizations were made to describe our beam and its interaction with the sample. The beam has a waist of (3.28 ± 0.42) μm, which is approximately 3 times smaller that the transverse size of the ODT (~ 10 μm), so it fulfills the premise of interacting with a "homogeneous" region of the cloud. The measured spectrum for a low density cloud, showed the expected behavior

for its density regime: width equal to the natural linewidth of the atomic transition, and a depth corresponding to the optical depth at low spatial density. The measured spectrum for a high density cloud, also showed a behavior that might be related to the presence of density effects in our atomic ensemble: saturation plus asymmetry of the curve. However, we were not able to completely solve the structure of the measured spectrum and the shape was different to that expected according to the simulations. Some hypothesis of the divergences observed in the experimental results, are discussed in the main text of this thesis, but we are still investigating the possibilities. So far, we just have some preliminary results.

7.1 Next Steps

7.1.1 Continuation of Coherent Transmission Measurements

At this moment, we are performing more measurements of the coherent transmission by the dense cloud, but we made some small modifications of our experimental system, that can be very relevant for our future results: we increased the intensity of the excitation beam until the saturation parameter $s = 1$, and we also installed a half-wave plate and a polarizing beam splitter before the collection fiber in order to separately measure the transmitted light with both parallel and perpendicular polarization states. This last modification should help us to understand the influence of possible incoherent light that could be transmitted in the forward direction.

7.1.2 Implementation of an Optical Accordion

In parallel with these measurements, we are also implementing an extra confinement of the cloud in the longitudinal direction. This is because our crossed ODT is hotter then we thought and this leads to a greater expansion in the z axis. An atomic cloud too expanded in the longitudinal direction can have a large optical depth, but not necessary a high spatial density. Then, to continue the studies of collective effects in the dense atomic regime, would be convenient to compress more the cloud.

The extra compression of the atomic ensemble is going to be done by producing another optical dipole trap created by the interference pattern of two green laser beams. The inspiration was taken from the article (88), where it is reported the realization of an optical accordion creating a lattice potential with a spacing that can be dynamically tuned. In this way, the atoms can be load into a single node of the lattice when the spacing between the lattice sites is large and then to reach a strong confinement while the spacing is decreased. In our system, we will not implement an dynamic accordion, but we want to transfer the atoms from the current implemented trap to a new trap created at the central maximum of the interference pattern between two beams that will access to the science chamber through a horizontal window. This implementation is part of the master project

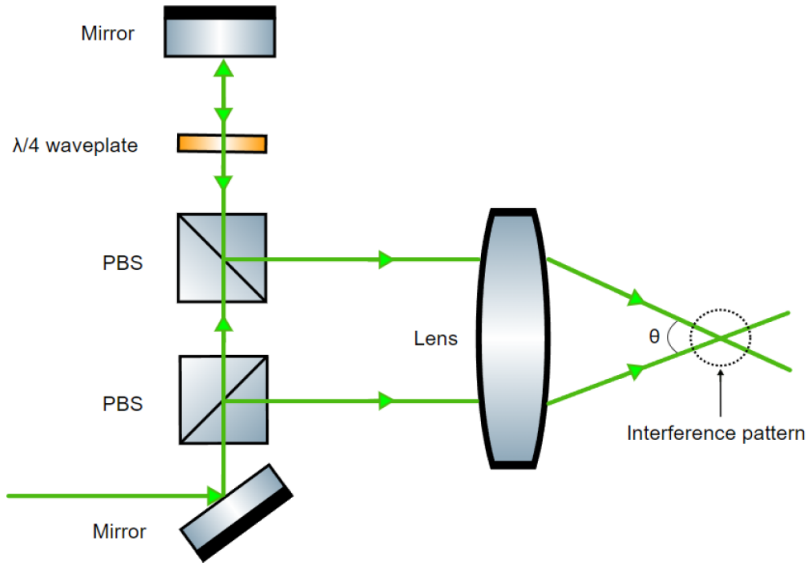

Figure 56 – Experimental setup for the implementation of an optical accordion.

Source: Adapted from MARTINS (89).

of one of the students of the lab (89), and the set up of the system can be seen at figure 56.

When we showed the scheme of the optical table for the green laser, back in Chapter 3, we mentioned that one of the beams of the green laser was going to be used with the purpose of producing an optical accordion trap. This beam, with 497 nm of wavelength, will be divided by the use of two polarizing beam splitters, producing two beams that propagates parallel to the same direction. Finally, these beams will cross at the focal plane of a lens, producing the interference pattern at the position of the atomic cloud. Some calculations, considering the parameters of the experimental system, indicates that with the accordion, we should reduce the longitudinal size of our pancake-shape cloud at least in a factor of 2.

REFERENCES

1 COHEN-TANNOUDJI, C.; DUPONT-ROC, J.; GRYNBERG, G. **Atom-photon interactions**: basic processes and applications. New York: Wiley-VCH, 1998. (Wiley Science Paperback Series). ISBN 0471293369.

2 ARIMONDO, E. Coherent population trapping in laser spectroscopy. **Progress in Optics**, v. 35, p. 257–354, 1996. DOI: 10.1016/S0079-6638(08)70531-6.

3 GUERIN, W.; ROUABAH, M.; KAISER, R. Light interacting with atomic ensembles: collective, cooperative and mesoscopic effects. **Journal of Modern Optics**, v. 64, n. 9, p. 895–907, 2017. DOI: 10.1080/09500340.2016.1215564.

4 DICKE, R. H. Coherence in spontaneous radiation processes. **Physical Review**, v. 93, n. 1, p. 99–110, 1954.

5 CONNERADE, J. P. Cooperative effects in atomic physics. **Advances in Atomic, Molecular, and Optical Physics**, v. 29, p. 325–367, 1991. DOI: 10.1016/S1049-250X(08)60142-1.

6 BIENAIME, T. *et al.* Interplay between radiation pressure force and scattered light intensity in the cooperative scattering by cold atoms. **Journal of Modern Optics**, v. 61, n. 1, p. 18–24, 2014. DOI: 10.1080/09500340.2013.829264.

7 GUERIN, W.; ARAUJO, M. O.; KAISER, R. Subradiance in a large cloud of cold atoms. **Physical Review Letters**, v. 116, n. 2, p. 083601, 2016. DOI: 10.1103/PhysRevLett.116.083601.

8 ARAUJO, M. O. *et al.* Superradiance in a large and dilute cloud of cold atoms in the linear-optics regime. **Physical Review Letters**, v. 117, p. 073002, 2016. DOI: 10.1103/PhysRevLett.117.073002.

9 ARAUJO, M. O.; GUERIN, W.; KAISER, R. Decay dynamics in the coupled-dipole model. **Journal of Modern Optics**, v. 65, n. 9, p. 1345–1354, 2017. DOI: 10.1080/09500340.2017.1380856.

10 BIENAIME, T.; PIOVELLA, N.; KAISER, R. Controlled dicke subradiance from a large cloud of two-level systems. **Physical Review Letters**, v. 108, p. 123602, 2012. DOI: 10.1103/PhysRevLett.108.123602.

11 ROOF, S. J.; KEMP, K. J.; HAVEY, M. D. Observation of single-photon superradiance and the cooperative lamb shift in an extended sample of cold atoms. **Physical Review Letters**, v. 117, p. 073003, 2016. DOI: 10.1103/PhysRevLett.117.073003.

12 RIBEIRO, S. *et al.* Collective effects in the photon statistics of thermal atomic ensembles. **Physical Review A**, v. 104, n. 1, p. 013719, 2021. DOI: 10.1103/PhysRevA.104.013719.

13 GARTTNER, M. *et al.* Collective excitation of rydberg-atom ensembles beyond the superatom model. **Physical Review Letters**, v. 113, n. 23, p. 233002, 2014. DOI: 10.1103/PhysRevLett.113.233002.

14 KUMLIN, J. P. **Collective effects of light-matter interactions in Rydberg superatoms**. 2021. Thesis (Doctor in Science) — Institut für Theoretische Physik III, Universität Stuttgart, Stuttgart, 2021. Available at: https://elib.uni-stuttgart.de/bitstream/11682/11999/1/PhD_Thesis_Jan_Kumlin_final_online_a4_v1.pdf. Accessible at: 17 nov. 2023.

15 DOMOKOS, P.; RITSCH, H. Collective cooling and self-organization of atoms in a cavity. **Physical Review Letters**, v. 89, n. 25, p. 253003, 2002. DOI: 10.1103/PhysRevLett.89.253003.

16 PHILLIPS, W. D.; METCALF, H. Laser deceleration of an atomic beam. **Physical Review Letters**, v. 48, p. 596, 1982. DOI: 10.1103/PhysRevLett.48.596.

17 CHU, S. *et al.* Three-dimensional viscous confinement and cooling of atoms by resonance radiation pressure. **Physical Review Letters**, v. 55, p. 48, 1985. DOI: 10.1103/PhysRevLett.55.48.

18 DALIBARD, J.; COHEN-TANNOUDJI, C. Dressed-atom approach to atomic motion in laser light: the dipole force revisited. **Journal of the Optical Society of America B**, v. 2, n. 11, p. 1707–1720, 1985. DOI: 10.1364/JOSAB.2.001707.

19 RAAB, E. L. *et al.* Trapping of neutral sodium atoms with radiation pressure. **Physical Review Letters**, v. 59, p. 2631, 1987. DOI: 10.1103/PhysRevLett.59.2631.

20 SKIPETROV, S. E.; SOKOLOV, I. M. Ioffe-regel criterion for anderson localization in the model of resonant point scatterers. **Physical Review B**, v. 98, p. 064207, 2018. DOI: 10.1103/PhysRevB.98.064207.

21 SKIPETROV, S. E. Finite-size scaling analysis of localization transition for scalar waves in a three-dimensional ensemble of resonant point scatterers. **Physical Review B**, v. 94, p. 064202, 2016. DOI: 10.1103/PhysRevB.94.064202.

22 ECONOMOU, E. N.; SOUKOULIS, C. M.; ZDETSIS, A. D. Localized states in disordered systems as bound states in potential wells. **Physical Review B**, v. 30, p. 1686, 1984. DOI: 10.1103/PhysRevB.30.1686.

23 JOHN, S. Electromagnetic absorption in a disordered medium near a photon mobility edge. **Physical Review Letters**, v. 53, p. 2169, 1984. DOI: 10.1103/PhysRevLett.53.2169.

24 TIGGELEN, B. A. van *et al.* Effect of resonant scattering on localization of waves. **Europhysics Letters**, v. 15, n. 6, p. 535–540, 1991. DOI: 10.1209/0295-5075/15/5/011.

25 TUCHIN, V. V. **Tissue Optics**: Light scattering methods and instruments for medical diagnostics. Washington: SPIE Press, 2015. ISBN 9781628415179.

26 CROSIGNANI, V. *et al.* Deep tissue fluorescence imaging and in vivo biological applications. **Journal of Biomedical Optics**, v. 17, p. 116023, 2012. DOI: 10.1117/1.JBO.17.11.116023.

27 ZHANG, H.; LIU, K.-K. Optical tweezers for single cells. **Journal of the Royal Society Interface**, v. 5, p. 671–690, 2008. DOI: 10.1098/rsif.2008.0052.

28 MONSHOUWER, R. *et al.* Superradiance and exciton delocalization in bacterial photosynthetic light-harvesting systems. **The Journal of Physical Chemistry B**, v. 101, n. 37, p. 7241–7248, 1997. DOI: 10.1021/jp963377t.

29 JULSGAARD, B. *et al.* Experimental demonstration of quantum memory for light. **Nature**, v. 432, p. 482 – 486, 2004. DOI: 10.1038/nature03064.

30 GORSHKOV, A. V. *et al.* Photon storage in λ-type optically dense atomic media. ii. free-space model. **Physical Review A**, v. 76, p. 033805, 2007. DOI: 10.1103/PhysRevA.76.033805.

31 LI, W.; ISLAM, P.; WINDPASSINGER, P. Controlled transport of stored light. **Physical Review Letters**, v. 125, p. 150501, 2020. DOI: 10.1103/PhysRevLett.125.150501.

32 LVOVSKY, A. I.; SANDERS, B. C.; TITTEL, W. Optical quantum memory. **Nature Photonics**, v. 3, p. 706 – 714, 2009. DOI: 10.48550/arXiv.1002.4659.

33 PELLEGRINO, J. *et al.* Observation of suppression of light scattering induced by dipole-dipole interactions in a cold-atom ensemble. **Physical Review Letters**, v. 113, p. 133602, 2014. DOI: 10.1103/PhysRevLett.113.1336026.

34 CORMAN, L. *et al.* Transmission of near-resonant light through a dense slab of cold atoms. **Physical Review A**, v. 96, n. 11, p. 053629, 2017. DOI: 10.1103/PhysRevA.96.053629.

35 KAISER, R.; WESTBROOK, C.; DAVID, F. **Coherent atomic matter waves**. Berlin: Springer, 2001. (Les Houches - Ecole d'Ete de Physique Theorique).

36 CHERRORET, N.; DELANDE, D.; TIGGELEN, B. A. van. Induced dipole-dipole interactions in light diffusion from point dipoles. **Physical Review A**, v. 94, p. 012702, 2016. DOI: 10.1103/PhysRevA.94.012702.

37 ROSSUM, M. C. W. van; NIEUWENHUIZEN, T. M. Multiple scattering of classical waves: microscopy, mesoscopy, and diffusion. **Reviews of Modern Physics**, v. 71, p. 313, 1999. DOI: 10.1103/RevModPhys.71.313.

38 BUSCH, K.; SOUKOULIS, C. M.; ECONOMOUT, E. N. Transport and scattering mean free paths of classical waves. **Physical Review B**, v. 50, p. 93, 1994. DOI: 10.1103/PhysRevB.50.93.

39 ANDERSON, P. W. Absence of diffusion in certain random lattices. **Physical Review Journals Archive**, v. 109, p. 1492, 1958. DOI: 10.1103/PhysRev.109.1492.

40 LAGENDIJK, A.; TIGGELEN, B. van; WIERSMA, D. S. Fifty years of anderson localization. **Physics Today**, v. 62, p. 24–29, 2009. DOI: 10.1063/1.3206091.

41 LAHINI, Y. *et al.* Anderson localization and nonlinearity in one-dimensional disordered photonic lattices. **Physical Review Letters**, v. 100, p. 013906, 2008. DOI: 10.1103/PhysRevLett.100.013906.

42 SKIPETROV, S. E.; SOKOLOV, I. M. Absence of anderson localization of light in a random ensemble of point scatterers. **Physical Review Letters**, v. 112, p. 023905, 2014. DOI: 10.1103/PhysRevLett.112.023905.

43 COURTEILLE, P. W. *et al.* Modification of radiation pressure due to cooperative scattering of light. **The European Physical Journal D**, v. 58, n. 4, p. 69–73, 2010. DOI: 10.1140/epjd/e2010-00095-6.

44 SINGHAM, S. B.; BOHREN, C. F. Evaluation of the scattering matrix of an arbitrary particle using the coupled dipole approximation. **Journal of Chemical Physics**, v. 84, p. 2658, 1986. DOI: 10.1063/1.450338.

45 SINGHAM, S. B.; BOHREN, C. F. Light scattering by an arbitrary particle: a physical reformulation of the coupled dipole method. **Optics Letters**, v. 12, p. 10–12, 1987. DOI: 10.1364/OL.12.000010.

46 MARKEL, V. Coupled-dipole approach to scattering of light from a one-dimensional periodic dipole structure. **Journal of Modern Optics**, v. 40, p. 2281, 1993. DOI: 10.1080/09500349314552291.

47 TAUBENBLATT, M. A.; TRAN, T. K. Calculation of light scattering from particles and structures on a surface by the coupled-dipole method. **Journal of the Optical Society of America A**, v. 10, n. 5, p. 912–919, 1993. DOI: 10.1364/JOSAA.10.000912.

48 HERZ, F.; BIEHS, S.-A. Generalized coupled dipole method for thermal far-field radiation. **Physical Review B**, v. 105, p. 205422, 2022. DOI: 10.1103/PhysRevB.105.205422.

49 JENNEWEIN, S. *et al.* Coherent scattering of near-resonant light by a dense, microscopic cloud of cold two-level atoms: experiment versus theory. **Physical Review A**, v. 97, p. 053816, 2018. DOI: 0.1103/PhysRevA.97.053816.

50 SHNERB, N.; KAVEH, M. Non-rayleigh statistics of waves in random systems. **Physical Review B**, v. 43, p. 1279, 1991. DOI: 10.1103/PhysRevB.43.1279.

51 FOOT, C. J. **Atomic physics**. Oxford: Oxford University Press, 2005. ISBN 0198506953, 9780198506959.

52 GERRY, C.; KNIGHT, P. **Introductory quantum optics**. Cambridge: Cambridge University Press, 2004. ISBN 9780511791239.

53 SCULLY, M. O.; ZUBAIRY, M. S. **Quantum optics**. Cambridge: Cambridge University Press, 1997. ISBN 0521435951, 9780521435956.

54 BIENAIME, T. *et al.* Atom and photon measurement in cooperative scattering by cold atoms. **Journal of Modern Optics**, v. 58, n. 12, p. 1942–1950, 2011. DOI: 10.1080/09500340.2011.594911.

55 CIPRIS, A. **Long-lived collective modes of light in cold atoms**: experimental and numerical studies on subradiance and anderson localization. 80 p. Thèse (Physics) — Université Côte D'azur, Nice, 2022. Available at: https://theses.hal.science/tel-03706978. Accessible at: 10 oct. 2023.

56 ANDREOLI, F. *et al.* The maximum refractive index of an atomic medium. **Physical Review X**, v. 11, n. 1, p. 011026, 2021. DOI: 10.1103/PhysRevX.11.011026.

57 AKKERMANS, E.; GERO, A.; KAISER, R. Photon localization and dicke superradiance in atomic gases. **Physical Review Letters**, v. 101, p. 103602, 2008. DOI: 10.1103/PhysRevLett.101.103602.

58 MANASSAH, J. T. Cooperative radiation from atoms in different geometries: decay rate and frequency shift. **Advances in Optics and Photonics**, v. 4, p. 108 – 156, 2012. DOI: 10.1364/AOP.4.000108.

59 STELLMER, S. **Degenerate quantum gases of strontium**. 2013. 80 p. Thesis (Doctor in Science) — Faculty of Mathematics, Computer, Science and Physics, University of Innsbruck, Innsbruck, 2013. Available at: http://www.arxiv-vanity.com/papers/1307.0601. Accessible at: 20 oct. 2023.

60 BOYD, M. M. *et al.* Nuclear spin effects in optical lattice clocks. **Physical Review A**, v. 76, p. 022510, 2007. DOI: 10.1103/PhysRevA.76.022510.

61 TOPTICA. **TA-SHG-Pro user's manual**. Available at: https://www.toptica.com/products/tunable-diode-lasers/frequency-converted-lasers/ta-shg-pro. Accessible at: 24 sep. 2023.

62 PRESTO, D. W. Doppler-free saturated absorption: laser spectroscopy. **American Journal of Physics**, v. 64, n. 11, p. 1432–1436, 1996. DOI: doi:10.1119/1.18457.

63 HAYAKAWA, Y. *et al.* Doppler-free spectroscopy of metastable sr atoms using a hollow cathode lamp. **Applied Optics**, v. 57, n. 6, p. 1450, 2018. DOI: 10.1364/AO.57.001450.

64 PALMER, S. *et al.* High bandwidth frequency modulation of an external cavity diode laser using an intracavity lithium niobate electro-optic modulator as output coupler. **APL Photon**, v. 7, p. 086106, 2022. DOI: 10.1063/5.0097880.

65 DIAS, P. S. **Coerência espectral da luz espalhada por átomos frios saturados**. 102 p. Dissertação (Mestrado) — Universidade Federal de São Carlos, São Carlos, 2020. Available at: https://repositorio.ufscar.br/handle/ufscar/13856. Accessible at: 8 jun. 2023.

66 LIU, Z.; SLAVIK, R. Optical injection locking: from principle to applications. **Journal of Lightwave Technology**, v. 38, n. 1, p. 43, 2020.

67 MOORE, R. W. G. *et al.* Measurement of vacuum pressure with a magneto-optical trap: a pressure-rise method. **Review of Scientific Instruments**, v. 86, n. 9, p. 093108, 2015. DOI: 10.1063/1.4928154.

68 DIAS, P. G. S. *et al.* Characterization of the collimation of an atomic beam with a monochromatic quasi-resonant laser. **Brazilian Journal of Physics**, v. 51, p. 329–338, 2021. DOI: 10.1007/s13538-020-00837-9.

69 MORIYA, P. **Collective effects in light scattering from cold strontium clouds**. 108 p. Tese (Doutorado em Ciências) — Instituto de Física de São Carlos, Universidade de São Paulo, São Carlos, 2016. Available at: http://http://www.ifsc.usp.br/~strontium/Publication/Thesis/PauloHisaoMoriyaThesis.pdf. Accessible at: 16 nov. 2023.

70 HANSCH, T. W.; SCHAWLOW, A. L. Cooling of gases by laser radiation. **Optics Communications**, v. 13, n. 1, p. 68, 1975. DOI: 10.1016/0030-4018(75)90159-5.

71 COURTEILLE, P. W. **Interaction of light with cold atoms**. 2023. Available at: https://www.ifsc.usp.br/~strontium/. Accessible at: 30 aug. 2023.

72 MORIYA, P. H. *et al.* Comparison between 403nm and 497nm repumping schemes for strontium magneto-optical traps. **Journal of Physics Communications**, v. 2, p. 125008, 2018. DOI: 10.1088/2399-6528/aaf662.

73 METCALF, H. J.; STRATEN, P. **Laser cooling and trapping**. Berlin: Springer, 1999. ISBN 978-0-387-98747-7.

74 XU, X. *et al.* Cooling and trapping of atomic strontium. **Journal of the Optical Society of America B**, v. 20, n. 5, p. 968–976, 2003. DOI: 10.1364/JOSAB.20.000968.

75 WALLIS, H.; ERTMER, W. Broadband laser cooling on narrow transitions. **Journal of the Optical Society of America B**, v. 6, n. 11, p. 2211, 1989. DOI: 10.1364/JOSAB.6.002211.

76 BAIER, S. **An optical dipole trap for Erbium with tunable geometry**. 2012. 102 p. Thesis (Master) — University of Innsbruck, Innsbruck, 2012. Available at: http://www.ultracold.at/theses/master_simon_baier/master_simon_baier.pdf. Accessible at: 5 jun. 2023.

77 LIAO, G.-B. *et al.* Optimization of a crossed optical dipole trap for loading and confining laser-cooled atoms. **Journal of the Optical Society of America B**, v. 34, n. 4, p. 869, 2003. DOI: 10.1364/JOSAB.34.000869.

78 MAGNANI, P. **Armadilha óptica de dipolo para ^{88}Sr**. 76 p. Dissertação (Mestrado) — Universidade Federal de São Carlos, São Carlos, 2018. Available at: https://repositorio.ufscar.br/handle/ufscar/11482. Accessible at: 5 jun. 2023.

79 MAKHALOV, V. *et al.* Precision measurement of a trapping potential for an ultracold gas. **Physics Letters A**, v. 379, p. 327–332, 2015. DOI: 10.1016/j.physleta.2014.10.049.

80 TUCHENDLER, C. *et al.* Energy distribution and cooling of a single atom in an optical tweezer. **Physical Review A**, v. 78, p. 033425, 2008. DOI: 10.1103/PhysRevA.78.033425.

81 TONIOLO, U. *et al.* Breathing mode frequency of a strongly interacting fermi gas across the 2d-3d dimensional crossover. **arXiv**, 2018. Available at: https://arxiv.org/abs/1803.07714. Accessible at: 23 sep. 2023.

82 PITAEVSKII, L. P.; ROSCH, A. Breathing modes and hidden symmetry of trapped atoms in two dimensions. **Physical Review A**, v. 55, n. 2, p. R853, 1997. DOI: 10.1103/PhysRevA.55.R853.

83 WERNER, F.; CASTIN, Y. Unitary gas in an isotropic harmonic trap: Symmetry properties and applications. **Physical Review A**, v. 74, p. 053604, 2006. DOI: 10.1103/PhysRevA.74.053604.

84 ANDREWS, M. R. *et al.* Direct, nondestructive observation of a bose condensate. **Science**, v. 273, n. 5271, p. 84–87, 1996. DOI: 10.1126/science.273.5271.84.

85 MEPPELINK, R. *et al.* Phase contrast imaging of bose condensed clouds. **arXiv**, 2009. Available at: https://arxiv.org/abs/0909.4429. Accessible at: 8 oct. 2023.

86 SCHUNEMANN, U. *et al.* Simple scheme for tunable frequency offset locking of two lasers. **Review of Scientific Instruments**, v. 70, n. 1, p. 242–243, 1999. DOI: 10.1063/1.1149573.

87 TOPTICA. **Data sheet DL pro HP 461-029059**. Available at: https://www.toptica.com/fileadmin/Editors_English/11_brochures_datasheets/01_brochures/toptica_BR_Scientific_Lasers.pdf. Accessible at: 21 nov. 2023.

88 VILLE, J. *et al.* Loading and compression of a single two-dimensional bose gas in an optical accordion. **Physical Review A**, v. 95, n. 1, p. 013632, 2017. DOI: 10.1103/PhysRevA.95.013632.

89 MARTINS, M. A. **Implementação de uma amostra atômica fria 2D para o estudo do espalhamento de luz em regimes densos bidimensionais**. Exame de Qualificação do Mestrado. 2023.

APPENDIX A – CALCULATING THE EFFECTIVE COUPLING BETWEEN THE ATOMIC DIPOLES

A.1 The vectorial Kernel

In this appendix, we are going to make the detailed deduction of the expression for the Kernel of the interactions between the atomic dipoles that we considered in the Coupled Dipole Model equations. Basically, we are going to start from the equation (2.24) and to solve the integral

$$\mathrm{B}_{j,\alpha,m,\gamma}(t) = \sum_{\mathbf{k},\boldsymbol{\epsilon}} g^*_{\mathbf{k},\boldsymbol{\epsilon},\alpha}\; g_{\mathbf{k},\boldsymbol{\epsilon},\gamma}\; e^{i\mathbf{k}\cdot(\mathbf{R}_j-\mathbf{R}_m)} \int_0^t dt' e^{i(\omega_l-\omega_k)(t-t')}\hat{\beta}^-_{m,\gamma}(t')\;, \tag{A.1}$$

applying a few approximations that are going to be explained here.

The first step consist in replacing the summation over $\mathbf{k}$ by an integral. This is possible because in the limit of the integration volume going to infinity, the spacing between consecutive $\mathbf{k}$ goes to zero. Assuming a quantization volume V, we have:

$$\sum_{\mathbf{k}} \rightarrow \frac{V}{(2\pi)^3}\int_0^\infty dk k^2 \int_0^\pi d\theta \sin\theta \int_0^{2\pi} d\phi\;;$$

then,

$$\begin{aligned}\mathrm{B}_{j,\alpha,m,\gamma}(t) =& \sum_{\boldsymbol{\epsilon}} \frac{V}{(2\pi)^3}\int_0^\infty dk\; k^2 \int_0^\pi d\theta \sin\theta \int_0^{2\pi} d\phi\; g^*_{\mathbf{k},\boldsymbol{\epsilon},\alpha}\; g_{\mathbf{k},\boldsymbol{\epsilon},\gamma}\; e^{i\mathbf{k}\cdot(\mathbf{R}_j-\mathbf{R}_m)} \\ &\times \int_0^t dt' e^{i(\omega_l-\omega_k)(t-t')}\hat{\beta}^-_{m,\gamma}(t')\;.\end{aligned} \tag{A.2}$$

Using the definition of $g_{\mathbf{k},\boldsymbol{\epsilon},\alpha} = d\,\sqrt{\frac{\omega_k}{2\hbar\varepsilon_0 V}}\boldsymbol{\epsilon}_\alpha\cdot\boldsymbol{\epsilon}^*$ and that $\omega_k = ck$, we obtain:

$$\begin{aligned}\mathrm{B}_{j,\alpha,m,\gamma}(t) =& \frac{d^2}{2(2\pi)^3\epsilon_0\hbar c^3}\int_0^\infty d\omega_k\; \omega_k^3 \int_0^\pi d\theta \sin\theta \int_0^{2\pi} d\phi \left(\sum_{\boldsymbol{\epsilon}} \boldsymbol{\epsilon}^*_\alpha\cdot\boldsymbol{\epsilon}\;\boldsymbol{\epsilon}_\gamma\cdot\boldsymbol{\epsilon}^*\right) e^{i\mathbf{k}\cdot(\mathbf{R}_j-\mathbf{R}_m)} \\ &\times \int_0^t dt' e^{i(\omega_l-\omega_k)(t-t')}\hat{\beta}^-_{m,\gamma}(t')\;.\end{aligned} \tag{A.3}$$

In order to solve this integral for $m = 1, ..., N$ and $\gamma = x, y, z$, we will consider the cases when $m = j$ and $m \neq j$, discussed in the following sections.

A.1.1 $\mathrm{B}_{j,\alpha,m,\gamma}$ when $m = j$

In the particular case of $m = j$, we can have two possibilities: $\gamma = \alpha$ or $\gamma \neq \alpha$. Lets begin considering the first situation and here we can notice that

$$\sum_{\boldsymbol{\epsilon}} \boldsymbol{\epsilon}^*_\alpha\cdot\boldsymbol{\epsilon}\;\boldsymbol{\epsilon}_\gamma\cdot\boldsymbol{\epsilon}^* = \sum_{\boldsymbol{\epsilon}} (\boldsymbol{\epsilon}^*_\alpha\cdot\boldsymbol{\epsilon})^2\;, \tag{A.4}$$

where each $\boldsymbol{\epsilon}$ represents one of two orthogonal polarizations of mode $\mathbf{k}$; so both polarizations, that we can consider as linears, determine a plane perpendicular to $\mathbf{k}$. Also, $\boldsymbol{\epsilon}_\alpha$ represents the direction of the atomic dipole moment, but as the integration is made symmetrically on all directions of $\mathbf{k}$, the resulte would be the same for any direction of $\boldsymbol{\epsilon}_\alpha$. Then, for simplicity we will assume $\boldsymbol{\epsilon}_\alpha = \boldsymbol{\epsilon}_z$ and

$$\sum_{\boldsymbol{\epsilon}} (\boldsymbol{\epsilon}_\alpha^* \cdot \boldsymbol{\epsilon})^2 = 1 - \left(\frac{\boldsymbol{\epsilon}_\alpha \cdot \mathbf{k}}{k}\right)^2 = 1 - \cos^2\theta = \sin^2\theta \ . \tag{A.5}$$

Replacing this in equation (A.3), we get:

$$\begin{aligned} \mathrm{B}_{j,\alpha,j,\alpha} &= \frac{d^2}{2(2\pi)^3\epsilon_0\hbar c^3}\int_0^\infty d\omega_k\ \omega_k^3 \int_0^\pi d\theta \sin^3\theta \int_0^{2\pi} d\phi \int_0^t dt' e^{i(\omega_l-\omega_k)(t-t')}\hat{\beta}^-_{j,\alpha}(t') \\ &= \frac{2d^2}{3(2\pi)^3\epsilon_0\hbar c^3}\int_0^\infty d\omega_k\ \omega_k^3 \int_0^t dt' e^{i(\omega_l-\omega_k)(t-t')}\hat{\beta}^-_{j,\alpha}(t') \ . \end{aligned} \tag{A.6}$$

To calculate the remaining integrals we apply the Weisskopf-Wigner treatment that consist in considering $\omega_k \sim \omega_0$ and the lower limit of the integral on ω_k as $-\infty$ instead of 0, since those terms will not contribute to the integral for being too far away from ω_l. These considerations relies on the fact that only values of ω_k close enough to ω_l (such the $|\omega_l - \omega_k| \lesssim \frac{1}{|t-t'|}$) will play a role for all t' in the time integration; for all other values, the term $e^{i(\omega_l-\omega_k)(t-t')}$ will quickly average to zero. Now, we have:

$$\mathrm{B}_{j,\alpha,j,\alpha} = \frac{2d^2\omega_0^3}{3(2\pi)^3\epsilon_0\hbar c^3}\int_0^t dt' \int_{-\infty}^\infty d\omega_k\ e^{i(\omega_l-\omega_k)(t-t')}\hat{\beta}^-_{j,\alpha}(t') \ . \tag{A.7}$$

The integral over ω_k gives

$$\int_{-\infty}^\infty d\omega_k\ e^{i(\omega_l-\omega_k)(t-t')} = 2\pi\delta(t-t') \tag{A.8}$$

and the integration on t gives

$$\int_0^t dt'\delta(t-t')\hat{\beta}^-_{j,\alpha}(t') = \frac{\hat{\beta}^-_{j,\alpha}(t)}{2} \ . \tag{A.9}$$

Finally, we arrive at:

$$\mathrm{B}_{j,\alpha,j,\alpha} = \frac{\Gamma}{2}\hat{\beta}^-_{j,\alpha}(t) \ , \tag{A.10}$$

where

$$\Gamma = \frac{d^2\omega_0^3}{3\pi\epsilon_0\hbar c^3} \tag{A.11}$$

is the linewidth of the atomic transition.

We will now consider the situation where $\gamma \neq \alpha$ and, in order to calculate the term $\left(\sum_{\boldsymbol{\epsilon}} \boldsymbol{\epsilon}_\alpha^* \cdot \boldsymbol{\epsilon}\ \boldsymbol{\epsilon}_\gamma \cdot \boldsymbol{\epsilon}^*\right)$ in equation (A.3), we can consider $\alpha = x$ and $\gamma = y$ since there is no

preferred direction for the calculation of this term. We will also define the two orthogonal polarization directions $\boldsymbol{\epsilon}$ as $\boldsymbol{\epsilon}_1 = \boldsymbol{\epsilon}_\theta$ and $\boldsymbol{\epsilon}_2 = \boldsymbol{\epsilon}_\phi$. Using the conversion between cylindrical and cartesian coordinates, we have

$$\begin{aligned}\boldsymbol{\epsilon}_1 = \boldsymbol{\epsilon}_\theta &= \cos\theta\cos\phi\ \boldsymbol{\epsilon}_x + \cos\theta\sin\phi\ \boldsymbol{\epsilon}_y - \sin\theta\ \boldsymbol{\epsilon}_z \\ \boldsymbol{\epsilon}_2 = \boldsymbol{\epsilon}_\phi &= -\sin\phi\ \boldsymbol{\epsilon}_x + \cos\phi\ \boldsymbol{\epsilon}_y\end{aligned}$$

Then,

$$\sum_{\boldsymbol{\epsilon}} \boldsymbol{\epsilon}_\alpha^* \cdot \boldsymbol{\epsilon}\ \boldsymbol{\epsilon}_\gamma \cdot \boldsymbol{\epsilon}^* = (\boldsymbol{\epsilon}_\alpha^* \cdot \boldsymbol{\epsilon}_1\ \boldsymbol{\epsilon}_\gamma \cdot \boldsymbol{\epsilon}^*) + (\boldsymbol{\epsilon}_\alpha^* \cdot \boldsymbol{\epsilon}_2\ \boldsymbol{\epsilon}_\gamma \cdot \boldsymbol{\epsilon}^*) = -\sin\theta^2 \sin\phi\cos\phi\ . \tag{A.12}$$

Finally, replacing this result, we see that the integration over ϕ gives 0, so

$$\mathrm{B}_{j,\alpha,j,\gamma} = 0 \text{ for } \gamma, \alpha \in \{z, y, z\},\ \gamma \neq \alpha\ , \tag{A.13}$$

and putting together the two results for $m = j$, we obtain:

$$\mathrm{B}_{j,\alpha,j,\gamma} = \frac{\Gamma}{2}\ \delta_{\alpha,\gamma}\ \hat{\beta}_{j,\alpha}^{-}(t) \quad \text{for } \gamma, \alpha \in \{z, y, z\}\ . \tag{A.14}$$

This term represents a non-hermitian correction of the Hamiltonian for the single atom, that represent the decay rate of the atomic coherence due to the interaction of the atom with the modes of the electromagnetic field.

Note that the last equation leads to the expression (2.29) given in the second chapter of this document.

A.1.2 $\mathrm{B}_{j,\alpha,m,\gamma}$ when $m \neq j$

In the general case when $m \neq j$, we see in equation (A.3), the appearing of a preferred direction of the integral, which is the vector $\mathbf{R}_j - \mathbf{R}_m = \mathbf{R}_{jm} = (x_{jm}, y_{jm}, z_{jm})$. So now we have three directions in our integral given by $\boldsymbol{\epsilon}_\alpha$, $\boldsymbol{\epsilon}_\gamma$ and $\mathbf{R}_{jm}$.

The term $e^{i\mathbf{k}\cdot\mathbf{R}_{jm}}$ is going to make the integral more difficult to solve, since $\mathbf{R}_{jm}$ and $\mathbf{k} = k(\sin\theta\cos\phi\boldsymbol{\epsilon}_x + \sin\theta\sin\phi\boldsymbol{\epsilon}_y + \cos\theta\boldsymbol{\epsilon}_z)$ are in any directions. For convenience, we will perform a rotation of coordinates in order to put $\mathbf{R}_{jm}$ in the direction of $\boldsymbol{\epsilon}_{z'}$, such as $\mathbf{R}_{jm} = R_{jm}\boldsymbol{\epsilon}_{z'}$; see the figure 57. In this case, writing $\mathbf{k} = k(\sin\theta'\cos\phi'\boldsymbol{\epsilon}_{x'} + \sin\theta'\sin\phi'\boldsymbol{\epsilon}_{y'} + \cos\theta'\boldsymbol{\epsilon}_{z'})$, the scalar product is simplified as $\mathbf{k}\cdot\mathbf{R}_{jm} = kR_{jm}\cos\theta'$.

In this figure we have defined two new vectors: $\mathbf{v}_1 \equiv \cos\phi_{jm}\boldsymbol{\epsilon}_x + \sin\phi_{jm}\boldsymbol{\epsilon}_y$ and $\mathbf{v}_2 \equiv \boldsymbol{\epsilon}_z \times \mathbf{v}_1 = -\sin\phi_{jm}\boldsymbol{\epsilon}_x + \cos\phi_{jm}\boldsymbol{\epsilon}_y$. We see that $\mathbf{v}_1$, $\mathbf{v}_2$ and $\boldsymbol{\epsilon}_z$ constitute a new orthonormal basis and $\mathbf{R}_{jm}$ in contained in the plane determined by $\boldsymbol{\epsilon}_z$ and $\mathbf{v}_1$. The rotation of coordinates that puts $\mathbf{R}_{jm}$ in the direction $\boldsymbol{\epsilon}_{z'}$ is a rotation of an angle $-\theta_{jm}$ around the vector $\mathbf{v}_2$. The coordinates transformation can be written as:

$$\begin{aligned}z' &= \cos\theta_{jm}z + \sin\theta_{jm}\ \mathbf{R}_{jm}\cdot\mathbf{v}_1 \\ \mathbf{R}_{jm}\cdot\mathbf{v}_1' &= -\sin\theta_{jm}z + \cos\theta_{jm}\ \mathbf{R}_{jm}\cdot\mathbf{v}_1 \\ \mathbf{R}_{jm}\cdot\mathbf{v}_2' &= \mathbf{R}_{jm}\cdot\mathbf{v}_2\end{aligned}$$

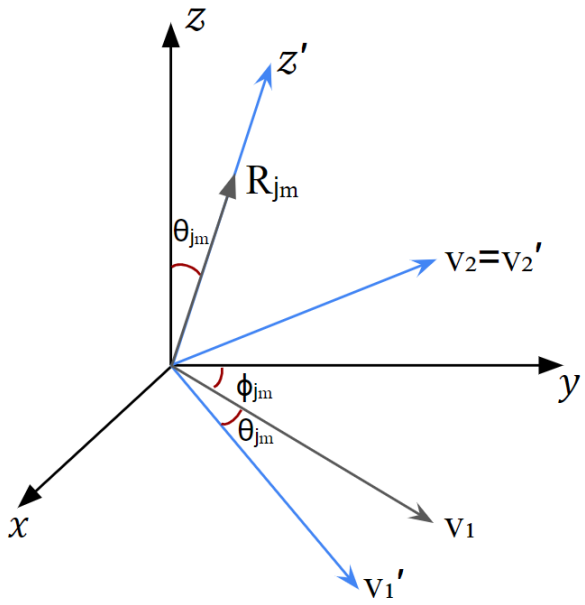

Figure 57 – Rotation of coordinate system, from $\{x,y,z\}$ to $\{x',y',z'\}$.

Source: By the author.

Inverting the system of equations above and using the definition of the vectors $\mathbf{v}_1$ and $\mathbf{v}_2$, as well as $\mathbf{v}_1' \equiv \cos\phi_{jm}\boldsymbol{\epsilon}_{x'} + \sin\phi_{jm}\boldsymbol{\epsilon}_{y'}$ and $\mathbf{v}_2' \equiv -\sin\phi_{jm}\boldsymbol{\epsilon}_{x'} + \cos\phi_{jm}\boldsymbol{\epsilon}_{y'}$, we obtain:

$$
\begin{aligned}
x &= (1-\cos^2\phi_{jm}(1-\cos\theta_{jm}))x' - \sin\phi_{jm}\cos\phi_{jm}(1-\cos\theta_{jm})y' + \sin\theta_{jm}\cos\phi_{jm}z' \\
y &= -\sin\phi_{jm}\cos\phi_{jm}(1-\cos\theta_{jm})x' + (1-\sin^2\phi_{jm}(1-\cos\theta_{jm}))y' + \sin\theta_{jm}\sin\phi_{jm}z' \\
z &= -\sin\theta_{jm}\cos\phi_{jm}x' - \sin\theta_{jm}\sin\phi_{jm}y' + \cos\theta_{jm}z'
\end{aligned}
$$

After this transformation of coordinates, we are now ready to perform the integration, but first lets consider $\alpha = \gamma = z$, so the term

$$
\sum_{\boldsymbol{\epsilon}} \boldsymbol{\epsilon}_\alpha^* \cdot \boldsymbol{\epsilon}\ \boldsymbol{\epsilon}_\gamma \cdot \boldsymbol{\epsilon}^* = \sum_{\boldsymbol{\epsilon}} (\boldsymbol{\epsilon}_z^* \cdot \boldsymbol{\epsilon})^2 = 1 - \frac{k_z^2}{k^2} = \sin^2\theta\ , \tag{A.15}
$$

which is similar as we saw in equation (A.5). In this way, the equation (A.3) becomes

$$
\begin{aligned}
\mathrm{B}_{j,z,m,z} = &\frac{d^2}{2(2\pi)^3\epsilon_0\hbar c^3}\int_0^\infty d\omega_k\omega_k^3\int_0^\pi d\theta\sin\theta\int_0^{2\pi} d\phi\sin^2\theta e^{i\mathbf{k}\cdot\mathbf{R}_{jm}} \\
&\times\int_0^t dt' e^{i(\omega_l-\omega_k)(t-t')}\hat{\beta}_{m,z}^-(t')\ .
\end{aligned} \tag{A.16}
$$

Lets apply the rotation of coordinates described before. Note that the modulus of any vector is the same for both coordinates, so: $\omega_k' = \omega_k$, $k' = k$, $R_{jm}' = R_{jm}$, and the Jacobian of the transformation keeps the same expressions for the integral:

$$
\int_0^\pi d\theta'\sin\theta'\int_0^{2\pi} d\phi' = \int_0^\pi d\theta\sin\theta\int_0^{2\pi} d\phi\ .
$$

Putting the term $\sin^2\theta = 1 - k_z^2/k^2$ as a function of the (k'_x, k'_y, k'_z) in the new basis:

$$\sin^2\theta = 1 - \left(- \sin\theta_{jm}\cos\phi_{jm}\frac{k'_x}{k} - \sin\theta_{jm}\sin\phi_{jm}\frac{k'_y}{k} + \cos\theta_{jm}\frac{k'_z}{k}\right)^2$$

and using the fact that $\frac{k'_x}{k} = \sin\theta'\cos\phi'$, $\frac{k'_y}{k} = \sin\theta'\sin\phi'$ and $\frac{k'_z}{k} = \cos\theta'$, we have:

$$\begin{aligned}\sin^2\theta =& 1 - \sin^2\theta_{jm}(\cos^2\phi_{jm}\cos^2\phi' + \sin^2\phi_{jm}\sin^2\phi' + 2\sin\phi_{jm}\cos\phi_{jm}\sin\phi'\cos\phi')\sin^2\theta' \\ & - \cos^2\theta_{jm}\cos^2\theta' + 2\sin\theta_{jm}\cos\theta_{jm}(\cos\phi_{jm}\cos\phi' + \sin\phi_{jm}\sin\phi')\sin\theta'\cos\theta' \ .\end{aligned} \tag{A.17}$$

Finally, since in the new basis $\mathbf{R}_{jm} = R_{jm}\cos\theta'$, the term

$$e^{i\mathbf{k}\cdot\mathbf{R}_{jm}} = e^{ikR_{jm}\cos\theta'} \ . \tag{A.18}$$

Replacing the equations (A.17) and (A.18) in equation (A.16), and solving the integral on ϕ', which is kind of simple, we arrive at

$$\begin{aligned}\mathrm{B}_{j,z,m,z} =& \frac{d^2}{2(2\pi)^3\epsilon_0\hbar c^3}\int_0^\infty d\omega_k\omega_k^3\int_0^\pi d\theta'\sin\theta'\left[\sin^2\theta_{jm} + \left(1 - \frac{3\sin^2\theta_{jm}}{2}\right)\sin^2\theta'\right] \\ & \times e^{ikR_{jm}\cos\theta'}\int_0^t dt' e^{i(\omega_l-\omega_k)(t-t')}\hat{\beta}^-_{m,z}(t') \ .\end{aligned} \tag{A.19}$$

We use now the following relations:

$$\int_0^\pi d\theta'\sin\theta' e^{ikR_{jm}\cos\theta'} = 2\ \frac{\sin kR_{jm}}{kR_{jm}} \tag{A.20}$$

$$\int_0^\pi d\theta'\sin^3\theta' e^{ikR_{jm}\cos\theta'} = 4\ \frac{\sin kR_{jm} - kR_{jm}\cos kR_{jm}}{(kR_{jm})^3} \tag{A.21}$$

and, the integral on θ', using that $\sin^2\theta_{jm} = 1 - z_{jm}^2/R_{jm}^2$, becomes

$$\begin{aligned}&\int_0^\pi d\theta'\sin\theta'\left[\sin^2\theta_{jm} + \left(1 - \frac{3\sin^2\theta_{jm}}{2}\right)\sin^2\theta'\right]e^{ikR_{jm}\cos\theta'} \\ &\quad = \frac{2}{kR_{jm}^3}\left[(R_{jm}^2 - z_{jm}^2)\sin kR_{jm} + \left(\frac{\cos kR_{jm}}{kR_{jm}} - \frac{\sin kR_{jm}}{(kR_{jm})^2}\right)(R_{jm}^2 - 3z_{jm}^2)\right] \\ &\quad\quad = \frac{e^{ikR_{jm}}}{ikR_{jm}^3}\left[R_{jm}^2 - z_{jm}^2 + \left(\frac{i}{kR_{jm}} - \frac{1}{(kR_{jm})^2}\right)(R_{jm}^2 - 3z_{jm}^2)\right] \\ &\quad\quad\quad - \frac{e^{-ikR_{jm}}}{ikR_{jm}^3}\left[R_{jm}^2 - z_{jm}^2 + \left(-\frac{i}{kR_{jm}} - \frac{1}{(kR_{jm})^2}\right)(R_{jm}^2 - 3z_{jm}^2)\right] \ .\end{aligned} \tag{A.22}$$

Let's replace this last result in equation (A.19):

$$\begin{aligned}\mathrm{B}_{j,z,m,z} =& \frac{d^2}{2(2\pi)^3\epsilon_0\hbar c^3}\int_0^t dt' e^{i(\omega_l-\omega_k)(t-t')}\hat{\beta}^-_{m,z}(t') \\ & \left\{\int_0^\infty d\omega_k\omega_k^3\frac{e^{-i\omega_k(t-\frac{R_{jm}}{c}-t')}}{ikR_{jm}^3}\left[R_{jm}^2 - z_{jm}^2 + \left(\frac{i}{kR_{jm}} - \frac{1}{(kR_{jm})^2}\right)(R_{jm}^2 - 3z_{jm}^2)\right]\right. \\ & \left. - \int_0^\infty d\omega_k\omega_k^3\frac{e^{-i\omega_k(t-\frac{R_{jm}}{c}-t')}}{ikR_{jm}^3}\left[R_{jm}^2 - z_{jm}^2 + \left(\frac{i}{kR_{jm}} - \frac{1}{(kR_{jm})^2}\right)(R_{jm}^2 - 3z_{jm}^2)\right]\right\}\end{aligned} \tag{A.23}$$

To solve the integral over ω_k, we will apply the approximations of the Weisskopf-Wigner treatment that was described in the previews section: $\omega_k \sim \omega_0$, $k \sim k_0$ outside the argument of the exponential, and the integral of the exponential gives Dirac delta functions.

$$\begin{aligned}
&\int_0^\infty d\omega_k \omega_k^3 \frac{e^{-i\omega_k(t\mp\frac{R_{jm}}{c}-t')}}{ikR_{jm}^3}\left[R_{jm}^2 - z_{jm}^2 + \left(\frac{\pm i}{kR_{jm}} - \frac{1}{(kR_{jm})^2}\right)(R_{jm}^2 - 3z_{jm}^2)\right] \\
&\simeq 2\pi\omega_0^3 \frac{\delta(t\mp\frac{R_{jm}}{c}-t')}{ik_0R_{jm}^3}\left[R_{jm}^2 - z_{jm}^2 + \left(\frac{\pm i}{k_0R_{jm}} - \frac{1}{(k_0R_{jm})^2}\right)(R_{jm}^2 - 3z_{jm}^2)\right] . \qquad \text{(A.24)}
\end{aligned}$$

Replacing this result in equation (A.23), we see that the Dirac delta with argument $t+\frac{R_{jm}}{c}$ is equal to zero because this argument is outside the interval $0 \leq t' \leq t$, so the only Dirac delta different than zero is the one with argument $t - \frac{R_{jm}}{c}$, and we obtain

$$\begin{aligned}
\mathrm{B}_{j,z,m,z} &= \frac{d^2\omega_0^3}{4\pi\epsilon_0\hbar c^3}\frac{1}{ik_0R_{jm}^3}\left[R_{jm}^2 - z_{jm}^2 + \left(\frac{i}{k_0R_{jm}} - \frac{1}{(k_0R_{jm})^2}\right)(R_{jm}^2 - 3z_{jm}^2)\right] \\
&\qquad \int_0^t dt' e^{i\omega_l(t-t')}\hat{\beta}_{m,z}^-(t')\ \delta\left(t - \frac{R_{jm}}{c} - t'\right) \\
&= -\frac{3i\Gamma}{4}\frac{e^{ik_lR_{jm}}}{k_0R_{jm}^3}\left[R_{jm}^2 - z_{jm}^2 + \left(\frac{i}{k_0R_{jm}} - \frac{1}{(k_0R_{jm})^2}\right)(R_{jm}^2 - 3z_{jm}^2)\right]\hat{\beta}_{m,z}^-\left(t - \frac{R_{jm}}{c}\right)
\end{aligned} \qquad \text{(A.25)}$$

We can see in the equation above that the argument of the operator $\hat{\beta}_{m,z}^-$ possess a retardation time given by $\frac{R_{jm}}{c}$, which is the time needed for the light emitted by one atom to travel through the cloud and reach another atom. For small enough clouds, this term is negligible with respect to all other time scales of the problem and we can consider that $t - \frac{R_{jm}}{c} \simeq t$. This approximation is called *rapid transit approximation*. Since the typical timescales of the problem are given by the inverse of the typical frequency Γ, Ω and Δ; for applying the rapid transit approximation is necessary that $\Gamma, \Omega, \Delta \ll \frac{c}{R}$ for a cloud of size R. As a consequence of this approximation, we also have that the ratio $\frac{e^{i\omega_l R_{jm}}}{e^{i\omega_0 R_{jm}}} = e^{i\Delta R_{jm}} \simeq 1$, so we can write $e^{ik_lR_{jm}} \simeq e^{ik_0R_{jm}}$ and put the expression as a function of the atomic quantities. After this approximation, we arrive at:

$$\mathrm{B}_{j,z,m,z} = -\frac{3i\Gamma}{4}\frac{e^{ik_0R_{jm}}}{k_0R_{jm}^3}\left[R_{jm}^2 - z_{jm}^2 + \left(\frac{i}{k_0R_{jm}} - \frac{1}{(k_0R_{jm})^2}\right)(R_{jm}^2 - 3z_{jm}^2)\right]\hat{\beta}_{m,z}^-(t) \ . \qquad \text{(A.26)}$$

In the situation considered here, there is nothing that determines direction in the interaction of the atoms with the isotropic electromagnetic modes of the vacuum. By symmetry, the expression obtained must be identical for the x or y direction, we have then

$$\mathrm{B}_{j,x,m,x} = -\frac{3i\Gamma}{4}\frac{e^{ik_0R_{jm}}}{k_0R_{jm}^3}\left[R_{jm}^2 - x_{jm}^2 + \left(\frac{i}{k_0R_{jm}} - \frac{1}{(k_0R_{jm})^2}\right)(R_{jm}^2 - 3x_{jm}^2)\right]\hat{\beta}_{m,x}^-(t) \qquad \text{(A.27)}$$

and

$$\mathrm{B}_{j,y,m,y} = -\frac{3i\Gamma}{4}\frac{e^{ik_0R_{jm}}}{k_0R_{jm}^3}\left[R_{jm}^2 - y_{jm}^2 + \left(\frac{i}{k_0R_{jm}} - \frac{1}{(k_0R_{jm})^2}\right)(R_{jm}^2 - 3y_{jm}^2)\right]\hat{\beta}_{m,y}^-(t) \quad \text{(A.28)}$$

Lets now consider the terms with $\alpha \neq \gamma$, beginning with $\alpha = x$ and $\gamma = y$, so

$$\begin{aligned}\mathrm{B}_{j,x,m,y} =& \frac{d^2}{2(2\pi)^3\epsilon_0\hbar c^3}\int_0^\infty d\omega_k\omega_k^3\int_0^\pi d\theta\sin\theta\int_0^{2\pi}d\phi\,\left(\sum_{\boldsymbol{\epsilon}}\boldsymbol{\epsilon}_x^*\cdot\boldsymbol{\epsilon}\;\boldsymbol{\epsilon}_y\cdot\boldsymbol{\epsilon}^*\right)e^{i\mathbf{k}\cdot\mathbf{R}_{jm}} \\ &\times\int_0^t dt' e^{i(\omega_l-\omega_k)(t-t')}\hat{\beta}_{m,z}^-(t')\ . \end{aligned} \quad \text{(A.29)}$$

Similar as the strategy followed in the previews case, we will perform a transform of coordinates and solve first the integral over ϕ'. We get then:

$$\begin{aligned}\mathrm{B}_{j,x,m,y} =& \frac{d^2}{2(2\pi)^3\epsilon_0\hbar c^3}\int_0^\infty d\omega_k\omega_k^3\int_0^\pi d\theta'\sin^2\theta_{jm}\sin\phi_{jm}\cos\phi_{jm}\sin\theta'\left(\frac{3\sin^2\theta_{jm}}{2}-1\right) \\ &\times e^{ikR_{jm}\cos\theta'}\int_0^t dt' e^{i(\omega_l-\omega_k)(t-t')}\hat{\beta}_{m,y}^-(t')\ . \end{aligned} \quad \text{(A.30)}$$

Using the integrals (A.20) and (A.21), and that

$$\sin^2\theta_{jm}\sin\phi_{jm}\cos\phi_{jm} = \frac{x_{jm}y_{jm}}{R_{jm}^2}\ , \quad \text{(A.31)}$$

we have

$$\begin{aligned}\mathrm{B}_{j,z,m,z} =& \frac{d^2}{2(2\pi)^3\epsilon_0\hbar c^3}\int_0^t dt' e^{i\omega_l(t-t')}\hat{\beta}_{m,y}^-(t')(-x_{jm}y_{jm}) \\ &\left\{\int_0^\infty d\omega_k\omega_k^3\frac{e^{-i\omega_k(t-\frac{R_{jm}}{c}-t')}}{ikR_{jm}^3}\left[1+3\left(\frac{i}{kR_{jm}}-\frac{1}{(kR_{jm})^2}\right)\right]\right. \\ &\left.-\int_0^\infty d\omega_k\omega_k^3\frac{e^{-i\omega_k(t-\frac{R_{jm}}{c}-t')}}{ikR_{jm}^3}\left[1-3\left(\frac{i}{kR_{jm}}-\frac{1}{(kR_{jm})^2}\right)\right]\right\}\ . \end{aligned} \quad \text{(A.32)}$$

Again, in order to integrate over ω_k, we use the approximations of the Weisskopf-Wigner treatment and applying also the rapid transit approximation, we obtain

$$\mathrm{B}_{j,x,m,y} = \frac{3i\Gamma}{4}\frac{e^{ik_0R_{jm}}}{k_0R_{jm}^3}x_{jm}y_{jm}\left[1+\left(\frac{i}{k_0R_{jm}}-\frac{1}{(k_0R_{jm})^2}\right)\right]\hat{\beta}_{m,y}^-(t) \quad \text{(A.33)}$$

and, by symmetry, we have

$$\mathrm{B}_{j,y,m,x} = \frac{3i\Gamma}{4}\frac{e^{ik_0R_{jm}}}{k_0R_{jm}^3}x_{jm}y_{jm}\left[1+\left(\frac{i}{k_0R_{jm}}-\frac{1}{(k_0R_{jm})^2}\right)\right]\hat{\beta}_{m,y}^-(t) \quad \text{(A.34)}$$

$$\mathrm{B}_{j,x,m,z} = \frac{3i\Gamma}{4}\frac{e^{ik_0R_{jm}}}{k_0R_{jm}^3}x_{jm}z_{jm}\left[1+\left(\frac{i}{k_0R_{jm}}-\frac{1}{(k_0R_{jm})^2}\right)\right]\hat{\beta}_{m,z}^-(t) \quad \text{(A.35)}$$

$$\mathrm{B}_{j,y,m,z} = \frac{3i\Gamma}{4}\frac{e^{ik_0R_{jm}}}{k_0R_{jm}^3}y_{jm}z_{jm}\left[1+\left(\frac{i}{k_0R_{jm}}-\frac{1}{(k_0R_{jm})^2}\right)\right]\hat{\beta}_{m,z}^-(t) \quad \text{(A.36)}$$

We can finally express all the results for $m \neq j$, in the expression:

$$B_{j,\alpha,m,\gamma} = \frac{3\Gamma}{4}\frac{e^{ik_0R_{jm}}}{ik_0R_{jm}^3}\Big[R_{jm}^2\boldsymbol{\epsilon}_\alpha^*\cdot\boldsymbol{\epsilon}_\gamma - (\mathbf{R}_{jm}\cdot\boldsymbol{\epsilon}_\alpha^*)(\mathbf{R}_{jm}\cdot\boldsymbol{\epsilon}_\gamma) + \left(\frac{i}{k_0R_{jm}} - \frac{1}{(k_0R_{jm})^2}\right)(R_{jm}^2\boldsymbol{\epsilon}_\alpha^*\cdot\boldsymbol{\epsilon}_\gamma - 3(\mathbf{R}_{jm}\cdot\boldsymbol{\epsilon}_\alpha^*)(\mathbf{R}_{jm}\cdot\boldsymbol{\epsilon}_\gamma))\Big]\hat{\beta}_{m,\alpha}(t)\ , \quad \text{for } m \neq j \text{ and } \alpha,\gamma \in \{x,y,z\}\ . \quad \text{(A.37)}$$

This last equation leads to the expression (2.28) of the chapter 2.